Discrete and continuum modelling of grain size segregation : application to bedload transport

Rémi Chassagne

Université Grenoble Alpes

THÈSE

Pour obtenir le grade de

DOCTEUR DE L'UNIVERSITÉ GRENOBLE ALPES

Spécialité : **Océan, Atmosphère, Hydrologie (CEOAH)**

Arrêté ministériel : 25 mai 2016

Présentée par

Rémi CHASSAGNE

Thèse dirigée par **Philippe Frey**, **Julien Chauchat** et **Raphaël Maurin**,

préparée au sein du **Laboratoire INRAE, UR ETNA**
dans **l'École Doctorale Terre, Univers, Environnement**

Discrete and continuum modelling of grain size segregation: application to bedload transport

Thèse soutenue publiquement le **19 Novembre 2020**,
devant le jury composé de :

M. Olivier Pouliquen
Directeur de Recherche, CNRS, IUSTI, Université Aix Marseille, Président
M. Pierre-Yves Lagrée
Directeur de Recherche, CNRS, UPMC, Rapporteur
M. Eric Lajeunesse
Physicien, CNAP, IPGP, Rapporteur
M. Nico Gray
Professor of applied Mathematics, University of Manchester, Examinateur
M. Philippe Frey
Chercheur HDR, INRAE, UR ETNA, Université Grenoble Alpes, Directeur de thèse
M. Julien Chauchat
Maître de conférence, LEGI, Université Grenoble Alpes, Co-directeur de thèse
M. Raphaël Maurin
Maître de conférence, IMFT, Toulouse INP, Encadrant de thèse

Abstract

Understanding particle size segregation is one of the great challenge in fluvial geomorphology. It is still notoriously difficult to predict sediment transport more accurately than within one order of magnitude. One of the main origin of this difficulty is particle size segregation, a granular process of particle sorting in the sediment bed. Size segregation is therefore a grain scale process impacting the morphological scale.

This PhD presents a numerical study of size segregation as a granular process during bedload transport. A coupled fluid discrete element method (DEM) is used to study the infiltration of small particles in a large particle bed. This configuration, close to granular flows on erodible bed, is characterized by a particle velocity profile, a shear rate profile and an inertial number profile exponentially decreasing into the bed. It presents a particular segregation phenomenology with small particles infiltrating the bed as a travelling wave, the velocity being controlled by the inertial number at the bottom of the layer. The segregation velocity is observed dependent on the local small particle concentrations and on the size ratio. The segregation problem is also analyzed with an advection diffusion model. With advection and diffusion coefficients both proportional to the inertial number, the continuum model perfectly reproduces the dynamics observed in the DEM results.

Very recently, a new segregation advection diffusion model has been derived based on particle scale forces, in particular a granular buoyancy force (or segregation force) and an inter-particle drag force. This provides new physically based parametrisations for the advection and diffusion coefficients. This new model is analysed in the bedload configuration, and reproduces qualitatively the DEM results. To improve the model, new dependencies on the inertial number and small particle concentration are proposed for the segregation and drag forces.

Finally, the impact of size segregation on sediment transport is studied through the mobility of bidisperse already segregated particle beds. Large particles are placed above small ones, and it is observed that, in the same fluid and surface bed conditions, the transport rate is higher in the bidisperse configuration than in the monodisperse one. For the range of studied size ratio ($r < 4$), it is showed that it is not a rugosity but a granular effect. This is analyzed within the framework of the $\mu(I)$ rheology and it is demonstrated that the buried small particles are more mobile than larger particles and play the role of a conveyor belt for the large particles at the surface. Based on rheological arguments, a simple predictive model for the additional transport in the bidisperse case is proposed, which reproduces quite well the DEM results for a large range of Shields number and for size ratios smaller than 4. The results of the model were used to identify four different transport regimes of bidisperse mixtures, depending on the mechanisms responsible for the mobility of the small particles.

This work represents an important improvement in the understanding of size segregation during bedload transport and questions our understanding of bidisperse granular media, which have not been much studied. It also represents a first step in an upscaling process towards the morphological scale through continuum models.

Résumé

La compréhension du tri granulométrique des particules est un enjeu majeur pour l'étude des évolutions morphologiques des rivières de montagne. La prédiction des flux de transport reste difficile avec des écarts de plusieurs ordres de grandeurs entre les valeurs prédites et mesurées. L'une des raisons principales de cette difficulté est la ségrégation, phénomène granulaire de tri granulométrique des particules constituant le lit sédimentaire. La ségrégation est donc un phénomène à l'échelle du grain ayant un impact à l'échelle morphologique.

Cette thèse présente une étude numérique de la ségrégation en tant que phénomène granulaire dans le cas du charriage et son impact sur le transport sédimentaire. Un modèle aux éléments discrets (DEM) couplé à un modèle fluide turbulent unidimensionnel est utilisé. A l'instant initial, des petites particules sont déposées au dessus de particules plus grosses. Le fluide s'écoule par gravité et transporte les particules du lit sédimentaire. Cette configuration, proche d'un lit érodable, est caractérisée dans la profondeur par des profils exponentiellement décroissant de la vitesse particulaire, du taux de cisaillement et du nombre inertiel et présente une phénoménologie de ségrégation particulière. Les petites particules s'infiltrent en couche, sous forme d'onde progressive, dont la vitesse est contrôlée par le nombre inertiel en bas de la couche. On observe aussi que la vitesse de ségrégation est dépendante de la concentration locale en petites particules et du ratio de taille. Le problème de ségrégation est ensuite analysé à partir d'un modèle d'advection-diffusion. Avec un coefficient d'advection proportionnel au nombre inertiel, le modèle continu reproduit parfaitement la dynamique de la phase des petites particules. Enfin on démontre que pour reproduire l'onde progressive observée dans les simulations DEM, le coefficient de diffusion doit avoir la même dépendance avec le nombre inertiel que le coefficient d'advection.

Très récemment, un nouveau modèle d'advection-diffusion a été proposé dans la littérature à partir de forces inter-particulaires, notamment une force de portance (ou force de ségrégation) et de traînée, apportant de nouvelles paramétrisations physiques aux coefficients d'advection et de diffusion. Ce nouveau modèle est analysé ici dans la configuration du charriage. La dépendance en nombre inertiel, observée dans les résultats DEM, peut être retrouvée à partir de ces nouvelles paramétrisations. Pour reproduire quantitativement les simulations DEM, de nouvelles dépendances en nombre inertiel et concentration en petites particules sont proposées pour la force de ségrégation et le coefficient de traînée.

Enfin, l'impact de la ségrégation sur le transport sédimentaire est étudié en s'intéressant à la mobilité d'un lit bi-disperse déjà ségrégé. Les grosses particules sont placées au dessus des petites et on observe que, pour la même contrainte fluide et pour le même état granulaire de surface, le transport est plus élevé dans le cas bi-disperse que dans le cas mono-disperse. Pour la gamme de ratio de taille étudié ($r < 4$), on montre que l'augmentation de mobilité n'est pas un effet de rugosité mais un effet rhéologique. À partir d'une analyse dans le cadre de la rhéologie $\mu(I)$, il est démontré que les petites particules en profondeur sont plus mobiles que les grosses particules, jouant le rôle d'un tapis roulant pour les grosses particules de surface et augmentant ainsi la mobilité globale du lit sédimentaire. Basé sur des arguments rhéologiques, un modèle simple de prédiction de l'augmentation du flux sédimentaire est proposé, reproduisant correctement les résultats DEM pour une large gamme de nombre de Shields et pour des ratio de taille inférieurs à 4. Les résultats du modèle sont exploités pour identifier quatre régimes de transport différent selon les mécanismes responsables de la mobilité des petites particules.

Ce travail représente une avancée importante dans la compréhension de la ségrégation en transport sédimentaire par charriage et questionne notre compréhension des milieux granulaires bi-disperses encore peu étudiés. Il représente aussi une première étape dans le processus de changement d'échelle vers l'échelle morphologique par le biais de modèles continus.

Remerciements

Durant ces trois années de thèse, j'ai eu le plaisir de vivre une excellente aventure de recherche. Cela n'aurait pas été possible sans l'aide et la présence de nombreuses personnes que je souhaiterais maintenant remercier.

Tout d'abord, parce que tout ça commence bien avant la thèse, j'ai une pensée particulière pour toutes celles et ceux qui m'ont donné le goût de la recherche et m'ont encouragé vers la thèse. Je pense en particulier aux encadrants de mes différents stages de recherche : Frédéric Cyr, Pierre Augier, Andrea Filippini, Mario Ricchiuto et Philippe Bonneton.

Je voudrais remercier les membres de mon jury qui, malgré les conditions sanitaires particulières, ont su être présents (virtuellement) et ont permis que la soutenance, en visioconférence, garde un caractère particulier pour moi. Merci à mes deux rapporteurs, Eric Lajeunesse et Pierre-Yves Lagrée, d'avoir attentivement relu mon manuscrit de thèse et pour leurs commentaires. Merci également à Olivier Pouliquen d'avoir accepté de présider le jury et à Nico Gray pour sa présence et ses retours toujours très pertinents. Ce fut un honneur et un défi très motivant de défendre ma thèse devant vous.

En écrivant ces lignes, je pense bien sûr à mes trois encadrants de thèse avec qui j'ai eu l'immense chance et le plaisir de travailler. Tout d'abord, un grand merci Raphaël Maurin, pour ta sympathie et ta bonne humeur constante, pour ton suivi permanent et de qualité malgré la distance géographique, pour les longues discussions et les conseils. Tu m'as beaucoup appris et j'ai adoré travailler avec toi. J'espère qu'on continuera à interagir ensemble dans le futur (et qu'on ira enfin en montagne ensemble !). Je te remercie aussi, Julien Chauchat, pour ton expertise et ta vision que tu as su me transmettre. Notre interaction a été très riche, toujours source de motivation et je suis très content de continuer notre collaboration en postDoc. Enfin, je voudrais remercier chaleureusement Philippe Frey pour m'avoir fait confiance pour ce projet de thèse, pour ta présence exceptionnelle et l'encadrement hors du commun tout au long de ces trois ans. Ta vision transversale, plus "geo-morpho", m'a permis de toujours prendre du recul sur mon travail et de garder à l'esprit qu'une rivière c'est un peu plus que quelques billes dans une simulation. Nos discussions sont toujours très riches et ouvrent beaucoup de perspectives sur les résultats.

Merci à Hugo, mon compagnon de bureau et de recherche, pour les longues journées passées au tableau à essayer de comprendre les mystères des milieux granulaires, à faire et defaire les théories, à tout remettre en question pour parfois toucher du doigt un concept qui nous échappait jusqu'alors. Ce fut un plaisir de partager ces moments de recherche avec toi et je te souhaite bon courage pour ta dernière année de thèse.

À l'IRSTEA (INRAE), j'ai eu la chance de trouver un cadre idéal pour effectuer ma thèse. Merci à tous pour la bonne humeur quotidienne et les bons moments passés avec vous. Merci à Florence pour le soin particulier que tu portes à l'ensemble des doctorants, à Christian pour l'atelier vélo et ta bonne humeur permanente, à Xavier, Hervé et Firmin pour m'avoir emmené avec vous plusieurs fois sur le terrain voir de vrais cailloux, à

Guillaume pour les sorties grimpe le midi. Je pense également à tous les amis “doctorants”: Antoine, Félix, Ségolène, Hugo L., Hugo R., Charlie, Cécile et Cecile, Erwan, Coline, Suzanne et Franziska... Merci à vous tous pour les moments conviviaux, pour les sorties montagnes et ailleurs.

Parce que je n'ai pas passé ces trois ans qu'au labo, je souhaite aussi remercier mes amis et mes proches pour leur soutien et les bons moments passés ensemble. Je pense en particulier à Gontran, Coline, Esteban, Julie, Audrey, Juliette et Benjamin, à mes parents et mes frères.

Enfin, merci Estelle pour le soutien sans faille, et pour cette aventure initiée à deux. J'ai pris un peu d'avance sur toi, rattrape moi vite. Bon courage pour ces quelques derniers mois de thèse.

Contents

List of Figures

List of Tables

Chapter 1

Introduction

Everyone has been through this awkward moment when, at the end of a box of muesli, only crumbs remain to be eaten, while we could enjoy nice large pieces at the beginning of the box. This phenomenon of particle sorting by size has been called size segregation. The literature also refers to it as the *Brazil-nut* effect because it was discovered when transporting Brazil nuts by truck on bumpy roads. When delivered, the Brazil nuts were found sorted by size due to the induced vibrations.

Size segregation has huge implications for industrial applications, in which a perfect mixture is often desired. For instance, size segregation can alter the resistance properties of concrete due to the migration of aggregates (ACI committee 238, 2008; Navarrete and Lopez, 2017) (see figure 1.1a). For the pharmaceutical industry, the non-uniformity of powder mixtures due to segregation can lead to non acceptable quality of tablets and capsules (Carson, 1988). Segregation can also be a useful tool to ensure the selection of a particular class of grains. As an example, just after harvest and before the transfer into barrels, grapes pass through a vibrating sorting table (see figure 1.1b) allowing the removal of small debris such as small leaves, overly-mature fruits or insects. Size segregation is also a main feature of geophysical flows such as debris flows, pyroclastic flows, snow avalanches and sediment transport. During these granular flows, the larger elements rise to the surface and often collect at the front. Even astrophysical applications are concerned by segregation. A recent study (Perera et al., 2016) has shown that size segregation could explain the presence of large blocks at the surface of asteroids as illustrated in figure 1.1c.

Beyond size segregation, sorting of particles occurs as soon as there exist property differences, such as density (Shi et al., 2007; Tripathi and Khakhar, 2011a), shape (Pollard and Henein, 1989) or friction (Srebro and Levine, 2003; Ulrich et al., 2007). However size segregation is certainly the most studied and efficient segregation phenomenon.

Plenty of mechanisms are responsible for size segregation with a huge phenomenology depending on the geometry of the system, the size ratio between large and small particles or the granular flow regime (Thomas, 2000). For large size ratios, the small particles can percolate spontaneously by gravity, without external forcing, into the bed of larger particles (Bridgwater and Ingram, 1971; Dudill et al., 2017). For the smaller size ratios, typically below six, spontaneous percolation is not possible without deformation of the granular bed, which can be achieved by shearing or vibrating. This dynamic segregation results from the combination of kinetic sieving (Middleton, 1970) and squeeze expulsion

(a) (b) (c)

Figure 1.1: (a): Manisfestation of segregation of coarse aggregates in a concrete pillar (adapted from Guo et al. (2020)). (b): Vibrating sorting table to separate fruit from non desired small particles. Top: a sieve allows the automatic elimination of small particles. Down: the larger elements (bunches, leaves) are removed by hand (vineyard 2020 at Mas des Auribelles, personal pictures). (c): Itokawa asteroid which surface is composed of large boulders (credit: JAXA).

(Savage and Lun, 1988). When sheared, the granular material dilates and creates gaps, as the layers of particles flow past one another. Kinetic sieving is based on the idea that, under the action of gravity, small particles are more likely to fall down into the created gaps than the large particles, because they are more likely to fit into the available space. This process competes against squeeze expulsion, which tends to push all particles upwards with the same probability. The combination of both processes, which for brevity will just be called gravity driven segregation (Gray, 2018), results in a net downward flux of small particles and an upward flux of large grains, leading to an inversely graded bed. This PhD thesis focuses on gravity driven segregation in the context of bedload transport.

1.1 Context

Sediment transport is of major importance to understand the geomorphological evolution of rivers, their management and their interactions with human infrastructures such as dams, bridges or cities. During floods, huge amounts of sediments can be transported leading to natural hazards as illustrated in figure 1.2. One of the main challenges is therefore to be able to predict the amount of transported sediments and the associated morphodynamics.

In river streams, the transport of sediment can be decomposed into two modes of transport, suspended load and bedload. Suspended load is the transport of the smallest sediments, from sand to clay, directly suspended in the water column under the effect of

(a)

(b)

Figure 1.2: (a) Deposited sediment after the 2005 flood of the Domenon river in Domène (France). (b) Destroyed shop by the sediment transported by the Saltine river in Brigue (Switzerland). Credits for the pictures: P. Belleudy and R. Loat

flow turbulence. Bedload is the transport of larger sediment particles, from sand to gravels, by rolling, sliding and saltating on top of the mobile sediment bed. While suspended load is often larger in mass, bedload transport represents the main contribution to riverbed evolution. In gravel bed rivers, it may even represent the main contribution of the total solid transport rate (Turowski et al., 2010). The present PhD thesis focuses on the bedload transport regime.

The morphological evolution of river beds depends on the erosion and deposition budget and is therefore related to transport, which is the key parameter to predict. In order to establish bedload transport laws, one classically tries to relate the dimensionless transport rate, or Einstein parameter (Einstein, 1942), defined as

$$Q_s^* = \frac{Q_s}{((\rho^p/\rho^f - 1)gd^3)^{1/2}}, \tag{1.1}$$

to the dimensionless fluid bed shear stress, or Shields number (Shields, 1936), defined as

$$\theta = \frac{\tau_b^f}{(\rho^p - \rho^f)gd}, \tag{1.2}$$

where Q_s is the transport rate per unit width, ρ^p (resp. ρ^f) is the particle density (resp. fluid density), g is the acceleration of gravity, d is the bed surface characteristic particle diameter and τ_b^f is the fluid bed shear stress. The relation between the Einstein parameter and the Shields number has been studied extensively both experimentally (Gilbert, 1914; Meyer-Peter and Müller, 1948; Rickenmann, 1991; Recking et al., 2009; Lajeunesse et al., 2010) and theoretically, through mechanical (du Boys, 1879; Kalinske, 1947; Bagnold, 1956; Charru et al., 2004) and statistical approaches (Einstein, 1942; Fernandez-Luque and Van Beek, 1976; Parker et al., 2000; Ancey et al., 2008; Furbish et al., 2012). This has led to the formulation of many transport laws, the most common of which is certainly

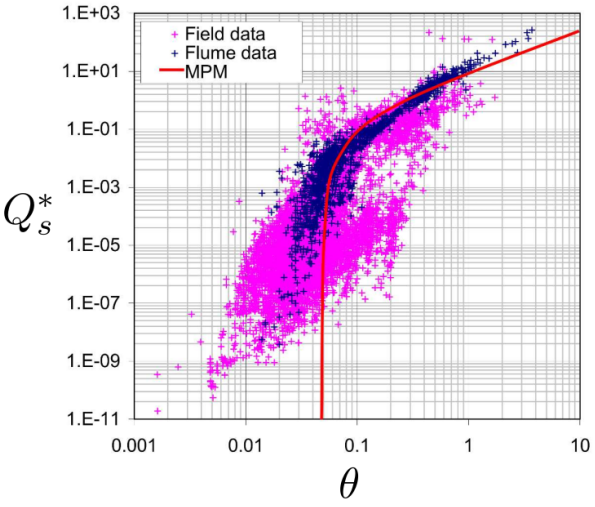

Figure 1.3: Compilation of 8700 field data in more than 100 rivers and 1317 flume data. The Meyer-Peter and Müller (1948) formula (MPM) is also plotted for comparison.

the Meyer-Peter and Müller (1948) formula

$$Q_s^* = 8\left(\theta - \theta_c\right)^{3/2}, \tag{1.3}$$

where θ_c is the critical Shields number, which corresponds to a threshold value below which sediments are in principle not transported. Most transport laws have the same formulation as equation (1.3) but with a different prefactor or power-law exponent. However, despite more than a century of research, bedload transport formulae still fail to predict accurately the measured transport rate. Figure 1.3, adapted from Recking et al. (2013), shows a compilation of flume and field data together with the Meyer-Peter and Müller (1948) formula. This formula has the right trend but can differ up to six orders of magnitude with the measured data, in particular close to the threshold of motion. Defining a critical Shields number from the data is not obvious at all and the large dispersion of the data indicates that the Einstein and Shields numbers are not the only relevant parameters to describe bedload. It seems therefore that some transport mechanisms are missing in the classical description of bedload.

Among the numerous possible missing mechanisms, it has recently been pointed out in the literature three main challenges for bedload transport that need to be addressed. First, Whitaker and Potts (2007) and Dhont and Ancey (2018) have evidenced the intermittent nature of bedload transport, with space and time variations of the data up to one order of magnitude for the same fluid forcing. Understanding these fluctuations in transport would improve our capacity to predict the morphological evolution of gravel bed rivers.

Second, the definition of the critical Shields number is very difficult and lead to several consistency problems (Pähtz et al., 2020). Close to the threshold of motion, the initiation of motion is strongly related to fluid velocity fluctuations, which can be strong enough to transport particles while the mean flow is too weak. It is therefore difficult to clearly

separate flow with and without transport. In addition, the incipient threshold of motion (by accelerating slowly the fluid) is not the same than the cessation threshold of motion (by decelerating the fluid). This hysteresis effect is classically attributed to particle inertia but a recent study suggests that it could also be due to inter-particle friction (Perrin et al., 2019). Finally, even for Shields numbers close to zero, some authors have been able to measure a very slow granular flow (Paintal, 1971; Houssais et al., 2015). These flows, also called creeping flows, have led some authors to question the existence of a critical shear stress (Lavelle and Mofjeld, 1987). In addition to these consistency problems, the critical Shields number is also expected to depend on the particle diameter, inertia, shape, friction, cohesion... All these complexities are well illustrated in figure 1.3 with large dispersion of data at low Shields numbers.

Another reason for our inability to predict accurately the transport rate is the polydispersity of the grain size distribution (Bathurst, 2007; Ancey, 2020), the focus of this PhD work. The mobility of the sediment bed is actually highly influenced by its size distribution. This has been mainly investigated from hydrodynamics perspectives. Indeed, for a given fluid forcing, the ratio between the fluid drag contribution and the buoyant weight of the particle is inversely proportional to the diameter, so that small particles are more transported than larger ones. In addition to this size-controlled effect, the presence of grains of different sizes alters the sediment exposition to the fluid flow and thereore modifies the bed mobility. In 1914, Gilbert (1914) was one of the first to observe experimentally that the introduction of finer sediments led to an increase of sediment mobility. This has then been studied extensively due to strong implications on fluvial morphology (Wilcock, 1993; Houssais and Lajeunesse, 2012; Dudill et al., 2017, 2018). It is generally observed that, in polydisperse beds, the mobility of smaller grains is decreased while that of larger grains is increased (Wilcock, 1993; Parker et al., 1982; Houssais and Lajeunesse, 2012). For instance small grains can be protected from the water flow by larger grains (see figure 1.4) reducing their mobility. In transport laws, the simplest way to deal with polydispersity is to define a characteristic surface sediment diameter based on the grain size distribution, classically d_{50}, the median surface diameter, or d_{84} (84% of the sediment is smaller than d_{84}) (Recking, 2013). This approach considers that the sediment bed behaves like an equivalent monodisperse bed of modified diameter but it does not take into account size interactions between grains, nor possible differences in the grain mobility due to their size. A more complex approach consists in modelling the transport of each class separately and to introduce empirical hiding functions in transport laws (Egiazaroff, 1965; Parker et al., 1982; Powell et al., 2001; Wilcock and Crowe, 2003; Houssais and Lajeunesse, 2012). These hiding functions allow the modification of transport law coefficients and critical Shields numbers of each class in order to account for relative size effects.

In addition to these hydrodynamic considerations, the complex relations between grains of different sizes can be the result of granular interactions and in particular of size segregation. Indeed, Frey and Church (2011) and Ferdowsi et al. (2017) have shown that the formation of armoured layers (see figure 1.4) is also a granular phenomenon, with large gravels rising up to the surface and smaller grains infiltrating the bed. It seems therefore necessary to adopt a complementary granular approach to study the mechanisms

(a) (b)

Figure 1.4: Field manifestation of size segregation. (a) Top view of Archiane stream (France). After removing the first large rocks of the surface armoured layer, smaller rocks are found protected below (personal picture). (b) Vertical profile in a gravel river bar in Vedder River, British Columbia, (Canada) (adapted from Frey and Church (2009))

controlling and responsible for size segregation in bedload transport and their consequences on the mobility of bidisperse beds.

The granular communities have already started to investigate the granular mobility question. In particular, due to strong implications for industrial applications and most geophysical flows (debris flows, pyroclastic flows or snow avalanches), they studied the influence of the slope (Mangeney et al., 2010; Farin et al., 2014; Maurin et al., 2018), basal friction (Chedeville and Roche, 2014; Edwards et al., 2017), total volume (Staron and Lajeunesse, 2009) and polydispersity (Phillips et al., 2006; Linares-Guerrero et al., 2007; Iverson et al., 2010; Lai et al., 2017) on particle mobility. Concerning the effect of polydispersity, Linares-Guerrero et al. (2007) measured, with two dimensional Discrete Element Method (DEM) simulations, the run-out distance of dry bidisperse granular avalanches. They observed an increased mobility of the avalanche due to the presence of small particles segregating at the base of the granular flow and acting as a lubrication layer. Similarly, Lai et al. (2017) with DEM and laboratory experiments of granular collapse with fractal size distributions, observed the formation of a basal small particle layer increasing the total mobility. In bedload transport, vertical size segregation is often identified as a main mechanism responsible for the increased mobility of polydisperse beds. In laboratory experiments with natural materials, Recking et al. (2009) and Bacchi et al. (2014) showed that, under certain conditions, due to kinetic sieving, small particles smooth the bed subsurface and make the above large particles more mobile. In bedload transport laboratory experiments with a bidisperse bed, Dudill et al. (2018) observed that the finer particles, after having infiltrated the first uppermost layers, increased drastically the sediment mobility. It seems therefore that size segregation, and in particular the formation of a small particle layer below large ones, plays an important role in the increased mobility process. Despite the few studies presented above, there is still no clear understanding of

the physical mechanisms responsible for the increased mobility of polydisperse mixtures.

The classical hydrodynamic approach of polydispersity in bedload transport only takes into account the surface state of the bed. The literature above however shows that the depth structure of the bed also impacts the sediment mobility. This opens two main questions. First, how is built this vertical structure ? Or in other words, what are the mechanims at the origin and controlling size segregation during bedload transport ? And secondly, how does it affect the sediment mobility and what are the associated granular mechanisms ? This PhD study tries to answer these two questions.

In order to address this sediment mobility problem, the analysis given above shows the necessity to adopt a complementary granular point of view (Frey and Church, 2009, 2011) and to understand size segregation mechanisms. This would benefit both the granular and geomorphological communities. In the following sections, a literature review on size segregation and its modelling is presented and commented in the perspective of bedload transport.

1.2 Size segregation in granular media

Particle-size segregation has strong implications for the study of both geomorphology and granular media in general. Gravity driven segregation has been studied experimentally and numerically in multiple configurations such as dry granular avalanches (Savage and Lun, 1988; Dolgunin and Ukolov, 1995; Wiederseiner et al., 2011; Fan et al., 2014; Jones et al., 2018), shear cells (Golick and Daniels, 2009; May et al., 2010; Van der Vaart et al., 2015; Fan and Hill, 2015; Fry et al., 2018), annular rotating drums (Gray and Ancey, 2011) and bedload configurations (Ferdowsi et al., 2017; Lafaye de Micheaux et al., 2018; Frey et al., 2020). However no general satisfying description has been proposed yet.

In order to identify the mechanisms and comment on the literature on gravity driven segregation, a dimensional analysis is performed. This analysis is made in the dry limit case, consistent with the results of Maurin et al. (2016) showing that the fluid (here water) just acts as a forcing mechanism in turbulent bedload transport and has only secondary effects on the granular behaviour. Therefore, the fluid is not considered as an influencing parameter for this granular segregation configuration. The different variables of the problem are

$$d_s, \quad d_l, \quad \rho_p, \quad g, \quad \phi_s, \quad \dot{\gamma}^p, \quad P^p, \quad w_s, \tag{1.4}$$

where d_s (resp. d_l) is the diameter of small (resp. large) particles, ϕ_s is the local concentration of small particles, ρ_p is the particle density, $g = 9.81$ m.s^{-2} is the gravitational acceleration, $\dot{\gamma}^p$ is the particle shear rate, P^p is the granular pressure and w_s is the segregation velocity of the small particles. These eight variables involve only three units (length, time and mass), so the problem depends on five dimensionless groups. Choosing d_l, $\sqrt{d_l/g}$ and $\rho_p d_l^3$ as reference length, time and mass units respectively, the following

relation is obtained

$$\frac{w_s}{\sqrt{gd_l}} = \mathcal{G}\left(r, \phi_s, \sqrt{\frac{d_l}{g}}\dot{\gamma}^p, \frac{P^p}{\rho_p d_l g}\right), \tag{1.5}$$

where $r = d_l/d_s$ is the size ratio between large and small particles and $\mathcal{G}$ is an unknown function. It is assumed that relation (1.5) can be written in a power law form for the dimensionless shear rate and pressure and that the effects of each variables are decoupled,

$$\frac{w_s}{\sqrt{gd_l}} \propto \left(\sqrt{\frac{d_l}{g}}\dot{\gamma}^p\right)^{\zeta} \left(\frac{P^p}{\rho_p d_l g}\right)^{\eta} \mathcal{G}_1(r)\mathcal{G}_2(\phi_s), \tag{1.6}$$

where the function $\mathcal{G}_1$ should vanish when $r = 1$ in order to cancel segregation in the monodisperse limit.

In the theory of Savage and Lun (1988), the shear rate $\dot{\gamma}^p$ is predicted to be an important controlling parameter for the rate of particle-size segregation. This is based on the observation that as particles flow downslope, shearing allows each layer of particles in the flow to move faster than the one beneath and hence the rate of finding gaps to fall into is expected to be proportional to the shear rate. Savage and Lun (1988) showed that this assumption produced good agreement between the theory and bidisperse experimental flows down inclined planes. More recently, DEM simulations of dry bidisperse mixtures in heap flows (Fan et al., 2014) have also found a linear relation between the segregation velocity and the shear rate. However, the annular shear cell experiments of Golick and Daniels (2009) suggest that the segregation-rate is also pressure dependent, since the segregation rate dramatically decreased when a large pressure was applied on the top plate of their shear cell. This pressure dependence has also been observed in the DEM simulations of Fry et al. (2018), who found a power law relating the segregation velocity to the inertial number I (GDR MiDi, 2004). A scaling with the inertial number represents an extension of the Savage and Lun (1988) theory in order to take into account both the effect of the shear rate and pressure on segregation. It corresponds in equation (1.6) to $\eta = -\zeta/2$, which can be rewritten as

$$\frac{w_s}{\sqrt{gd_l}} \propto I^{\zeta}\mathcal{G}_1(r)\mathcal{G}_2(\phi_s), \tag{1.7}$$

with I the inertial number based on the large particle diameter defined as

$$I = \frac{d_l\dot{\gamma}^p}{\sqrt{P^p/\rho_p}}, \tag{1.8}$$

suggesting that the segregation velocity is a function of the inertial number, the size ratio and the local concentration.

The size ratio between large and small particles r is also a key parameter for size segregation. In the annular shear cell, Golick and Daniels (2009) showed that the segregation velocity is an increasing function of the size ratio with a maximum around $r = 2$. This effect was also observed in both two-dimensional (2D) and three-dimensional (3D) DEM

simulations of sheared granular flows (Guillard et al., 2016; Thornton et al., 2012).

The effect of the small particle concentration ϕ_s has also been widely studied, and different forms for $\mathcal{G}_2$ have been proposed (Bridgwater et al., 1985; Savage and Lun, 1988; Dolgunin and Ukolov, 1995; Gray and Thornton, 2005; May et al., 2010; Gajjar and Gray, 2014; Van der Vaart et al., 2015; Fan et al., 2014). The small particles have been shown to segregate less easily if they are more concentrated and the downward velocity should vanish for a pure phase of small particles. For this purpose, the simplest form $\mathcal{G}_2(\phi_s) = 1 - \phi_s$, has been proposed by Dolgunin and Ukolov (1995). In oscillating shear cell experiments, Van der Vaart et al. (2015) measured the time necessary to achieve complete segregation with an initial mixture ranging from one small particle segregating into a bed of large particles, to a single large particle rising up through a small particle bed. They observed that both extreme cases were not symmetric, resulting in an asymmetry of the vertical velocity with the concentration, and Gajjar and Gray (2014) proposed a quadratic dependence of $\mathcal{G}_2$ on ϕ_s. Fan et al. (2014) and Jones et al. (2018) also observed this non-linearity in dry bidisperse avalanche simulations, but concluded that the form of Dolgunin and Ukolov (1995) is still a good first order approximation.

This literature review on dry granular flows underlines the qualitative understanding of size-segregation for simple flow configurations. Bedload transport can be seen as a granular flow, where the fluid forcing induces strong velocity gradients in the vertical direction and a somewhat more complex granular forcing, which could challenge the classical picture of segregation. Few studies have been published on gravity driven segregation in bedload transport and more remains to be done for a clear understanding of the processes at play. Ferdowsi et al. (2017) experimentally studied size segregation in laminar bedload transport and performed dry granular flow simulations. They studied the formation of armour, i.e. the segregation of large particles to the top, starting from a mixture of small and large particles. They showed that the process seems to be a granular phenomenon and reproduced their experimental results in the framework of continuum segregation modelling, using a generalization of the Gray and Thornton (2005) segregation model. Hergault et al. (2010) and Frey et al. (2020) studied experimentally size-segregation in turbulent bedload transport, considering a quasi-2D channel enabling particle tracking. They found that the particles move down as a layer into the bed, and related the segregation velocity to the granular shear rate.

While the literature review presented above underlines the progress in the understanding and modelling of gravity driven segregation, more physically-based parameterizations for a continuum segregation model are still lacking, in particular in the complex turbulent bedload transport configuration. In addition, no general description of size segregation, that would be valid in all configurations, has been proposed yet. From a geomorphological point of view, the impact of size segregation on transport rate is not well understood and an effort is still needed in the development of models able to represent size segregation at the river scale.

1.3 Size segregation modelling

Modelling size segregation is considered as one of the main challenges for bedload transport (Ancey, 2020) and for the understanding of granular flows in general (Andreotti et al., 2013). This is however quite a recent subject of research. So far, segregation has been mainly investigated on the one hand at the particle scale, trying to model the forces applied on a single intruder. On the other hand, continuum models describing size segregation for an assembly of particles of different sizes have been proposed. The latter approach has been succesfully used to represent size segregation experiments and will be applied in the bedload configuration in this PhD work. Existing continuum models however still lack strong physical fondations that would rely on the particle scale forces applied on an intruder and would bring information on the physical mechanisms at play during size segregation. This section therefore reviews and comments on these two different approaches.

1.3.1 Particle scale modelling

At the particle scale, one generally considers the evolution of one or several intruders in a bath of other homogeneous particles. The intruder can have a different shape, size or density than other particles and segregation is analysed in terms of force. The migration of the intruder is seen as the result of a destabilizing lift force (Ding et al., 2011), or segregation force, together with a resistive drag force (Tripathi and Khakhar, 2011a, 2013) due to the relative motion with surrounding particles. Among the few existing studies, the lift force has been measured to be a buoyancy-like force (Tripathi and Khakhar, 2011a, 2013; Guillard et al., 2014, 2016), or Saffman lift force (Van der Vaart et al., 2018). Another approach, proposed by Staron (2018), considers that the migration of the intruder is not driven by a lift force but by force fluctuations, challenging the classical view of segregation. In this section, the investigations of Tripathi and Khakhar (2011a) on density segregation and Guillard et al. (2016) on size segregation are presented and interpreted in the bedload configuration. In these papers, the authors have been able to isolate and to clearly identify the forces during segregation.

Tripathi and Khakhar (2011a) proposed a granular Stokes experiment. They performed DEM simulations of a settling heavy particle in a dense flow down an incline made of light spheres but with the same particle size (see figure 1.5a). They measured the velocity and the forces applied on the intruder and demonstrated that it was submitted to three different forces. The first is its own weight $P = -\rho^I V g cos(\alpha)$, where ρ^I is the intruder density and V is its volume. Assuming that the surrounding lighter particles can be considered as an equivalent fluid, a buoyancy force also applies on the intruder. With an analysis in the limit of similar particle density, they showed that it is similar to a fluid buoyancy force as $F_b = \rho^p V g cos(\alpha)$, where ρ^p is the density of the surrounding particles. Finally, by analogy with hydrodynamics, they showed that, in dense flow conditions, the intruder is also submitted to an inter-particle drag force which follows a Stokesian form

$$F_d = -c(\Phi)\pi d\eta^p(w_I - w_p), \tag{1.9}$$

where $c(\Phi)$ is the drag coefficient, d is the particle diameter, Φ is the solid volume fraction defined as the portion of the space occupied by the solid phase, $\eta^p = |\tau^p_{xz}|/\dot{\gamma}^p$ is the granular viscosity with τ^p_{xz} the granular shear stress, w_I is the settling intruder velocity and w_p is the bulk vertical velocity. Tripathi and Khakhar (2011a) found the drag coefficient to have a slight dependency with the solid volume fraction Φ and to be of the order of the fluid viscous drag coefficient, $c \sim 3$. Similar to a fluid drag force, the particle drag force can be associated to a particle Stokes number

$$St^p = \frac{\rho^p d_I \sqrt{g d_I}}{6 c \eta^p}, \tag{1.10}$$

which compares the inertia of the intruder with the viscosity of the surrounding particles.

With these three different forces, the force balance on the intruder can be written as

$$\begin{aligned} \rho^I V \frac{dw_I}{dt} &= P + F_b + F_d \\ &= -(\rho^I - \rho^p) V g \cos(\alpha) - c\pi d \eta^p (w_I - w_p). \end{aligned} \tag{1.11}$$

Tripathi and Khakhar (2011a) verified this equation at steady state, i.e. with $dw_I/dt = 0$. The parralel with hydrodynamics is direct here. The intruder sinks if its weight is stronger than the buoyancy force. The forcing mechanism for density segregation is therefore the gravitational force. Note that in the limit $\rho^I \to \rho^p$, the gravity term in the right hand side vanishes and the equation of motion becomes a simple relaxation equation without segregation. The difference with hydrodynamics lies in the limit of non moving particles. Indeed, while an object can sink in a fluid at rest, the intruder can only segregate if the surrounding particles are moving. However, defining the particle drag force for a granular bed at rest is not trivial, as the granular viscosity becomes infinite. This case is therefore discarded in this study.

Let us consider now an intruder of the same density but different size than surrounding particles. According to the previous analysis, the granular buoyancy force F_b balances exactly the weight P of the intruder and there is no destabilizing force anymore in equation (1.11). This means that there exists another destabilizing force, that is called segregation force in the following, responsible for the migration of an intruder of different size. To be consistent with equation (1.11) the segregation force should vanish when the size ratio between the intruder and surrounding particles is close to 1. In order to determine the segregation force, Guillard et al. (2016) performed two-dimensional (2D) DEM simulations of particle scale size segregation. They considered a 2D granular medium made of disks of diameter d_s, with an intruder of diameter d_I. They measured the segregation force when applying a gravitational field (see figure 1.5b). The mixture was confined by a plate of glued particles and sheared. A virtual spring is attached to the intruder. While the large intruder rises up, the spring elongates. The originality of this work is that once the steady state is reached, the intruder does not move and the drag force vanishes. Therefore at steady state, the particle is submitted to its own weight, to the granular buoyancy force, to the segregation force and to the spring force and these forces equilibrate exactly.

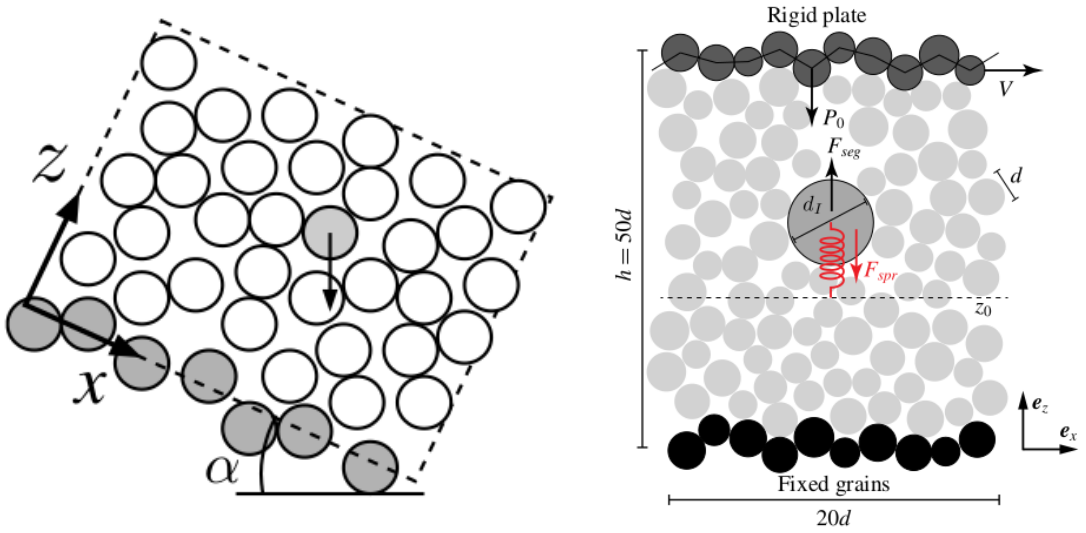

(a) (b)

Figure 1.5: (a) Schematic view of the density segregation system (adapted from Tripathi and Khakhar (2011a)). A heavy intruder of mass m_I surrounded by lighter spheres. (b) Schematic view of the size segregation system (adapted from Guillard et al. (2016)). A large intruder in a shear cell with smaller particles.

Measuring the spring force and substracting the weight of the intruder, they were able to measure the sum of the granular buoyancy force and segregation force (they did not distinguish these two forces in their article). They found it to be proportional to the granular stress gradients as

$$F_b + F_{seg} = -V_I \left(\mathcal{F}(\mu, r) \frac{\partial P^p}{\partial z} + \mathcal{G}(\mu, r) \frac{\partial |\tau^p_{xz}|}{\partial z} \right), \tag{1.12}$$

where V_I is the volume of the large intruder, $\mathcal{F}$ and $\mathcal{G}$ are two empirical functions depending on the friction coefficient $\mu = |\tau^p_{xz}|/P^p$ and the size ratio $r = d_I/d_s$. In the bedload configuration, the slope is commonly small ($\tan(\alpha) < 20\%$). The pressure gradient being proportional to the cosine of the slope and the shear stress gradient to the sine of the slope, the second term of equation (1.12) can be neglected and

$$F_b + F_{seg} = -V_I \mathcal{F}(\mu, r) \frac{\partial P^p}{\partial z}. \tag{1.13}$$

Assuming that the pressure is hydrostatic, $\partial P^p/\partial z = -\Phi \rho^p g \cos\alpha$, and using the expression of the granular buoyancy force introduced by Tripathi and Khakhar (2011a), the latter can be written $F_b = -V_I/\Phi \partial P^p/\partial z$ yielding the following expression for the segregation force

$$F_{seg} = -V_I \left(\mathcal{F}(\mu, r) - \frac{1}{\Phi} \right) \frac{\partial P^p}{\partial z}. \tag{1.14}$$

The segregation force can therefore be interpreted as a default of buoyancy. Guillard et al. (2016) found $\mathcal{F}$ to depend on μ as $\mathcal{F}(\mu) = 2.4 + 0.73\exp(-(\mu - \mu_c)/0.051)$, for $\mu > \mu_c$ where μ_c is the static friction coefficient. $\mathcal{F}$ also depends on the size ratio r. They observed it to be maximum for $r = 2$ but did not provide any expression. As mentioned previously, the segregation force should vanish in the same size particle limit (no destabilizing force when there is no size difference between the intruder and surrounding particles). This is equivalent to $\mathcal{F}(\mu, r = 1) = 1/\Phi$, which is indeed what is observed by Guillard et al. (2016) in their simulations.

Therefore, a segregating large particle in a small particle bed (without the spring), and remembering that the granular buoyancy force balances the weight of the intruder ($P = -F_b$), the equation of motion becomes

$$\begin{aligned} \rho^p V_I \frac{dw_I}{dt} &= P + F_b + F_{seg} + F_d \\ &= -V_I \left(\mathcal{F}(\mu, r) - \frac{1}{\Phi}\right) \frac{\partial P^p}{\partial z} - c\pi d_I \eta^p (w_I - w_p). \end{aligned} \tag{1.15}$$

In order to clearly identify the mechanisms responsible for density or size segregation, the approaches of Tripathi and Khakhar (2011a) and Guillard et al. (2016) can be combined. Considering an intruder of different size and density than surrounding particles, the equation of motion of the intruder is

$$\rho^I V_I \frac{dw_I}{dt} = -(\rho^I - \rho^p) V_I g \cos(\alpha) - V_I \left(\mathcal{F}(\mu, r) - \frac{1}{\Phi}\right) \frac{\partial P^p}{\partial z} - c\pi d_I \eta^p (w_I - w_p). \tag{1.16}$$

If $r = 1$, $\mathcal{F}(\mu, r = 1) = 1/\Phi$, and equation (1.11) is retrieved. If $\rho^I = \rho^p$, equation (1.15) for size segregation only is found. This equation highlights the different origins of segregation in density or size. In the case of density segregation, segregation is caused by the first term of the right hand side. The gravitational force being stronger than the buoyancy force applied by the surrounding particles, this is a simple gravitational mechanism. In the case of size segregation, the first term of the right hand side vanishes and segregation is caused by the second term, corresponding to a default of buoyancy. In this equation the particle drag force due to the surrounding small particles is equivalent to a damper. It slows down segregation and scales with the granular viscosity and the intruder velocity. Note that in this equation, the rise of the intruder is a function of the granular state of the bed. The segregation force depends on the friction coefficient and on the granular pressure gradient and the resistive force on the granular viscosity and on the bed velocity.

This equation highlights the mechanisms responsible for size segregation at the particle scale and should predict the vertical motion of a single isolated intruder in a small particle bed. For numerous intruders, collective effects have to be taken into account and individual motions are not sufficient anymore to describe the migration of large and small particles. A continuum description is therefore preferable to the particle scale description.

1.3.2 Advection-diffusion model for size segregation

Modelling the size segregation phenomenon at the particle scale is computationally demanding and can only be achieved for small domains. In this context, one of the main challenges for segregation is to be able to upscale to macroscopic continuum modelling.

The classical approach is to consider each class of particles as a phase. A concentration is attributed to each class, corresponding to the portion of the granular volume occupied by the particles of the class. Since the first size segregation continuum model of Bridgwater et al. (1985), there have been plenty of models for segregation, the great majority of them in an advection or advection-diffusion form. The evolution of the small particle phase concentration can be described by a transport equation of the following form

$$\frac{\partial \phi_s}{\partial t} + \nabla \cdot (\phi_s \boldsymbol{u}) - \frac{\partial F_s(\phi_s)}{\partial z} = \nabla \cdot (D \nabla \phi_s)\,, \tag{1.17}$$

where ϕ_s is the small particle concentration, $\boldsymbol{u}$ is the bulk velocity field, F_s is the segregation flux and D is the diffusion coefficient. In this transport equation, small particles are advected both by the mean flow $\nabla \cdot (\phi_s \boldsymbol{u})$ and downward by a segregation flux $-\partial F_s(\phi_s)/\partial z$. A diffusion term $\nabla \cdot (D \nabla \phi_s)$ allows particles of one class to mix with others. The large particle concentration ϕ_l is obtained by the relation $\phi_s + \phi_l = 1$.

Models differ from each others by the way to derive and express the segregation flux F_s. Based on their kinetic sieving theory, Savage and Lun (1988) were the first to proposed an analytical expression of the segregation flux which depends on the granular shear rate $\dot{\gamma}^p$ and small particle concentration. Their expression however does not depend on gravity although it is driving size segregation. More recently, Gray and Thornton (2005) placed the problem in the mixture theory framework, and assuming ad-hoc granular interactions between phases, they were able to derive analytically an advection equation with a segregation flux depending on gravity. This model has then been extended to account for the presence of passive fluid (Thornton et al., 2006), for diffusion (Gray and Chugunov, 2006), for a third granular phase (Gray and Ancey, 2011) and for a continuous size distribution (Marks et al., 2012). Advection-diffusion models for segregation were also obtained based on the kinetic theory for granular gases (dilute regime) (López de Haro et al., 1983; Jenkins and Mancini, 1989; Khakhar et al., 1999; Ottino and Khakhar, 2000; Fan and Hill, 2015). The segregation flux is the sum of two distinct fluxes, which are proportional to the granular temperature gradient and to the granular pressure gradient. Similar to a real gas, the granular temperature characterises the kinetic energy of particle random motion and is computed with velocity fluctuations. The kinetic theory predicts that large particles migrate toward cold regions (low granular temperature) and small particles toward warm regions (high granular temperature). While this is verified for dilute granular flows, it fails to predict the correct segregation state in most dense flows.

To model segregation in dense bidisperse flows, the model of Gray and Thornton (2005) and extensions have been widely used to compare with DEM simulations (Fan et al., 2014) and laboratory experiments (May et al., 2010; Wiederseiner et al., 2011; Van der Vaart et al., 2015; Ferdowsi et al., 2017). These models are briefly presented thereafter but the

interested reader should refer to Gray and Thornton (2005), Thornton et al. (2006) and Gray and Chugunov (2006) for exhaustive description. This is a two phase flow model, each phase $\nu = l, s$ corresponding to the class of large and small particles respectively. Mixture theory assumes that each spatial point is occupied simultaneously by both phases. Because each phase shares space with the other, partial variables need to be defined, and each phase must satisfy a mass and momentum equation

$$\frac{\partial \rho_\nu}{\partial t} + \nabla \cdot (\rho_\nu \boldsymbol{u}_\nu) = 0, \tag{1.18}$$

$$\frac{\partial \rho_\nu \boldsymbol{u}_\nu}{\partial t} + \nabla \cdot (\rho_\nu \boldsymbol{u}_\nu \times \boldsymbol{u}_\nu) = -\nabla p_\nu + \rho_\nu \boldsymbol{g} + \boldsymbol{\beta}_\nu, \tag{1.19}$$

where ρ_ν is the partial density of class ν, p_ν is its partial pressure, $\boldsymbol{u}_\nu$ is its partial velocity, $\rho_\nu \boldsymbol{g}$ is the gravitational force and $\boldsymbol{\beta}_\nu$ is the interaction force applied by the other constituent on class ν.

The partial variables need to be related to physical variables and to bulk quantities. The partial density is computed accordingly to the portion of the space occupied by the phase $\rho_\nu = \Phi_\nu \rho^p$ (particles of both phases have the same density ρ^p) and the partial velocity is assumed to be the same than the bulk velocity in the streamwise direction, $u_\nu = u$, but different in the vertical direction, $w_s \neq w_l \neq w$, where $\boldsymbol{u} = (u, w)$ is the bulk velocity field. The main assumption of the Gray and Thornton (2005) model is that the particle phases do not share equally the bulk pressure (not proportionally to the concentration), i.e. $p_\nu = f_\nu P^p$ where $f_\nu \neq \phi_\nu$ and P^p is the bulk pressure. This unequal repartition of pressure is at the origin of size segregation in the model, small particles supporting less pressure than they should.

The interaction force is taken as $\boldsymbol{\beta}_\nu = P^p \nabla f_\nu - \rho_\nu c(\boldsymbol{u}_\nu - \boldsymbol{u})$. The first term has been introduced to delete one of the cross terms in the pressure gradient ($-\nabla p_\nu = -f_\nu \nabla P^p - P^p \nabla f_\nu$) and ensures that segregation is driven by intrinsinc pressure gradient $f_\nu \nabla P^p$. The second term is a linear granular drag force with a constant coefficient c (Morland, 1992). Of course in 2005, the particle scale studies of Tripathi and Khakhar (2011a) and Guillard et al. (2016) presented in the previous sub-section were not available and Gray and Thornton (2005) had to assume simple interactions between phases.

Introducing the expressions of partial density, partial pressure and interaction force in the momentum equation and assuming that the acceleration terms can be neglected, the vertical velocity w_ν can be isolated. Introducing the obtained expression and partial density in the mass conservation equation and assuming that the total volume fraction is constant $\Phi = Const$, the evolution of the small particle concentration is predicted by an advection equation

$$\frac{\partial \phi_s}{\partial t} + \nabla \cdot (\phi_s \boldsymbol{u}) - \frac{\partial F_s(\phi_s)}{\partial z} = 0, \tag{1.20}$$

with $F_s = (f_s - \phi_s) g / c \cos\alpha$ is the segregation flux, responsible for a vertical transport of particles. The segregation flux is proportional to $f_s - \phi_s$ which originates from the partial presure expression ($p_s = f_s P^p$). If the bulk pressure were equally shared between phases, the pressure proportion and the segregation flux would satisfy $f_s = \phi_s$ and $F_s = 0$,

meaning that small particles would just be advected by the mean flow without segregation. The segregation flux also depends on gravity g, the drag coefficient c and the slope α. With this equation, Gray and Thornton (2005) were the first to introduce analytically gravity in size segregation, representing an important step for segregation modelling.

In order to compute the segregation flux, a closure for f_s is still needed. Gray and Thornton (2005) proposed the following ad-hoc closure, $f_s = \phi_s - B\phi_s(1-\phi_s)$, yielding a non linear segregation flux $F_s(\phi_s) = -q\phi_s(1-\phi_s)$ with $q = B/cg\cos(\alpha)$, where B is an empirical constant which has to be adjusted on a case by case basis.

When considering bedload transport, the interstitial fluid also has to be modeled. Thornton et al. (2006) extended the Gray and Thornton (2005) model to account for the presence of a passive fluid. It results in the same equation as equation (1.20) with $q = B/c(\rho^p - \rho^f)/\rho^p g cos(\alpha)$, the fluid only acting through buoyancy to reduce gravity.

This model has been very successful because of its elegant derivation and its simplicity. It represented an important step to understand size segregation as it is based on particle scale forces and introduced gravity in the segregation process. However the segregation flux does not depend on bulk flow properties, while the litterature review evidenced the role of the inertial number. Indeed, it is expected from the previous section that the segregation velocity is in the form $w_s \propto \mathcal{G}_1(r)\mathcal{G}_2(\phi_s)I^\zeta$. F_s being a flux of small particles, it is related to the small particle velocity as $F_s = \phi_s w_s$. Considering the simplest linear form of Dolgunin and Ukolov (1995) $\mathcal{G}_2 = 1 - \phi_s$, one expects the segregation flux $F_s = \phi_s w_s$ to be in the form

$$F_s \propto \mathcal{G}_1(r) I^\zeta \phi_s(1-\phi_s), \tag{1.21}$$

This predicts a quadratic form for the segregation flux consistent with the one of Gray and Thornton (2005), but indicates that the prefactor should depend on the size ratio and on the inertial number while it was proposed constant by Gray and Thornton (2005). This absence of dependencies may come from the simplicity of the closures proposed by Gray and Thornton (2005), in particular the linear drag force and the expression of the partial pressure. A way to improve the model would be to integrate the segregation force of Guillard et al. (2016) and the more complex granular drag force of Tripathi and Khakhar (2011a) in the phase interaction term $\boldsymbol{\beta}_\nu$. Indeed both of these forces depend on the bulk flow properties via the friction coefficient and the granular viscosity.

The segregation model (1.20) is an advection equation with a non linear segregation flux $F_s \propto \phi_s(1-\phi_s)$. Such hyperbolic equations lead to shock formation and propagation of ϕ_s, that are not observed in practice. This is due to diffusive remixing effects which somewhat act in opposition to segregation to mix the phase of small and large particles. Gray and Chugunov (2006) introduced diffusive remixing in the Gray and Thornton (2005) model as a simple diffusion process, resulting in the following advection-diffusion model

$$\frac{\partial \phi_s}{\partial t} + \nabla \cdot (\phi_s \boldsymbol{u}) - \frac{\partial F_s}{\partial z} = \nabla \cdot (D \nabla \phi_s), \tag{1.22}$$

where D is the diffusive remixing coefficient of the phase of small particles into the phase of large ones. In granular flows, diffusion has been mainly studied in the case of self-

diffusion, for which the diffusion coefficient is measured to be proportional to the shear rate (Campbell, 1997; Utter and Behringer, 2004). The diffusion mechanism considered in equation (1.22) is the mixing of one class of particles into another. This kind of diffusion is expected to be related to self-diffusion but this has been barely studied (Cai et al., 2019).

The advection-diffusion model has shown its ability to reproduce experimental measurements and numerical simulations of size segregation in different configurations (May et al., 2010; Wiederseiner et al., 2011; Fan et al., 2014; Van der Vaart et al., 2015; Ferdowsi et al., 2017). As already mentioned, the expressions of the segregation flux and of the diffusion coefficient however rely on empirical closures with coefficients that need to be adjusted case by case. A more general description of size segregation with the advection-diffusion model, that would be valid in all configurations, is therefore needed.

1.4 Objectives and scope

This PhD thesis is at the starting point of a long and challenging upscaling process: taking into account size segregation in the prediction of sediment transport, understanding and modelling the impact of size segregation on geomorphological evolutions. Following and taking inspiration from the previous works performed at INRAE (formerly Irstea and Cemagref) by Hergault (2011), Maurin (2015), Dudill (2016) and Lafaye de Micheaux et al. (2018), the present study focuses on the small scales, as pictured in figure 1.6, keeping in mind that the final objective is to upscale toward the river scale. The primary purpose of this PhD thesis is to study, at the particle scale, size segregation during bedload transport with DEM simulations, in order to understand the mechanisms controlling size segregation and its impact on sediment transport. A second objective is to propose a first step toward continuum modelling at larger scales.

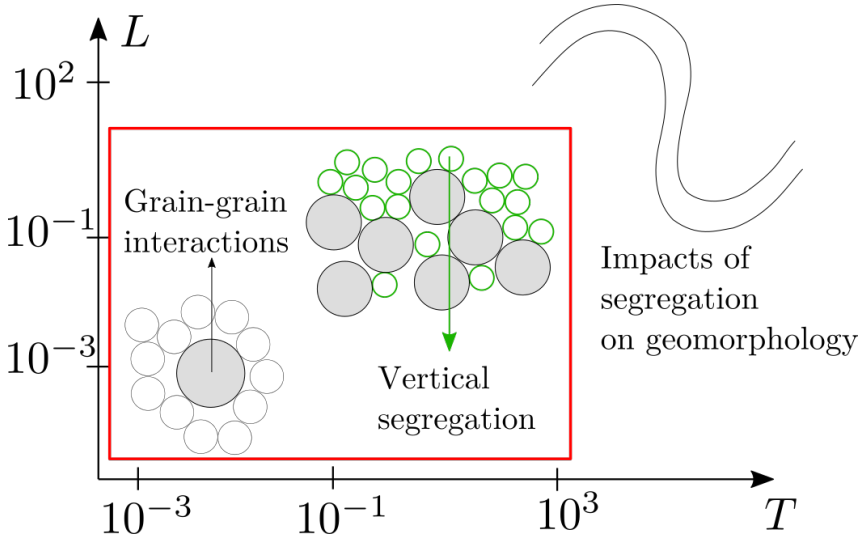

Figure 1.6: The time (T) and space (L) scales of the segregation problem in bedload transport. This PhD thesis focuses on the smaller scales as identified by the red square.

The coupled fluid DEM model developed by Maurin et al. (2015) has been adapted to bidisperse configurations and is presented in chapter 2. Based on the dimensional analysis performed in the present introduction, the DEM model is used in chapter 3 to study the mechanisms controlling size segregation during bedload transport and to improve continuum modelling of size segregation with the advection diffusion model. Starting from the particle scale forces presented in section 1.3.1, a new physically-based advection-diffusion model for size segregation has been derived by Hugo Rousseau, current PhD student at INRAE. In chapter 4, this model is numerically solved and interpreted in the light of the obtained results with the DEM simulations. Enhanced sediment mobility, as a consequence of size segregation, is studied in chapter 5 with DEM simulations of already segregated bidisperse beds. Last, conclusions and perspectives are proposed in chapter 6.

Chapter 2

Presentation of the discrete model, continuous framework and bedload transport configuration

This chapter first presents the coupled fluid-DEM model used in this PhD thesis to study size-segregation. Then, using a monodisperse simulation, the bedload configuration is presented and analysed in a continuous two-phase (Eulerian-Eulerian) framework. These descriptions will be used as a basis for the developments all along this PhD thesis.

2.1 A Coupled fluid-DEM model

The numerical model used to simulate size-segregation in turbulent bedload transport is a three-dimensional Discrete Element Method (DEM) using the open-source code YADE (Smilauer et al., 2015) coupled with a one-dimensional turbulent fluid model. This coupling has been developed during the PhD of Maurin (2015) and validated with monodisperse particle-scale experiments (Frey, 2014) in Maurin et al. (2015). It was used to study bedload rheology (Maurin et al., 2016) and the slope influence (Maurin et al., 2018) in monodisperse configurations. It has been extended to bidisperse configurations in this PhD work. A summary of the model formulation is first presented for monodisperse beds. Then, the extension to bidisperse configurations is presented.

2.1.1 Granular phase

DEM is a Lagrangian method based on the resolution of contacts between particles. For each spherical particle p, the motion of the particle is obtained from Newton's second law, solving the translational and rotational momentum conservation equations

$$m^p \frac{d^2 \boldsymbol{x}^p}{dt^2} = \boldsymbol{f}_g^p + \boldsymbol{f}_c^p + \boldsymbol{f}_f^p, \tag{2.1}$$

$$\mathcal{I}^p \frac{d\boldsymbol{\omega}^p}{dt} = \boldsymbol{\mathcal{T}} = \boldsymbol{x}_c \times \boldsymbol{f}_c^p, \tag{2.2}$$

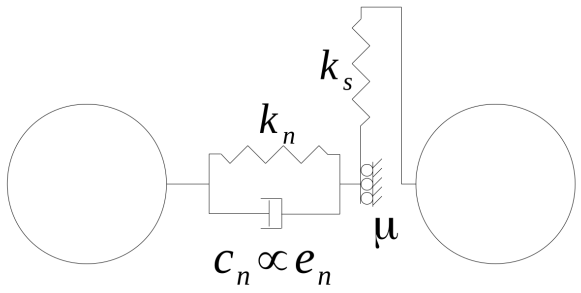

Figure 2.1: The spring-dashpot sytem modelling the inter-particles contact forces.

where m^p, $\boldsymbol{x}^p$, $\boldsymbol{\omega}^p$ and $\mathcal{I}^p$ are respectively the mass, position, angular velocity and moment of inertia of particle p. The three major forces are: $\boldsymbol{f}_g^p$ the gravitational force, $\boldsymbol{f}_c^p$ the inter-particle contact forces and $\boldsymbol{f}_f^p$ the interaction forces with the fluid. The inter-particle contact forces are schematically presented in figure 2.1. They are classically defined as a spring-dashpot system (Schwager and Poschel, 2007) composed of a spring of stiffness k_n in parallel with a viscous damper of coefficient c_n in the normal direction; and a spring of stiffness k_s associated with a slider of friction coefficient μ_p in the tangential direction. The normal and tangential contact forces read accordingly

$$\begin{aligned} F_n &= -k_n\delta_n - c_n\dot{\delta}_n, \\ F_t &= -\min(k_s\delta_t, \mu_p F_n), \end{aligned} \tag{2.3}$$

where δ_n (resp. δ_t) is the overlap between particles in the normal (resp. tangential) direction. For each class of particles, the values of k_n and k_s, taken equal, are computed in order to stay in the rigid limit of grains (Roux and Combe, 2002; Maurin et al., 2015) by imposing

$$\frac{k_n}{max(P^p)d^p} > 10^4, \tag{2.4}$$

where d^p denotes the diameter of particle p and $max(P^p)d^p$ is the maximal pressure that a grain can encounter. It is determined assuming a hydrostatic granular pressure. This ensures a weak enough interpenetration of particles so that the results are independent of the stiffness. The normal stiffness, in parallel with the viscous damper, defines a restitution coefficient representative of the loss of energy during collisions. Based on measurements in an experimental channel (Bigillon, 2001), it is fixed herein to $e_n = 0.5$ for each contact. Finally, considering glass beads, the friction coefficient is fixed to $\mu_p = 0.4$, corresponding to the friction coefficient of dry glass beads. Maurin (2015) performed a sensitivity analysis on e_n and μ^p and showed that results are negligibly affected by the value of these coefficients as long as they remain in realistic ranges $e_n \in [0.25, 0.75]$ and $\mu^p \in [0.2, 0.8]$.

The third type of forces concerns the interactions with the fluid. As the fluid flows with respect to particles, this induces several forces such as drag force, buoyancy force, Magnus force, shear induced lift force, added mass force or even Basset history force (Guyon et al., 2001; Guazzelli and Morris, 2011). With experimental measurements of the forces applied on a fixed particle over a rough bed and immersed in a free surface flow, Schmeeckle

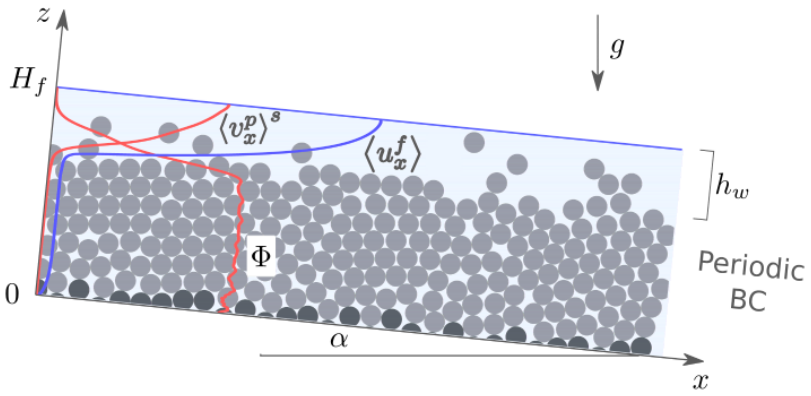

Figure 2.2: Adapted from Maurin (2015). Sketch of the problem with axes and variables used in the model: the free surface position H_f, the water depth h_w, the gravity vector $\vec{g}$, the averaged fluid and solid velocity profile $\langle u_x \rangle^f$ and $\langle v_x^p \rangle^s$ and volume fraction profiles Φ. Periodic boundary conditions (BC) are used in the streamwise and spanwise direction for the solid phase.

et al. (2007) showed that the main fluid forces acting on a particle in sediment transport are the lift force, the drag force and the buoyancy force. They showed that the classical formulation of the lift force proposed by Wiberg and Smith (1985) is not valid close to the threshold of motion and, based on the absence of an alternative formulation, Maurin et al. (2015) decided not to include the lift force in the model. The fluid interaction forces are therefore restricted in this model to the buoyancy force and the drag force. They are defined as

$$\boldsymbol{f}_b^p = -\frac{\pi d^{p3}}{6} \nabla P^f_{\boldsymbol{x}^p}, \tag{2.5}$$

$$\boldsymbol{f}_D^p = \frac{1}{2}\rho_f \frac{\pi d^{p2}}{4} C_D || \langle \boldsymbol{u} \rangle^f_{\boldsymbol{x}^p} - \boldsymbol{v}^p || \left(\langle \boldsymbol{u} \rangle^f_{\boldsymbol{x}^p} - \boldsymbol{v}^p \right), \tag{2.6}$$

where $\langle \boldsymbol{u} \rangle^f_{\boldsymbol{x}^p}$ is the mean fluid velocity at the position of particle p, $P^f_{\boldsymbol{x}^p}$ is the hydrostatic fluid pressure at the position of particle p and $\boldsymbol{v}^p$ is the velocity of particle p. The drag coefficient proposed by Dalla Valle (1943) with a hindrance effect correction (Richardson and Zaki, 1954) is considered

$$C_D = (0.4 + 24.4/Re_p)(1-\Phi)^{-\zeta}, \tag{2.7}$$

with $Re_p = || \langle \boldsymbol{u} \rangle^f_{\boldsymbol{x}^p} - \boldsymbol{v}^p || d^p / \nu^f$ the particle Reynolds number, ν^f the pure fluid viscosity and Φ the solid phase volume fraction. The $(1-\Phi)^{-\zeta}$ term takes into account hindrance effects due to the collective presence of particles and the exponent is fixed to $\zeta = 3.1$ (Jenkins and Hanes, 1998).

2.1.2 Fluid phase

In order to model the bedload configuration, the DEM is coupled with a fluid model. The problem is sketched in figure 2.2. Water flows around and above particles. In order to gain computational time, and because the aim of the model is to focus on the granular processes, it has been decided to use a horizontal averaged fluid model. It is based on the three-dimensional (3D) spatially averaged two-phase momentum equations of Jackson (2000), modelling the average motion of both the fluid and granular phases. Based on an averaging procedure that is described below, Jackson (2000) showed that the momentum equations of the granular and fluid phases are

$$\rho^p \Phi \left(\frac{\partial \left\langle v_i^p \right\rangle^s}{\partial t} + \left\langle v_i^p \right\rangle^s \frac{\partial \left\langle v_i^p \right\rangle^s}{\partial x_j} \right) = \rho^p \Phi g_i + \frac{\partial \sigma_{ij}^p}{\partial x_j} + n \left\langle f_{f_i}^p \right\rangle^s , \tag{2.8}$$

$$\begin{aligned} \rho_f (1-\Phi) \left(\frac{\partial \left\langle u_i \right\rangle^f}{\partial t} + \left\langle u_i \right\rangle^f \frac{\partial \left\langle u_i \right\rangle^f}{\partial x_j} \right) = & - \frac{\partial \left((1-\Phi) P^f \right)}{\partial x_i} + \frac{\partial S_{ij}}{\partial x_j} + \frac{\partial R_{ij}}{\partial x_j} \\ & + \rho_f (1-\Phi) g_i - n \left\langle f_{f_i}^p \right\rangle^s , \end{aligned} \tag{2.9}$$

where $\langle . \rangle^s$ (resp. $\langle . \rangle^f$) denotes for the solid phase average (resp. the fluid phase average), ρ_f is the density of the fluid, $\langle v_i^p \rangle^s$ (resp. $\langle u_i \rangle^f$) is the i^{th} component of the averaged particle velocity (resp. averaged fluid velocity). σ_{ij}^p, S_{ij} and R_{ij} are the ij components of respectively the granular stress, the fluid effective viscous shear stress and the Reynolds shear stress. Finaly $n \left\langle f_{f_i}^p \right\rangle^s$ represents the i^{th} component of momentum transfer associated with the interaction forces between fluid and particles.

In the present model, the granular phase is solved with the DEM. Only the fluid phase is solved as a continuum phase with equation 2.9. At transport steady state, the total granular phase (of small and large particles) has only a streamwise component with no main transversal or vertical motion. In such a case, it can be shown (Revil-Baudard and Chauchat, 2013; Chauchat, 2018) that the 3D volume-averaged equation on the fluid velocity reduces to a one-dimensional (1D) vertical equation, in which the fluid velocity is only a function of the wall-normal component, z, and is aligned with the streamwise direction (see figure 2.2). The projection along z of the fluid momentum equation provides that the fluid pressure P^f is in this case given by the hydrostatic fluid pressure. The fluid model is therefore a one-dimensional turbulent model in the streamwise x-direction with variables only depending on z. The projection along x of the volume-averaged momentum balance for the fluid phase (equation 2.9) simplifies to

$$\rho_f (1-\Phi) \frac{\partial \left\langle u_x \right\rangle^f}{\partial t} = \frac{\partial S_{xz}}{\partial z} + \frac{\partial R_{xz}}{\partial z} + \rho_f (1-\Phi) g_x - n \left\langle f_{f_x}^p \right\rangle^s , \tag{2.10}$$

This equation is close to a classical 1D turbulent fluid equation but accounts for the presence of particles via the solid volume fraction Φ and the momentum transfer term. In addition, the choice of closures for the viscous shear stress and turbulent shear stress is also done according to the presence of particles.

The fluid (water) being considered Newtonian, the viscous shear stress S_{xz} is classicaly taken as

$$S_{xz} = \rho_f(1-\Phi)\nu^e \frac{\partial \langle u_x \rangle^f}{\partial z}, \tag{2.11}$$

with ν^e the Einstein's effective viscosity defined as (Einstein, 1906) $\nu^e = \nu^f(1+5/2\Phi)$. Jackson (1997) demonstrated analytically that this modification of viscosity originates from second order particle fluid phase interactions.

The Reynolds shear stress R_{xz} is a turbulent fluid stress induced by fluid velocity fluctuations. This stress has to be modelled and a closure based on an eddy viscosity concept is adopted,

$$R_{xz} = \rho_f(1-\Phi)\nu_t \frac{\partial \langle u_x \rangle^f}{\partial z}. \tag{2.12}$$

The turbulent viscosity ν_t follows a mixing length approach that depends on the integral of the solid volume fraction profile to account for the presence of particles (Li and Sawamoto, 1995),

$$\nu_t = l_m^2 \left| \frac{\partial \langle u_x \rangle^f}{\partial z} \right|, \quad l_m(z) = \kappa \int_0^z \frac{\Phi_{max} - \Phi(\zeta)}{\Phi_{max}} d\zeta, \tag{2.13}$$

with $\kappa = 0.41$ the Von-Karman constant and $\Phi_{max} = 0.61$ the maximal packing of the granular medium (random close packing). This simple formulation of mixing length extends the Prandtl (1926) law for flow inside and over a mobile sediment bed. In the pure fluid phase above the sediment bed $\Phi = 0$ and the linear mixing length of Prandtl (1926) is recovered. Inside the bed, where $\Phi = \Phi_{max}$, the mixing length goes to zero, and the turbulence is damped inside the dense sediment bed.

The total momentum $n\left\langle f_{f_x}^p \right\rangle^s$ transmitted by the fluid to the particles corresponds to the average momentum transfer associated to the drag force. As the solid phase is solved with the DEM, a drag force is applied on each particle individually. It is therefore necessary to compute the horizontal solid-phase average (denoted $\langle . \rangle^s$) of the momentum transmitted by the drag force to each particle:

$$n\left\langle f_{f_x}^p \right\rangle^s = \frac{\Phi}{\pi d^{p3}/6} \left\langle f_{f_x}^p \right\rangle^s, \tag{2.14}$$

and introducing the expression of the drag force (2.6),

$$n\left\langle f_{f_x}^p \right\rangle^s = \frac{3}{4}\frac{\Phi\rho_f}{d^p} \left\langle C_D || \langle \boldsymbol{u} \rangle_{\boldsymbol{x}^p}^f - \boldsymbol{v}^p || \left(\langle \boldsymbol{u} \rangle_{\boldsymbol{x}^p}^f - \boldsymbol{v}^p \right) \right\rangle^s, \tag{2.15}$$

This expression requires the definition of the solid phase average $\langle . \rangle^s$, which is presented in the next sub-section.

The fluid model, which is classical in sediment transport (Drake and Calantoni, 2001; Hsu and Liu, 2004; Durán et al., 2012; Revil-Baudard and Chauchat, 2013; Maurin et al., 2015; Chauchat, 2018), is only closed using a mixing length model and a closure for the drag force formulation. These closures are usual in the literature, and it has been shown in Maurin (2015) and Maurin et al. (2015) that the results obtained in terms of granular behavior are very weakly sensitive to the fluid closure adopted.

2.1.3 Averaging procedure

In the framework of the volume average two-phase equations, Jackson (1997, 2000) proposed an averaging procedure based on a weighting function, representing the volume in which the average is performed. Considering the symmetry of the current problem and remembering that the variables have no dependencies in the horizontal x and y directions, a cuboid weighting function $\mathcal{H}$ with the same length and width as the 3D domain is applied. In the vertical direction, in order to capture the strong vertical gradient of the mean flow, the vertical thickness l_z of the box is chosen as $l_z = d^p/30$, giving the following weighting function

$$\mathcal{H}(\boldsymbol{x}) = \begin{cases} \dfrac{1}{V} = \dfrac{1}{LBl_z}, & \text{if } z \in [-l_z/2, l_z/2], \\ 0, & \text{otherwise}, \end{cases} \tag{2.16}$$

where L and B denote respectively for the length and breadth of the domain. The volume fraction is computed as

$$\Phi(z) = \sum_p \int_{V_p} \mathcal{H}(|z - z'|)dz', \tag{2.17}$$

where $\int_{V_p}$ represents the integral over the volume of particle p. The average over the solid phase of any scalar quantity γ is computed as

$$\langle\gamma\rangle^s = \frac{1}{\Phi(z)} \sum_p \int_{V_p} \gamma(z')\mathcal{H}(|z - z'|)dz', \tag{2.18}$$

This averaging procedure makes it possible to compute the total transfer of momentum between the fluid and particles.

The fluid model should *a priori* be valid only if there is scale separation between the macroscopic length (the flow height H_f in our case), the weighting function length scale l_z, and the particle diameter d^p, i.e. $H_f >> l_z >> d^p$ (Jackson, 1997). This is however not the case as l_z has been choosen such that $l_z = d^p/30$ in order to capture the very sharp transition at the sediment bed interface. This may introduce uncertainties when computing the fluid particle transfer of momentum and fluid stresses. However, Maurin et al. (2015) showed, by comparison with monodisperse turbulent bedload transport experiments, that the uncertainties on the computed averaged quantities are small, provided that the size of the domain $L \times B$ is sufficiently large, typically $L \times B \geq 20d^p \times 20d^p$.

The averaging procedure is also used to obtain granular continuum fields when post processing the data, in particular to obtain the granular velocity field. This averaging procedure is also known as coarse-graining and Weinhart et al. (2013) showed that such spatial averaging method is necessary to obtain macroscopic fields consistent with conservation laws of continuum theory.

2.1.4 Granular stresses

For a box with scale separation, it is possible to forget the discrete nature of the granular bed and to consider it as a continuum phase. Goldhirsch (2010) proposed a rigourous averaging procedure to compute the stresses of a granular medium. The author showed

that the granular stresses at position $\boldsymbol{x}$ and time t are the sum of a kinematic and a contact force contribution as

$$\sigma_{ij}^{p}(\boldsymbol{x},t) = \sigma_{ij}^{k}(\boldsymbol{x},t) + \sigma_{ij}^{c}(\boldsymbol{x},t). \tag{2.19}$$

The computation of both contributions depends on the choice of a weighting averaging function. For the same cuboid weighting function $\mathcal{H}$ as defined previously, it can be shown (Andreotti et al., 2013; Maurin et al., 2015) that the stress formulation (2.19) simplifies to

$$\sigma_{ij}^{p}(z) = -\frac{1}{V}\sum_{p\in V(z)} m^{p} v_{i}^{\prime p} v_{j}^{\prime p} - \frac{1}{V}\sum_{c\in V(z)} f_{i}^{c} b_{j}^{c}, \tag{2.20}$$

where the sums are performed over the ensemble of particles p and contacts c inside the volume $V(z)$ such that $z \in [z - l_z/2, z + l_z/2]$, $v_k^{\prime p} = v_k^p - \langle v_k^p \rangle^s$ is the k^{th} component of the spatial velocity fluctuation of particle p, $\boldsymbol{f}^c$ is the interaction force at contact c applied on particle α by particle β and $\boldsymbol{b}^c = \boldsymbol{x}^\beta - \boldsymbol{x}^\alpha$ is the branch vector. The first term corresponds to the kinetic contribution and, similarly to the Reynolds stress tensor for the fluid phase, it is induced by the particle velocity fluctuations during the flow. The second term, also known as the Lowe-Weber stress tensor in the geomechanics community, corresponds to the contact forces induced stress. As the discretization step l_z has been chosen very small, the branch vector can cross several vertical cells. In this case, the contact force is distributed proportionally to the part of the branch vector contained in the cell. Maurin (2015) showed that the stress value was not sensitive to the discretization l_z, indicating the relevency of this method. Due to the one dimensional structure of the flow, Maurin (2015); Maurin et al. (2016) showed that, in the steady state bedload configuration, $\sigma_{zz}^p = Tr(\sigma^p)/3 = P^p$ and the only non diagonal terms which are not vanishing are σ_{xz}^p and σ_{zx}^p, with $\sigma_{xz}^p = \sigma_{zx}^p$. The granular stress tensor can therefore be expressed classically as the sum of a pressure term and a shear stress term

$$\sigma_{ij}^{p}(z) = -P^{p}\delta_{ij} + \tau_{ij}^{p}, \tag{2.21}$$

where $\tau_{xz}^p = \sigma_{xz}^p$ is the only non-negligible shear stress term.

2.1.5 Extension to bidisperse configurations

For this PhD work, the coupled fluid-DEM model has been extended to bidisperse configurations. For the DEM part of the model, the extension is almost direct. We denote d_s (resp. d_l) the diameter of small (resp. large) particles. The only modifications lie on the computation of the stiffnesses k_n and k_s adapting the rigid limit condition (eq. 2.4) according to the size of particles. The particle diameter also appears in the expression of the buoyancy force (eq. 2.5) and the drag force (eq. 2.6). The fluid interaction forces are therefore computed according to the particle size.

Concerning the fluid phase, the main modification when considering bidisperse mixtures lies in the momentum transfer by the fluid to particles $n\left\langle f_{f_x}^p \right\rangle^s$, in which the solid-phase average operator need to be extended to bidisperse cases. The same cuboid weighting

function $\mathcal{H}$ as in equation (2.16) is used, with the vertical thickness $l_z = d_s/30$ computed on the small particle diameter. The volume fraction of each class is computed as

$$\Phi_s(z) = \sum_{p_s} \int_{V_{ps}} \mathcal{H}(|z - z'|)dz', \tag{2.22}$$

$$\Phi_l(z) = \sum_{p_l} \int_{V_{pl}} \mathcal{H}(|z - z'|)dz', \tag{2.23}$$

where p_s (resp. p_l) denotes the ensemble of the small (resp. large) particles, Φ_s (resp. Φ_l) the volume fraction of small (resp. large) particles. The total volume fraction is $\Phi = \Phi_s + \Phi_l$. The average over the small particle phase of any scalar quantity γ is computed as

$$\langle\gamma\rangle^{small} = \frac{1}{\Phi_s(z)} \sum_{p_s} \int_{V_{ps}} \gamma(z')\mathcal{H}(|z - z'|)dz'. \tag{2.24}$$

Similarly, the average over the large particle phase is

$$\langle\gamma\rangle^{large} = \frac{1}{\Phi_l(z)} \sum_{p_l} \int_{V_{pl}} \gamma(z')\mathcal{H}(|z - z'|)dz'. \tag{2.25}$$

The total solid phase average is therefore computed as the sum over each class of the solid phase average as

$$\langle\gamma\rangle^{s} = \langle\gamma\rangle^{small} + \langle\gamma\rangle^{large}. \tag{2.26}$$

This averaging procedure allows the computation of average values for each class and for the mixture. Finally the transfer of momentum from the fluid to the particle phase is computed as

$$n \left\langle f_{f_x}^{p} \right\rangle^{s} = \frac{\Phi_s}{\pi d_s^3/6} \left\langle f_{f_x}^{p_s} \right\rangle^{s} + \frac{\Phi_l}{\pi d_l^3/6} \left\langle f_{f_x}^{p_l} \right\rangle^{s}, \tag{2.27}$$

and introducing the expression of the drag force (2.6),

$$\begin{aligned} n \left\langle f_{f_x}^{p} \right\rangle^{s} = \frac{3}{4}\frac{\Phi_s \rho_f}{d_s} \left\langle C_D || \langle \boldsymbol{u} \rangle_{\boldsymbol{x}^{p_s}}^{f} - \boldsymbol{v}^{p_s} || \left(\langle \boldsymbol{u} \rangle_{\boldsymbol{x}^{p_s}}^{f} - \boldsymbol{v}^{p_s} \right) \right\rangle^{s} \\ + \frac{3}{4}\frac{\Phi_l \rho_f}{d_l} \left\langle C_D || \langle \boldsymbol{u} \rangle_{\boldsymbol{x}^{p_l}}^{f} - \boldsymbol{v}^{p_l} || \left(\langle \boldsymbol{u} \rangle_{\boldsymbol{x}^{p_l}}^{f} - \boldsymbol{v}^{p_l} \right) \right\rangle^{s}. \end{aligned} \tag{2.28}$$

This extends the coupled fluid-DEM model to bidisperse configurations, and it can now be used to study size-segregation.

2.2 The bedload configuration: presentation and continuum description

Before using this model in bidisperse situations, the setup and main characteristics of the bedload configuration are presented here in the case of a monodisperse simulation. Indeed, the literature review performed in the introduction has shown that the segregation dynamics is a response to the granular state of the bed. A clear description of the bedload configuration is therefore necessary.

2.2.1 Numerical setup

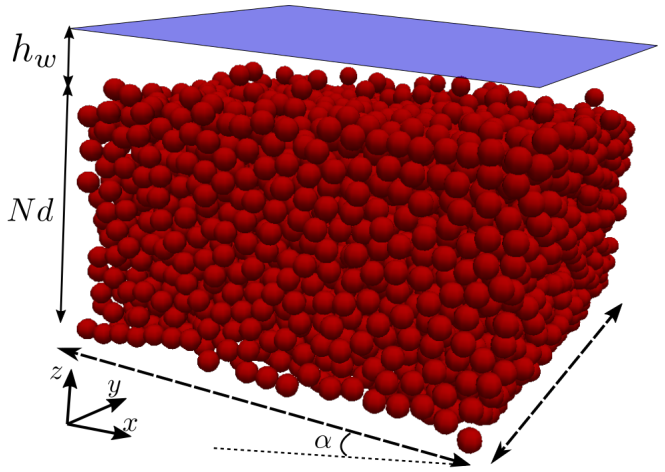

Figure 2.3: Numerical setup. N layers of particles are deposited by gravity above a rough bed made of fixed particles. The fluid free surface elevation is set to $H_f = Nd + h_w$, where h_w represents the water depth. Due to the slope α the fluid flows by gravity and entrains particles.

The numerical setup is presented in figure 2.3. It is composed of a 3D domain, biperiodic in both streamwise x and spanwise y directions. Particles of diameter $d = 6$ mm and density $\rho^p = 2500$ kg.m^{-3} are considered, corresponding to typical glass beads used at the INRAE laboratory. They are deposited by gravity above a rough layer made of fixed particles randomly positioned between $-d/2$ and $d/2$. The number of particles is associated to a number of layers N. The number of layers corresponds, in term of particle diameter, to the height occupied by particles if the volume fraction is exactly the observed random close packing $\Phi = 0.61$. This defines the height of the bed $H = (1/2 + N)d$, where the $1/2$ accounts for the fixed particles at the bottom. The particles are immersed in a fluid, here water, of density $\rho^f = 1000$ kg.m^{-3}. The free surface is fixed to $H_f = Hd + h_w$, where h_w represents the water depth. In this study the slope is fixed to 10% (5.7°) to mimick steep slope bedload transport, occuring in mountain streams. At initial time, the fluid flows by gravity and sets particles into motion. After a rapid transient phase, during which fluid and particles are accelerating, a steady state takes place at transport equilibrium.

The bedload configuration will be illustrated with a simulation of $N = 10$ layers of 6 mm diameter particles and with a water depth of $h_w = 4.7d$. The value of N has been chosen high enough in order to ensure an erodible bed bottom boundary condition. Each quantity is computed using the spatial averaging procedure (2.18) and are obtained every $\Delta t = 0.1$s. The simulation lasts 300s and the profiles presented thereafter are obtained by averaging all profiles once steady state is achieved, i.e. after about 20s.

2.2.2 Description of the bedload configuration

In the bedload configuration, different flow regimes take place at the same time, which are described in this section. An hydrodynamic vision is adopted for the granular phase, which is seen as a continuum material. Figure 2.4 shows the depth profiles of the volume fraction, the fluid velocity, the particle velocity and the transport rate, the latter being the product of the volume fraction with particle velocity. In all figures in this PhD manuscript, the fluid mechanics convention is adopted, with depth on the vertical axis and quantities of interest on x-axis. The figures exhibit three different regions. Below $z \sim 6d$, the volume fraction is almost constant around the random close packing $\Phi \sim 0.61$. This zone corresponds to the quasi-static region, or creeping region, where the particle and fluid velocity profiles are exponentially decreasing into the bed (see inset in semilog scale of figure 2.4c). The particle velocity is very low in this zone and the quasi-static region has a negligible contribution to the overall sediment transport rate. Above $z \sim 6d$, the volume fraction decreases almost linearly to zero. This region will be called flowing layer, or bedload layer, corresponding to a transition zone between the quasi-static region to a pure fluid phase. Its thickness has been shown to be proportional to the Shields number (Bagnold, 1956; Capart and Fraccarollo, 2011) and most of the sediment transport is taking place in this layer (see figure 2.4d). The velocity of both the fluid and the particles is strongly increasing with elevation. Note that the total height of the bed is slightly larger than H due to dilatation of the bed (reduction of the volume fraction). In the bedload layer, the three granular classical flow regimes coexist (Andreotti et al., 2013) with a continuous transition from a quasi-static flow regime at the lower boundary of the bedload layer to a dense regime and then a dilute regime at the top boundary. The pure fluid phase takes place above $z \sim 13.5d$, where $\Phi = 0$, until the free surface at $z = 15.2d$ in this simulation. Note that data for the particle velocity can be collected even in the pure fluid phase because of very rare events of saltating particles reaching this region.

This complex phenomenology, with continuous transitions between the three different granular flow regimes, makes the bedload configuration very rich when studying granular mechanisms. This PhD work will mainly focus on the quasi static and dense flow regimes.

2.2.3 Granular rheology in bedload transport

A key issue for granular flows is to be able to relate the granular stress state to the kinetic state. This is called rheology. Monodisperse dense dry granular flows are well described by the $\mu(I)$ rheology (GDR MiDi, 2004; Jop et al., 2006; Forterre and Pouliquen, 2008). Assuming a local rheology, i.e. that the granular stresses only depend on the local shear

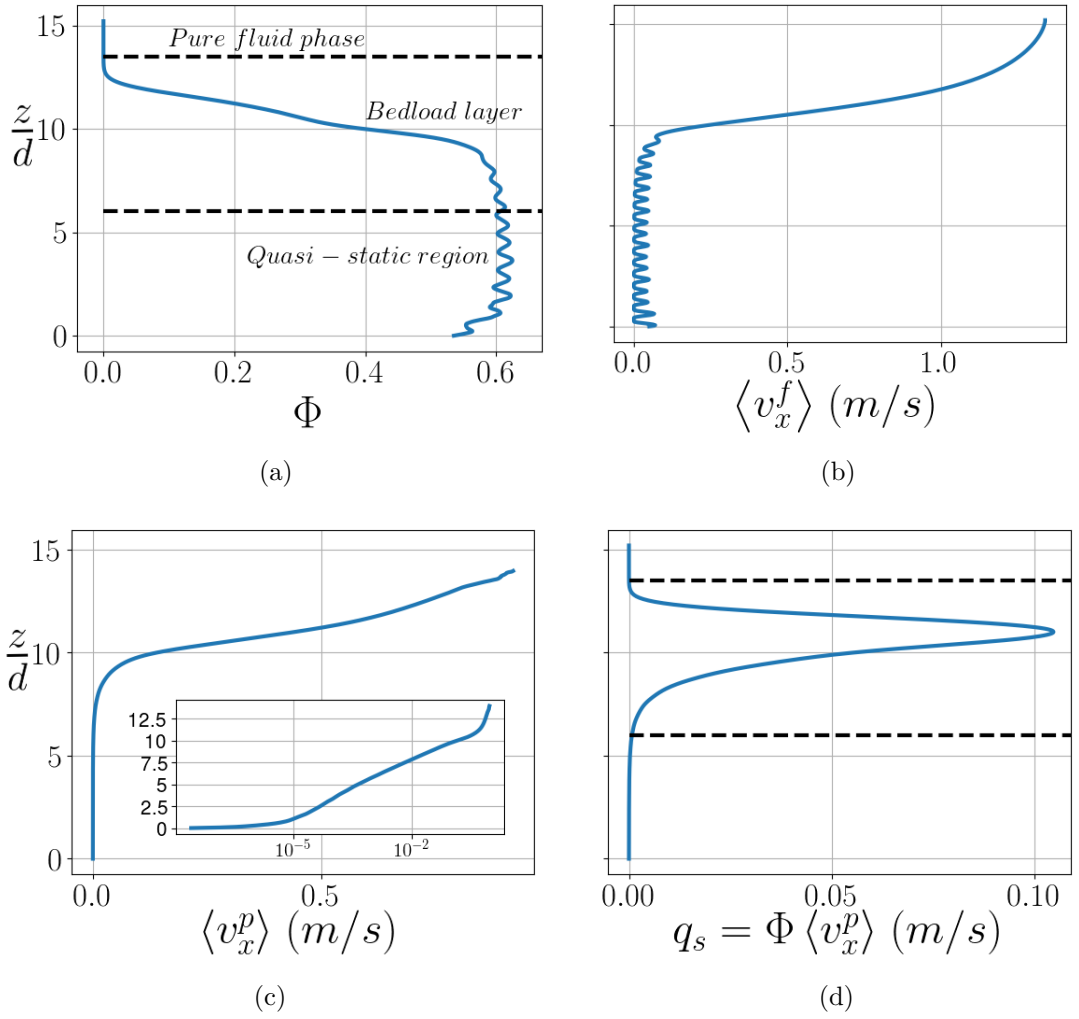

Figure 2.4: DEM simulation with $N = 10$ layers of particles and water depth $h_w = 4.7d$. (a) Volume fraction profile, (b) fluid velocity profile, (c) particle velocity with inset in semilog plot, (d) transport rate profile. Dashed lines separate the different region of transport.

rate and pressure, a dimensional analysis indicates that the dry inertial number I is the only dimensionless parameter controlling the system, where

$$I = \frac{d\dot{\gamma}^p}{\sqrt{P^p/\rho^p}}. \tag{2.29}$$

The shear to normal stress ratio $\mu = \tau_{xz}^p/P^p$ and the volume fraction Φ therefore only depend on the inertial number. Fitting DEM simulations and experiments, the following phenomenological expressions have been obtained (Jop et al., 2005; da Cruz et al., 2005; Pouliquen et al., 2006)

$$\mu(I) = \mu_c + \frac{\mu_2 - \mu_c}{I_0/I + 1}, \tag{2.30}$$

$$\Phi(I) = \Phi_{max} - bI, \tag{2.31}$$

with $\mu_c = 0.38$, $\mu_2 = 0.64$, $I_0 = 0.279$ and $b = 0.31$ are empirical data. This constitutive law models the granular media as a viscoplatic material. μ_c represents the static friction coefficient below which no motion is *a priori* possible. Creeping flow is possible below the threshold μ_c but the flow is controlled by non local effects that the $\mu(I)$ rheology is not able to capture.

To account for the presence of an interstitial fluid, one should replace in the constitutive laws (2.30) and (2.31) the dry inertial number by the viscous inertial number $I_{visc} = \eta^f\dot{\gamma}^p/P^p$ or the turbulent inertial number $I_{turb} = d\dot{\gamma}^p/\sqrt{P^p/(\rho^f C_D)}$ (Cassar et al., 2005) depending on the interstitial fluid influence regime (Courrech du Pont et al., 2003).

With the coupled fluid DEM model, Maurin et al. (2016) studied the granular rheology of monodisperse beds in bedload transport. In the dense part of the flow, despite the presence of water, the authors showed that the dry inertial number is still the controlling parameter. They found the $\mu(I)$ rheology to be valid in bedload transport in a wider range of inertial numbers than the dry classical $\mu(I)$ rheology and proposed another set of parameters $\mu_c = 0.35$, $\mu_2 = 0.97$ and $I_0 = 0.69$. They also proposed a slightly different law for the volume fraction as $\Phi(I) = \Phi_{max}/(1 + aI)$, with $a = 0.31$.

2.2.4 Momentum balance

The averaging procedure presented in section 2.1.4 allows the computation of granular stresses and therefore to adopt a continuum vision of the granular flow. In the dense and quasi-static part of the bed, it is interesting to understand the stress repartition between the fluid and the granular phase. This is made possible by writing the momentum balance of both phases. Starting from the 3D average two-phase flow equations of Jackson (1997, 2000) (equations (2.8) and (2.9)), Revil-Baudard and Chauchat (2013) and Chauchat (2018) showed that, for a unidirectional and steady state flow conditions, they simplifies as

$$0 = \frac{\partial S_{xz}}{\partial z} + \frac{\partial R_{xz}}{\partial z} + \rho_f(1-\Phi)g\sin(\alpha) - n\left\langle f_{f_x}^p \right\rangle^s, \tag{2.32}$$

$$0 = \frac{\partial \tau_{xz}^p}{\partial z} + \rho^p \Phi g \sin\alpha + n \left\langle f_{f_x}^p \right\rangle^s, \tag{2.33}$$

$$0 = \frac{\partial P^f}{\partial z} + \rho^f g \cos\alpha, \tag{2.34}$$

$$0 = \frac{\partial P^p}{\partial z} + (\rho^p - \rho^f)\Phi g \cos\alpha, \tag{2.35}$$

These equations are expected to model the stress balance of both phases at transport steady state. They bring information on the origin of stresses and, under some simplifications, allow the derivation of analytical expressions of the granular stresses. These analytical expressions, derived thereafter, will be used several times in the PhD manuscript.

By integration of equations (2.34) and (2.35) between an altitude z and the free surface position H_f where $P^f(H_f) = P^p(H_f) = 0$, the two phase flow model predicts hydrostatic pressure for both the fluid and granular phases

$$P^f(z) = -\rho^f g \cos\alpha (H_f - z), \tag{2.36}$$

$$P^p(z) = -(\rho^p - \rho^f) g \cos\alpha \int_z^{H_f} \Phi(\xi)\, \mathrm{d}\xi. \tag{2.37}$$

Summing equation (2.32) and (2.33), a mixture momentum balance is obtained

$$0 = \frac{\partial S_{xz}}{\partial z} + \frac{\partial R_{xz}}{\partial z} + \frac{\partial \tau_{xz}^p}{\partial z} + \left(\rho^f + (\rho^p - \rho^f)\Phi\right) g \sin(\alpha). \tag{2.38}$$

Maurin et al. (2016) showed that the viscous fluid shear stress S_{xz} is negligible in the turbulent bedload configuration and it will therefore not be taken into account in this study. In order to understand the repartition between the fluid and the granular stresses, equation (2.38) is integrated between an altitude z and H_f, where both shear stresses are assumed to vanish, leading to

$$R_{xz}(z) + \tau_{xz}^p(z) = \left(\rho^f (H_f - z) + (\rho^p - \rho^f) \int_z^{H_f} \Phi(\xi)\, \mathrm{d}\xi\right) g \sin(\alpha). \tag{2.39}$$

Figure 2.5a shows the granular pressure P^p and comparison with equation (2.37). Both curves collapse showing that the granular pressure is indeed hydrostatic. Except in the transition layer between pure fluid phase and dense flow, the granular pressure is linear with depth, indicating that the small variations of Φ below the transition zone (below $z \sim 6d$ in figure 2.4a) has a weak influence on the granular pressure profile.

The fluid shear stress can be computed from equations (2.12) and the granular shear stress from equation (2.20) by computing contact forces and velocity fluctuations in the DEM simulation. Figure 2.5b shows the Reynolds fluid stress together with the granular shear stress τ_{xz}^p. The two phase flow model only indicates that the fluid and the granular

shear stresses share a momentum source due to gravity (right hand side of equation (2.39)). It is plotted in dashed line in figure 2.5b and it shows that the two phase flow model and the DEM simulation are in perfect agreement. In the pure fluid phase ($\Phi = 0$), all the mixture shear stress is taken by the Reynolds shear stress and equation (2.39) simplifies to

$$R_{xz}(z) = \rho^f g \sin(\alpha)(H_f - z), \tag{2.40}$$

the classical expression of the turbulent fluid shear stress in free surface flows. In the granular bed the fluid shear stress rapidly decreases to zero and only the granular shear stress holds the momentum source.

To compute the granular shear stress with equation (2.39), the expression of the volume fraction profile Φ is needed. However it is not easy to obtain as it results from an equilibrium between the fluid and granular phase interactions. It can only be estimated with the coupled fluid-DEM model presented previously or by solving the Jackson (2000) equations and assuming a rheology to model the behavior of the granular phase. In order to obtain an analytical expression of the granular shear stress, it is however possible to assume a simplified volume fraction profile as a step function from $\phi_{max} = 0.61$ to 0 in H. This idealized volume fraction is plotted in figure 2.5c. This profile contains the same granular mass than the DEM one but assumes that the granular phase is transported without dilatation of the bed. It corresponds to an idealized situation, where the transition from the pure fluid phase to the dense sediment bed is discontinuous. For $z \leq H$, turbulence is assumed to be completely damped to zero, i.e. $R_{xz}(z) = 0$, and considering the step concentration profile, equation (2.39) simplifies to

$$\tau^p_{xz}(z) = \left[\rho^f (H_f - z) + (\rho^p - \rho^f)\Phi_{max}(H - z)\right] g \sin(\alpha), \tag{2.41}$$

and by definition of the water surface height $H_f - z = (H_f - H) + (H - z) = h_w + (H - z)$, it comes

$$\tau^p_{xz}(z) = \rho^f g \sin(\alpha) h_w + \left[\rho^p \Phi_{max} + (1 - \Phi_{max})\rho^f\right] g sin(\alpha)(H - z). \tag{2.42}$$

The first term of the right hand side is the fluid bed shear stress τ_b appearing in the classical definition of the Shields number and represents the stress transmission by the flowing fluid to the grains. The second term represents the variation of the shear stress with depth. The same simplified step concentration profile can be applied to equation (2.37) yielding

$$P^p(z) = -(\rho^p - \rho^f)\Phi_{max} g \cos\alpha (H - z). \tag{2.43}$$

Equations (2.42) and (2.43) are plotted in figure 2.5d with DEM data. It shows that, except in the transition toward the pure fluid phase, the DEM stress profiles are very well predicted by the two phase flow conditions. The simplified stress profiles may seem restrictive, as they do not reproduce the transition from the pure fluid phase to the dense granular flow, but it allows one to express both the granular pressure and shear stress only as a function of geometrical and physical parameters of the flow.

In fact this step volume fraction profile corresponds to an idealized situation where the fluid shear stress is completely transmitted to the granular bed at the discontinuity

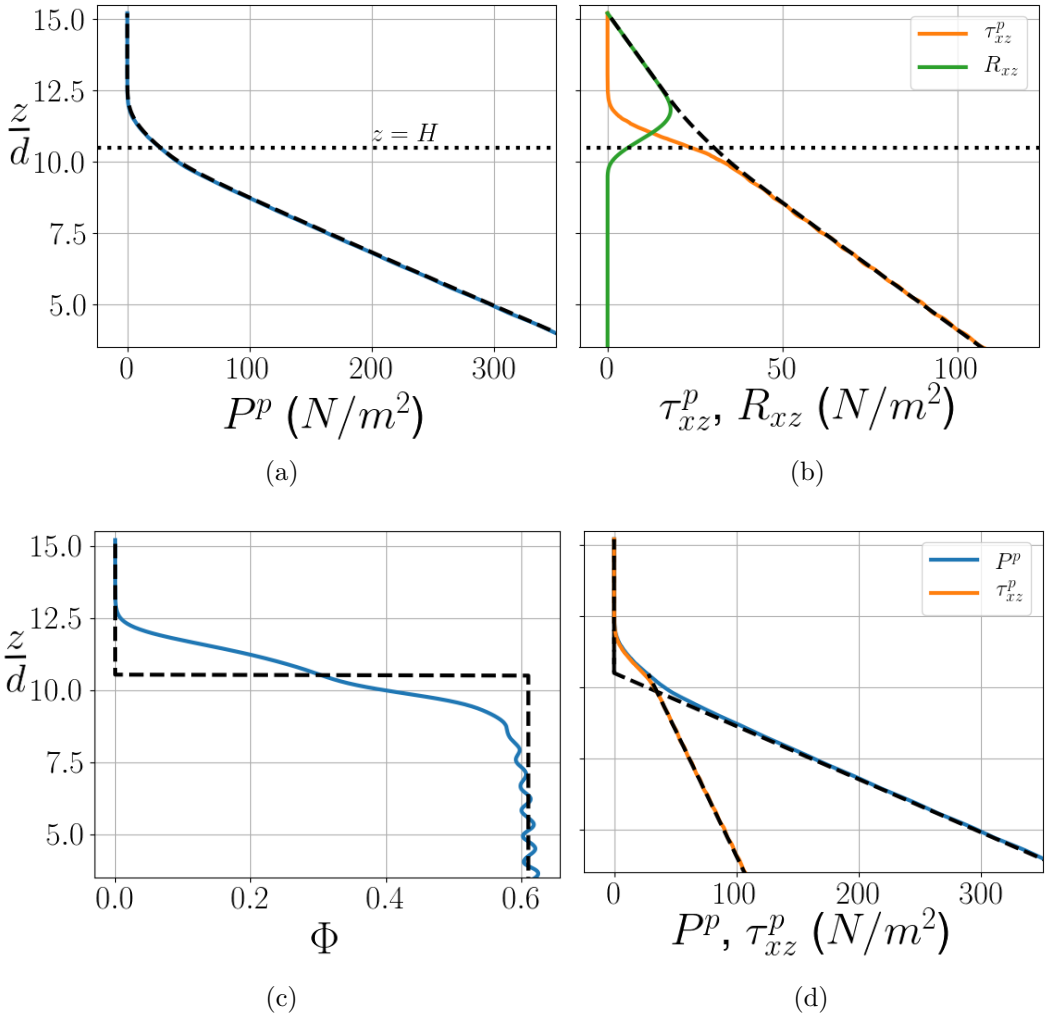

Figure 2.5: (a) Granular pressure from DEM simulation (full line) compared with equation (2.37) (dashed line). The dotted line indicates the geometrical bed position. (b) Granular shear stress (orange line) and Reynolds shear stress (green line) from DEM simulation and gravity term (dashed line) computed from equation (2.39). The dotted line indicates the geometrical bed position. (c) Idealized volume fraction profile (dashed line) compared with the DEM one (blue line) and (d) granular pressure (blue line) and granular shear stress (orange line) from DEM simulation compared with the predicted stress by equations (2.43) and (2.42).

($z = H$). Focusing on the granular shear stress, the DEM and analytical profiles correspond almost perfectly as soon as $z \leq H$. This indicates that in the DEM simulation the fluid stress is almost completely transmitted to the granular bed below $z \leq H$ and that the fluid does not provide any forcing and has a passive role inside the sediment bed. In figure 2.5b, it can be observed that the fluid stress decreases very rapidly between the line $z = H = 10.5d$ and $z = 10d$. This indicates that the fluid shear stress is completely damped in less than one diameter below the geometrical definition of the bed surface $z = H$. Ouriemi et al. (2009) obtained the same results with another two-phase continuum model. Below $z = H$, it will therefore be assumed that equations (2.42) and (2.43) model perfectly the granular stresses and that the fluid shear stress is negligible.

2.2.5 Discussion on the Shields number definition

The Shields number θ is defined as the dimensionless fluid bed shear stress. By analogy to a free surface flow on a fixed bed, the fluid bed shear stress is classicaly taken as $\tau_b = \rho^f g \sin(\alpha) h_w$, where h_w is the water depth. The volume fraction profile presented in figure 2.4a shows that there is no clear separation between the pure fluid phase and the granular bed and it is therfore difficult to measure a water depth. It is only possible to define a geometrical water depth, corresponding to a virtual depth where all particles are deposited and fully compacted at $\Phi = 0.61$. Since water depth is difficult to measure, Revil-Baudard and Chauchat (2013) and Maurin et al. (2015) proposed to define a Shields number based on the Reynolds stress profile (see figure 2.5b) such that $\tau_b = \max(R_{xz})$. Two definitions of the Shields number are then considered. The first definition, based on h_w, will be referred to as the macroscopic Shields number and the second one, based on the maximum Reynolds Stress, as the microscopic Shields number. The latter gives values of the Shields number smaller than the macroscopic one, i.e. for this configuration $\theta = 0.2$ for the microscopic Shields number and $\theta = 0.3$ for the macroscopic one. Indeed, due to interactions with particles, a negative feedback applies on the fluid and the Reynolds shear stress is rapidly damped to zero in the flowing layer (see figure 2.5b). This microscopic Shields number should therefore be the relevant parameter when studying phenomena in the bedload layer. However the fluid bed shear stress based on the geometrical water depth appears in the expression of the granular shear stress (see equation (2.42)). Therefore the macroscopic Shields number is as more relevant as the microscopic number when studying phenomena below the bed surface.

In practice, the microscopic definition of the Shields number is difficult to use. This definition indeed implies to be able to measure the Reynold stress profile which is far from being easy. It is experimentally possible to measure the fluid velocity fluctuations and to deduce a Reynold stress profile. In the field, with current techniques, measuring the Reynold stress is extremely difficult. The macroscopic definition based on the water depth is therefore more classical. Defining the water depth is also a subject of discussion. To measure a water depth, the bed position should be defined, which is not obvious as the transition layer between the dense bed and the pure fluid phase may reach several particle diameters. But this is more a question of definition (where is the bed position ?) than a technical difficulty.

This discussion about both definitions of the Shields number is essentially relevent for small water depths of the order of the particle diameter on steep slopes. Indeed, when the water depth is large in comparison to the particle diameter, both definitions are very close and it is therefore more convenient to use the macroscopic definition. For large water depths, the width of the transition layer becomes negligible and there is no problem of definition for the water depth.

Chapter 3

Segregation mechanisms analysis and continuum modelling in the quasi-static regime

This chapter is dedicated to the description, analysis and modelling of size segregation during bedload transport in the quasi-static regime. As pointed out in the introduction, size segregation is still not yet well understood, in particular in configurations with complex forcing such as bedload transport. It will be analysed using the coupled fluid DEM model (chapter 2) in the framework of the dimensional analysis (aq. 1.7) presented in the introduction (section 1.2). The aim is to understand size segregation in the quasi-static part of the bed and to improve the continuum modelling parameterizations. In particular, the influence of the three main parameters, which are the size ratio r, the inertial number I and the small particle concentration ϕ_s, will be investigated through numerical experiments in the bedload configuration. The results will then be analysed in the framework of the segregation model of Thornton et al. (2006).

This work has led to the publication of a scientific article in *Journal of Fluid Mechanics* (Chassagne et al., 2020b).

3.1 DEM simulations of segregation dynamics

3.1.1 Numerical setup

The numerical setup is presented in figure 3.1. In the following, subscripts l and s denote quantities for large and small particles respectively. Initially, large particles of diameter $d_l = 6$ mm and small particles of diameter $d_s = 4$ mm, defining a size ratio of $r = 1.5$, are deposited by gravity over a rough fixed bed made of large particles. The particle and fluid densities are fixed respectively to $\rho^p = 2500\ \mathrm{kg\,m^{-3}}$ and $\rho^f = 1000\ \mathrm{kg\,m^{-3}}$. The size of the 3D domain is $30d_l \times 30d_l$ in the horizontal plane in order to have converged average values (Maurin et al., 2015) and is periodic in the streamwise and spanwise directions. The number of particles of each class is assimilated into a number of layers, N_l and N_s. The number of layers represents in terms of particle diameters the height that would be

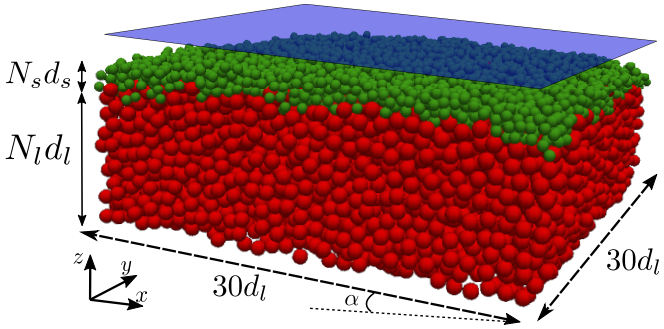

Figure 3.1: Numerical setup for $N_s = 2$. Initially, N_s layers of small particles ($d_s = 3$ mm) are deposited by gravity above N_l layers of large particles ($d_l = 6$ mm). N_s varies from 0.01 until 2 with N_l varying accordingly in order to always have $N_l d_l + N_s d_s = 10 d_l$.

occupied by the particles if the volume fraction was exactly $\Phi = 0.61$, the random close packing observed in the simulation. Equivalently, the volume occupied by large particles (resp. small particles) is $0.61 \times 30d_l \times 30d_l \times N_l d_l$ (resp. $0.61 \times 30d_l \times 30d_l \times N_s d_s$). Therefore, fixing N_l or N_s fixes the number of particles of each class. The height of the bed at rest is defined by $H = 1/2 d_l + N_l d_l + N_s d_s$, where the $1/2 d_l$ term accounts for the fixed particles at the bottom of the domain, and H is fixed to $10.5 d_l$ in all the simulations. The number of layers of fine particles N_s varies from 0.01 (only a few small particles) up to 2 layers (corresponding to figure 3.1), while N_l changes accordingly in order to keep $H = 10.5 d_l$. The bed slope is fixed to 10% (5.7°), representative of mountain streams, and the water depth is set to $h_w = 2.6 d_l$. It corresponds to a macroscopic Shields number of $\theta = \rho^f g h_w \sin(\alpha)/[(\rho_p - \rho_f) g d_l] = 0.17$ and to a microscopic Shields number of $\theta = \max(R^f_{xz}/[(\rho_p - \rho_f) g d_l]) \sim 0.12 - 0.13$.

At the beginning of each simulation, the fluid flows by gravity and sets particles into motion. A first transient phase takes place, during which fluid and particles are accelerating. Along this period, segregation is very fast and at the end of the transient phase, the small particles have already infiltrated into the first layers of the bed. It is therefore difficult to study size segregation in the bedload layer. It would require numerical tricks that are not easy to set up in order to keep small particles at the surface during the transient phase. For these reasons, in this chapter, the study focuses on the dynamics of segregation once the system is at transport equilibrium and small particles have reached the quasi-static region.

The horizontal averaged volume fraction per unit granular volume of small and large particles are defined as

$$\phi_s = \frac{\Phi_s}{\Phi}, \qquad \phi_l = \frac{\Phi_l}{\Phi}, \tag{3.1}$$

where Φ_s (resp. Φ_l) is the volume fraction of small (resp. large) particles defined per unit mixture volume as in the previous chapter. In the following, ϕ_s (resp. ϕ_l) will also be called small (resp. large) particle concentration. By definition, the two concentrations sum

to unity,

$$\phi_s + \phi_l = \frac{\Phi_s}{\Phi_s + \Phi_l} + \frac{\Phi_l}{\Phi_s + \Phi_l} = 1, \tag{3.2}$$

Lastly, z_c is defined as the vertical position of the center of mass of small particles,computed as

$$z_c(t) = \frac{\int \Phi_s(z) z dz}{\int \Phi_s(z) dz}, \tag{3.3}$$

and dz_c/dt is its velocity.

The results are presented in dimensionless form using the following dimensionless variables,

$$\tilde{z} = \frac{z}{d_l}, \quad \tilde{t} = t\sqrt{g/d_l}, \quad \widetilde{\langle v_x \rangle^p} = \frac{\langle v_x \rangle^p}{\sqrt{g d_l}}. \tag{3.4}$$

The large particle diameter d_l has been chosen as a reference length scale. Indeed we assume that the small particles are few enough not to perturb the bulk granular flow. The segregation mechanisms are interpreted as a response to the mean flow assumed to be a monodisperse granular flow of large particles. In the following, the tildes are dropped for sake of clarity.

3.1.2 Results

Simulations have been performed for different numbers of layers of small particles N_s. Figure 3.2a shows the temporal evolution of fine particle concentration profiles for the case $N_s = 2$, corresponding to two layers of small particles deposited on top of a bed made of large particles. At the beginning, the small particles, indicated by the high small particle concentration regions in green, infiltrate rapidly into the first few layers of large particles. As small particles infiltrate downward, large particles rise to the surface. The DEM simulations exhibit a two-layer structure, with small particles sandwiched between two layers of large particles. While infiltrating, the thickness of the small particle layer gets slightly larger. Profiles of concentration for different times are presented in figure 3.2b. The concentration profiles exhibit a Gaussian-like shape. After the transient phase, neither the maximal value (see figure 3.2c) nor the width of the profiles evolve in time, suggesting that the small particles infiltrate the bed as a layer having a constant thickness and being just convected downward by segregation inside large particles.

The vertical time and volume-averaged streamwise velocity profile of the particle mixture is plotted in figure 3.3a for all the simulations. All the curves are superimposed meaning that the response of the granular medium to the fluid flow forcing is not modified by the number of small particles. The granular forcing is therefore the same for all the simulations independently of the number of small particles at the initial condition. Between $z = 3$ and 8 approximately, the velocity profiles are linear in the semi-logarithmic plot, indicating that the velocity is exponentionally decreasing in the bed. This is characteristic of a quasi-static granular flow (Komatsu et al., 2001), or creeping flow (Houssais et al., 2015; Ferdowsi et al., 2017). Due to the presence of a fixed layer of particles, the velocity vanishes at the bottom of the domain. It is interesting to note that the entire bed is

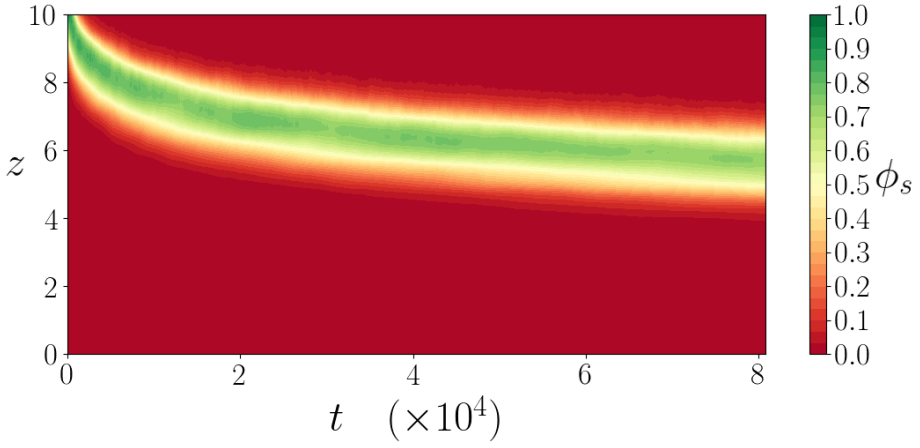

(a)

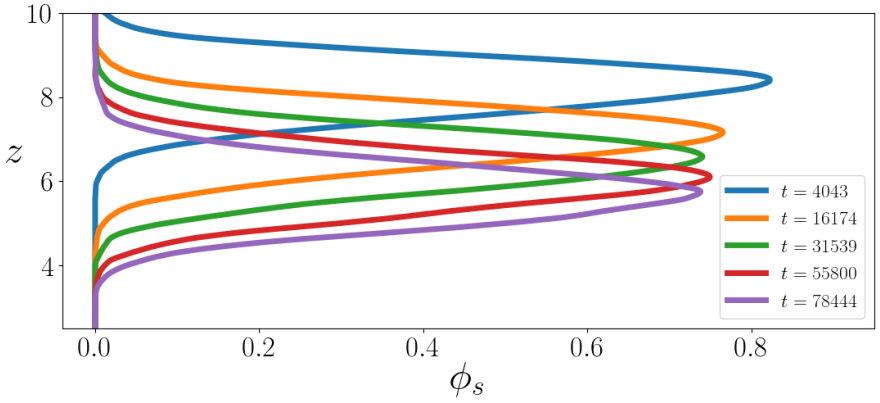

(b)

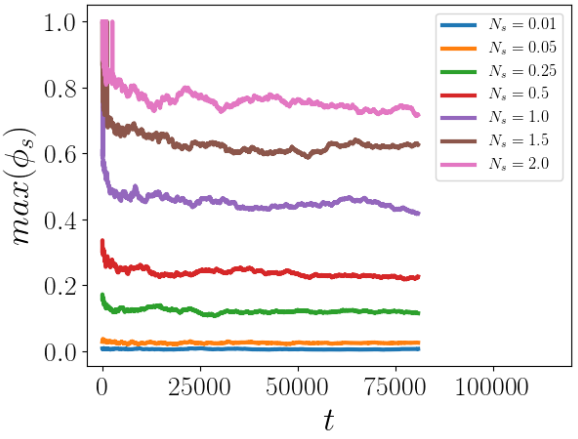

(c)

Figure 3.2: (a) Typical temporal evolution of fine particle concentration profile ϕ_s for the case $N_s = 2$, (b) concentration profiles in small particles for different times for the case $N_s = 2$ and (c) time evolution of the maximal value of ϕ_s for all simulations.

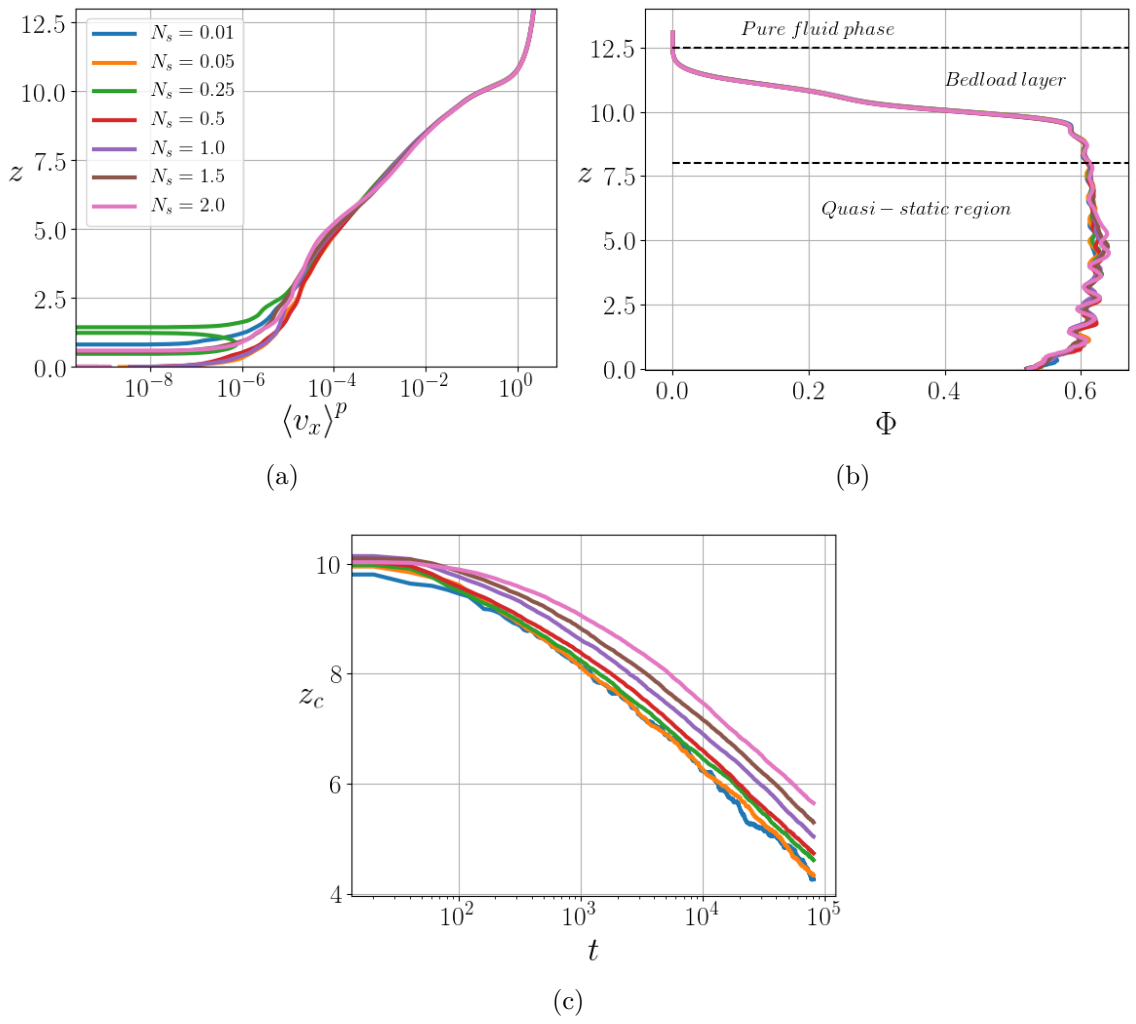

Figure 3.3: (a) Streamwise space time averaged particle velocity as a function of the height, (b) time averaged volume fraction of the granular mixture and (c) evolution of the vertical position of the mass center of small particles with time.

in motion, even if the velocity can be very low at the bottom of the quasi-static region. The time averaged solid volume fraction of the mixture is plotted in figure 3.3b for all the simulations. The quasi-static region is characterized by the bed at random close packing ($\Phi \sim 0.61$). Above $z \sim 8$, the volume fraction decreases to zero, corresponding to a transition zone between a quasi-static region and a pure fluid phase. Note that due to this decompaction of the bed at the surface, the total height of the bed is slightly larger than $10.5 d_l$. For the case $N_s = 2$, the velocity profile is slightly modified as well as the volume fraction profile with a small increase of volume fraction around $z \sim 5$. This very small increase originates from mixture effects and the volume fraction can exceed the random close packing (Cumberland and Crawford, 1987). The modifications on the velocity and volume fraction profiles are however small enough to consider that the small particles do not perturb the mean monodisperse flow. This supports the assumption that the segregation mechanisms can be considered in this configuration as a response to the mean monodisperse granular flow.

Since the small particles infiltrate the bed as a layer, the center of mass of the small particles, z_c, is a representative position of the entire layer. Figure 3.3c shows the temporal evolution of this position for all the simulations, in a semi-logarithmic plot. After the initial transient phase, the curves become linear, meaning that z_c is a logarithmic function of time

$$z_c = -a \ln(t) + b. \tag{3.5}$$

In equation (3.5), the coefficient a corresponds to the absolute slope of the curve and characterises the segregation velocity ($dz_c/dt = -a/t$). Whatever the number of small particles in the simulation, figure 3.3c shows that all the curves are parallel to each other, meaning that a is independent of the number of layers of small particles, N_s. Therefore the segregation velocity dz_c/dt is also independent of the number of layers of small particles.

In the following, these simulations will be analysed using the dimensional analysis presented in the introduction (equation (1.7)) with the aim to confirm the dependence of the segregation flux on the inertial number I and on the local concentration ϕ_s.

3.1.3 Dependence on the inertial number

In figure 3.4a, the dimensionless segregation velocity is plotted against the large particle inertial number $I = \dot{\gamma}^p d_l / \sqrt{P^p/\rho_p}$, where $\dot{\gamma}^p$ is the time averaged granular shear rate and P^p is the time averaged granular pressure. Note that in our configuration, and contrary to non-erodible granular flows, there is a large variation of I with z (figure 3.4b). The segregation velocity is higher for larger inertial number. The linearity of the curves shows that the segregation velocity is indeed a power law of the inertial number. For all the simulations a similar exponent is obtained, ranging from 0.81 to 0.88, and a best fit gives a value of 0.85 for the mean exponent,

$$\frac{dz_c(t)}{dt} \propto I^{0.85}(z_c(t)). \tag{3.6}$$

Interestingly, Fry et al. (2018) obtained, for dry granular flows at higher inertial

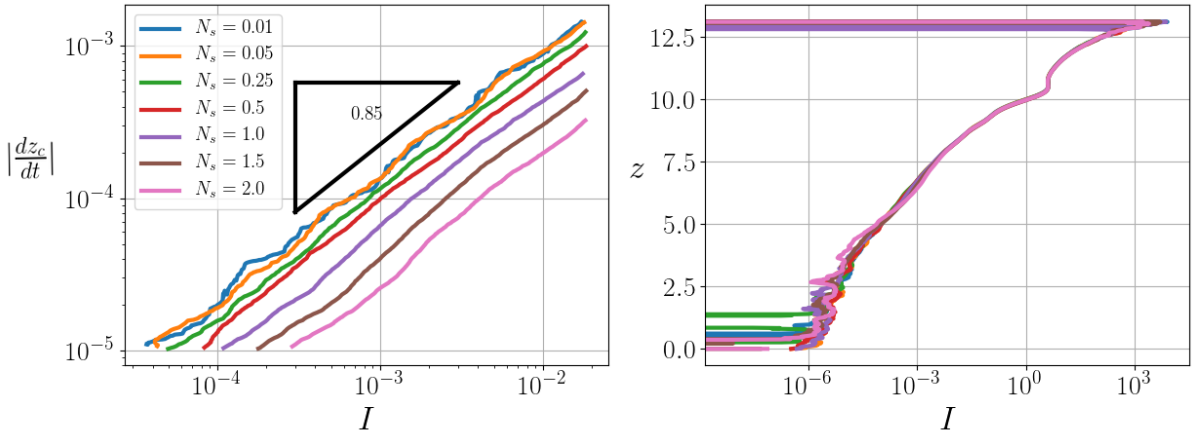

Figure 3.4: (a) Segregation velocity dependence on the local inertial number, (b) inertial number profile.

numbers ($I \in [10^{-2}, 1]$), an exponent 0.84, very close to the 0.85 exponent in the present configuration. Our results suggest that the behaviour observed by Fry et al. (2018) is valid in a wider range of inertial numbers, in particular, in the quasi-static regime ($I \in [10^{-5}, 10^{-2}]$).

The scaling with the inertial number (eq. 3.6) is in line with the theory of Savage and Lun (1988), who suggested relating the segregation velocity to the shear rate. Indeed the inertial number is the dimensionless ratio between the shear rate and the square root of pressure. In the bedload configuration, the pressure increases linearly with depth while the shear rate exponentially decreases in the bed. Therefore, most of the variation of the inertial number is contained in the shear rate. A scaling with the inertial number allows the effect of pressure P^p to be taken into account, which is small in this configuration. On the contrary in the configuration of Fry et al. (2018), the pressure displayed strong variations and the authors found a scaling with the inertial number and not with the shear rate. The similarity with the results of Fry et al. (2018) is encouraging in the understanding of size segregation in general and supports a scaling with the inertial number.

Equation (3.6) allows the temporal evolution of the fine particles center of mass to be understood. Figure 3.4b shows the inertial number profile for all simulations. The linearity of the curves, for $z \leq 8$, in the semi-logarihtmic plot indicates that the inertial number is an exponential function of z in the quasi-static part of the bed. Taking an exponential profile to the power 0.85, $I^{0.85}$ is also an exponential function of z and can be written as

$$I^{0.85}(z) = I_0 e^{z/c}. \tag{3.7}$$

N_s	a	c	error (%)
0.01	0.863	0.873	1.159
0.05	0.850	0.864	1.647
0.25	0.823	0.847	2.916
0.5	0.843	0.862	2.254
1	0.833	0.857	2.800
1.5	0.820	0.828	0.976
2	0.849	0.828	2.473

Table 3.1: Values of coefficients a (slope of the center of mass) and c (exponential decay of the inertial number to the power 0.85) obtained from fitting the curves of figures 3.3c and 3.4b and the error in percentage.

Introducing (3.7) into expression (3.6) leads to

$$\frac{dz_c(t)}{dt} = -b_1 e^{z_c(t)/c}, \tag{3.8}$$

with b_1 a positive constant. Equation (3.8) can be integrated

$$\int e^{-z_c/c} dz_c = \int -b_1 dt, \tag{3.9}$$

leading to

$$ce^{-z_c/c} = b_1 t + C_0 \sim b_1 t \quad \text{for } t \gg |C_0/b_1| \tag{3.10}$$

It can be rewritten as

$$z_c(t) = -c \ln(t) + b_2, \tag{3.11}$$

where $b_2 = -c \ln(b_1/c)$ is a constant.

This analysis shows that the logarithmic descent of the small particle center of mass is a consequence of the dependence of the segregation velocity on the inertial number. This is confirmed by the comparison between the coefficients a in equation (3.5) and c in equation (3.7), that should be equal. Fitting of the elevation of both the center of mass (figure 3.3c) and $I^{0.85}$ yields coefficients a and c (see table 3.1). The maximal difference between a and c is around 3% confirming the present analysis and showing that the inertial number is indeed the controlling parameter of the segregation velocity.

It has been verified in appendix A, that the segregation dynamics observed here and in particular the scaling of the segregation velocity with the inertial number were not dependent on the model parameters such as the material friction coefficient μ, the restitution coefficient e_n or the Richardson-Zaki exponent. These parameters have been varied and in all cases the same dynamics is observed with a scaling with the inertial number to the power 0.85.

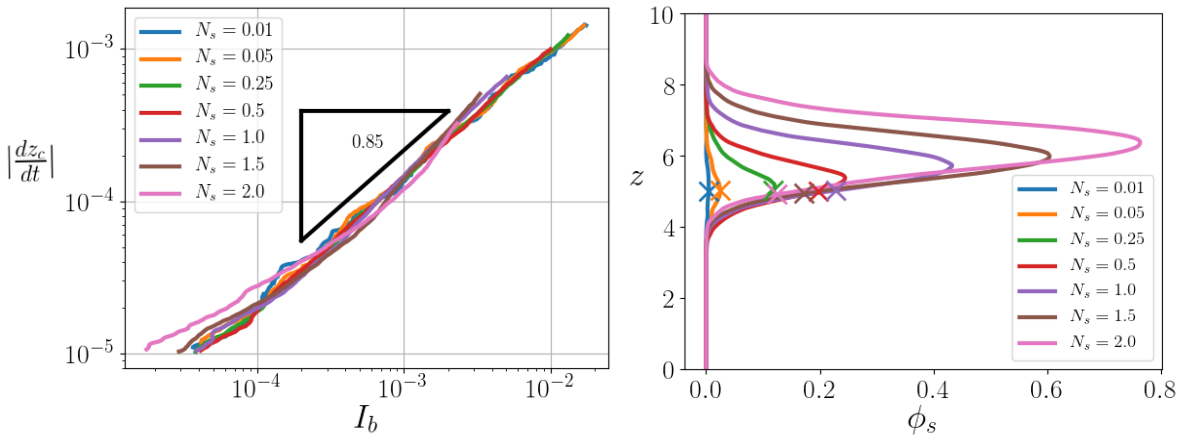

(a) (b)

Figure 3.5: (a) Center of mass velocity dependence on the inertial number at the bottom of the layer of small particles, (b) small particle concentration profiles at time $t = 40435$ and vertical position of the bottom of the layer ($\times$).

3.1.4 Bottom controlled segregation

While this analysis clearly explains the trends observed, figure 3.4a shows that for a given value of the inertial number, different segregation velocities are obtained depending on the initial number of small particles, N_s. This is quite surprising and seems at first in contradiction with figure 3.3c, where it was observed that the segregation velocity (given by the slope of the curve) is independent of N_s. To understand this apparent contradiction, it is necessary to change the point of view adopted in this problem.

Since the inertial number follows an exponential profile, it varies importantly throughout the layer of small particles. Thus, according to equation (3.6) the segregation velocity should be lower at the bottom than at the top of the layer. This lower segregation velocity at the bottom of the layer implies that all the small particles above cannot move downward faster than the lowest particles in the layer. Defining the position of the bottom of the layer as $z_b = z_c - W/2$, with $W = 2N_s d_s/d_l$ the small particle layer thickness, figure 3.5a shows the dependence of the segregation velocity on the inertial number at the bottom of the layer. All the curves collapse on a master curve and a power law relationship is found between the segregation velocity and the inertial number at the bottom of the layer $I_b(z_c) = I(z_b)$,

$$\frac{dz_c(t)}{dt} = -\alpha_0 I_b^{0.85}(z_c(t)), \tag{3.12}$$

where α_0 is a positive constant independent of the number of layers of small particles. This result shows that the segregation velocity of the layer is indeed completely controlled by the inertial number at the bottom of the small particle segregating layer and it does not contain any dependence on the number of small particle layers, N_s.

The layer thickness has been chosen to be two times the thickness it would occupy if only small particles were present, $W = 2N_s d_s/d_l$. This choice is motivated by the fact that the layer is formed of a mixture of both large and small particles. Figure 3.5a shows that for the different cases, the obtained width is indeed consistent with the actual thickness. Note that when N_s tends to zero, z_b tends to z_c the center of mass of the small particles. In the extreme case where only one small particle is present, this position corresponds to its center. Figure 3.5b shows, at dimensionless time $t = 40435$, the profiles of small particle concentration, where the crosses denote the position of the bottom of the layer. The lower limbs of the concentration profiles are superimposed and the position of the bottom of the layer is identical for all tested values of N_s. Whatever the number of small particles, they pile up above the bottom position, where the segregation dynamics is controlled.

This dynamics is clearly due to the exponential inertial number profile, which imposes a very strong decrease of the segregation velocity with depth, resulting in the formation of a small particle stable layer. The exponential decrease of the inertial number is characteristic of flows on erodible beds and this bottom controlled segregation dynamics is therefore expected to occur in any flow of this type.

It is remarkable that this continuum description, in terms of mass center position evolution (eq. 3.12), is applicable even for the cases $N_s = 0.01$ and $N_s = 0.05$. These cases correspond to very few non interacting particles and a continuum vision seems at first hardly relevant. This can be explained by the bottom controlled dynamics. Indeed, the bottom position is a stable position for segregation. If the particle is late and is above z_b, it will soon reach the bottom position because the inertial number is higher at its position. And inversely if the particle is in advance compared to the bottom position. Therefore, the isolated particles are placed at the bottom position. Since for cases $N_s = 0.01$ and $N_s = 0.05$, z_b and z_c are located at the same elevation, the continuum description captures the dynamics of isolated particles.

This analysis highlights the dependence of segregation on the inertial number in bedload transport. Furthermore, the bottom of the small particle layer is shown to be a key position that controls segregation. In particular, it explains why the small particles infiltrate the bed as a layer of constant thickness.

3.1.5 Size ratio influence

The analysis presented above provides a reference position that describes the segregation dynamics. In the following, the effect of the size ratio is investigated. The previous simulations were all performed at the same size ratio, $r = 1.5$. According to the dimensional analysis performed in the introduction (section 1.2), the following relationship is expected,

$$\frac{dz_c(t)}{dt} = -\alpha_0 \mathcal{G}_1(r) I_b^{0.85}(z_c(t)). \tag{3.13}$$

A set of simulations in which the diameter of the small particles is varied has been performed. It covers a range of size ratios from $r = 1.15$ to 3. In all these simulations, the number of small particle layers is fixed to $N_s = 1$. The dependence of the center of mass

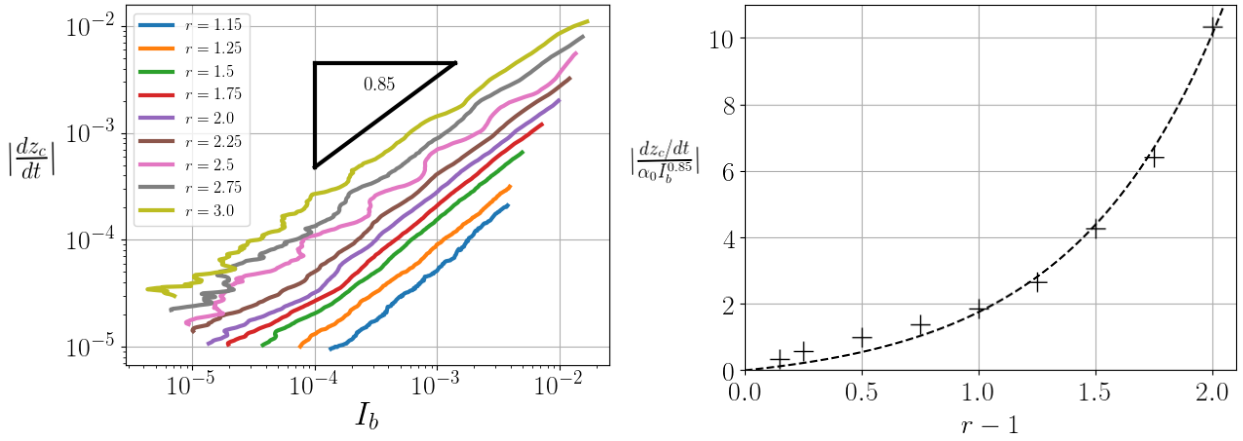

(a) (b)

Figure 3.6: (a) Center of mass velocity dependence on the inertial number at the bottom of the layer of small particles for different size ratio. Note that for $r = 2.5$, $r = 2.75$ and $r = 3$, simulations were performed with a $15d_l \times 15d_l$ box in order to gain computation time. (b) Best fit coefficient between the segregation velocity and the inertial number to the power 0.85 times α_0 as a function of the size ratio minus one (for each curve of figure 3.6a, one point is obtained). The function $\mathcal{G}_1$ is plotted as dashed line.

velocity on the inertial number at the bottom of the layer of small particles is plotted in figure 3.6a. A similar power law relationship is recovered, showing that the inertial number is still the controlling parameter. The best fit provides a 0.82 exponent for the inertial number dependency, which is in the range of values found previously. However, to remain consistent with the previous analysis an exponent of 0.85 is used in what follows. The curves are parallel but not superimposed, which implies that, as expected, the size ratio plays an important role in the segregation dynamics. The dependence with the size ratio is presented in figure 3.6b, where the ratio between the segregation velocity and the inertial number to the power 0.85 is plotted as a function of the size ratio minus one. The dependence of the segregation velocity increases strongly with the size ratio and tends to zero when r is close to unity, cancelling segregation in the monodisperse limit. The following functional form for $\mathcal{G}_1$ is proposed,

$$\mathcal{G}_1(r) = 0.45\left(e^{(r-1)/0.63} - 1\right), \tag{3.14}$$

fitting empirically the data (see the dashed line in figure 3.6b).

The maximal segregation efficiency at $r = 2$ reported by Golick and Daniels (2009), Thornton et al. (2012) and Guillard et al. (2016) is not recovered in this configuration, as the segregation velocity still increases for $r > 2$ ($r - 1 > 1$ in figure 3.6b). These studies essentially focused on the rise of a few large particles. In particular, Guillard et al. (2016) focused on the rise of a single large intruder in a small particle bed. This difference in the size ratio dependency could be explained by an asymmetry in the segregation behaviour,

as already observed by Van der Vaart et al. (2015) with shear cell experiments. Indeed, there is no reason that the infiltration of a small particle in a bed made of large particles should have a maximum efficiency at a given size ratio. The larger the size ratio, the easier the small particles find holes in which to fall. In addition, when the size ratio increases beyond $r \sim 6$, the segregation regime is modified from a frictional regime (kinetic sieving) toward a purely gravity controlled regime called spontaneous percolation. The rise of a large particle is however only a frictional process, whatever the size ratio (Guillard et al., 2016). My intuition is that the rise of a large particle is related to the number of contacts with surrounding particles, which increases with the size ratio. When the size ratio is infinite, there is an infinite number of contacts and small particles should act as a pure buoyant fluid. On the contrary the infiltration of a small particle is related to the size of the holes in which to fall, which increases with the size ratio. These assumptions would of course need more work but it could explain the segregation asymmetry observed by Van der Vaart et al. (2015) in a shear cell.

To summarize, the results presented here suggest that the segregation dynamics in bedload transport can be described, to leading order, by the following relationship,

$$\frac{dz_c}{dt} = -\alpha_0 \mathcal{G}_1(r) I_b^{0.85}, \tag{3.15}$$

where α_0 can be computed from figure 3.5a and $\mathcal{G}_1(r)$ is given by equation (3.14).

3.2 Discussion in the framework of continuum modelling

Beyond the dependence on the inertial number and the size ratio, it is remarkable that the trends observed for the evolution of the center of mass and for the segregation velocity are independent of the number of small particle layers, N_s. Indeed, as the latter is increased from 0.01 to 2, the configuration moves from a few isolated (non-interacting) small particles to two consistent layers of small particles infiltrating collectively inside the coarse bed. Therefore, it is expected that the increase of N_s, would increase the local particle concentration and reduce the segregation velocity due to particle hindrance effects.

This independence of the trend observed in the segregation velocity seems in contradiction with the literature (e.g. Savage and Lun, 1988; Dolgunin and Ukolov, 1995; Van der Vaart et al., 2015; Jones et al., 2018). Indeed, in these studies, a major influence of the local small particle concentration on the segregation velocity has been evidenced. In order to explain this apparent contradiction and to get more insight into the physical processes at play, the results are discussed in the following as a function of local mechanisms within the framework of the continuum model of Gray and Thornton (2005), Thornton et al. (2006) and Gray and Chugunov (2006).

3.2.1 Local mechanism interpretation

In order to explain the apparent independence of the results on the concentration of small particles, a local analysis in the theoretical framework of continuum modelling is developed. The model of Thornton et al. (2006) (eq. 1.22), presented in the introduction chapter (section 1.3.2), will be used as a baseline. In the present configuration, the velocity field has only a streamwise component (along x) and all quantities only depend on z. Therefore, the advection by the bulk flow $\nabla \cdot (\phi_s \boldsymbol{u})$ vanishes. As a first step, diffusion is not considered and equation (1.22) simplifies to a purely hyperbolic equation,

$$\frac{\partial \phi_s}{\partial t} - \frac{\partial F_s}{\partial z} = 0. \tag{3.16}$$

Remembering that the segregation flux is the product of the segregation velocity by the small particle concentration and combining the form proposed in the introduction $F_s \propto \mathcal{G}_1(r) I^{\zeta} \phi_s (1 - \phi_s)$ with the analysis of the DEM simulations (eq. 3.15), it can be written as

$$F_s = \alpha_0 \mathcal{G}_1(r) I^{0.85} \phi_s (1 - \phi_s), \tag{3.17}$$

where α_0 can be fitted in the DEM results from equation (3.12). Since the inertial number is exponentially decreasing with depth (eq. 3.7), the segregation flux simplifies to

$$F_s = S_{r0} e^{z/c} \phi_s (1 - \phi_s), \tag{3.18}$$

with $S_{r0} = \alpha_0 \mathcal{G}_1(r) I_0$. The inertial number does not depend on the number of small particles (figure 3.4b) so S_{r0} is independent on the initial number of small particles and only depends on the response of the granular mixture to the fluid flow forcing through I_0 and c. For $r = 1.5$, the corresponding value of S_{r0} obtained from the DEM simulations is: $S_{r0} = 3.70 \times 10^{-8}$. Due to the exponential decrease of the inertial number in the bed, the form of the segregation flux, F_s, is also exponential with z. May et al. (2010) already proposed an analytical solution for an exponential flux, but the flow was shear-driven from the bottom. Proceeding similarly, the analytical solution can be derived using the method of characteristics (appendix B), for which the initial condition is simply a step of concentration representing an initial pure layer of small particles lying on a bed made of large particles.

$$\phi_s(z, t = 0) = \begin{cases} 0, & z < z_i, \\ 1, & z \geq z_i, \end{cases} \tag{3.19}$$

with $z_i = N_l d_l$.

The analytical solution is plotted in figure 3.7 for the case $N_s = 1$ and $r = 1.5$. Figure 3.7a corresponds to the very first times of the solution, while figure 3.7b is the long time solution. The initial discontinuity leads to an expansion fan delimited by two characteristics (see figure 3.7a). The first, denoted z_1, is going down and meets the bottom of the domain at time t_1. This time is very long as it corresponds to the the time at which the first small particle touches the bottom boundary position. That case was never reached in our DEM simulations, and the analytical solution is therefore not plotted until this

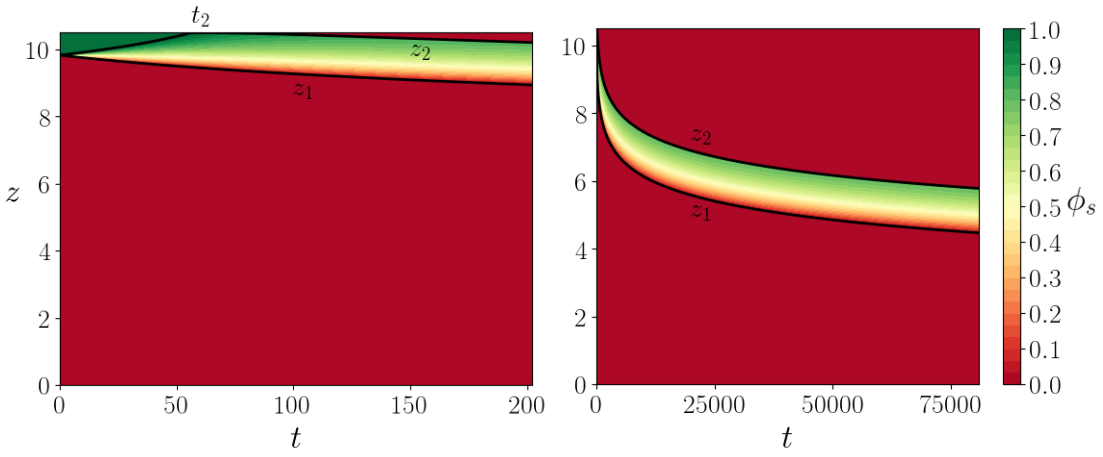

Figure 3.7: Case $N_s = 1$, $r = 1.5$ space time evolution of the concentration in small particles ϕ_s at different time scales. Note that the scale in the abscissa is drastically different in both figures.

time. The second characteristics delimiting the expansion fan is going up and is denoted z_2. When it meets the top of the domain at time t_2 (i.e. when the first large particle reaches the top boundary, which happens very rapidly), a shock is created that travels downward. It can be shown (see Appendix B) that the analytical solution for time $t_2 \leq t \leq t_1$ is

$$\phi_s(z,t) = \begin{cases} 0, & z < z_1(t), \\ \phi_{fan}(z,t), & z_1(t) \leq z \leq z_2(t), \\ 0, & z > z_2(t), \end{cases} \tag{3.20}$$

where z_1 is the characteristic curve (eq. 3.21) delimiting the bottom of the rarefaction zone, z_2 is given by the shock equation (3.22) delimiting the top of the rarefaction zone and ϕ_{fan} is the solution in the expansion fan given by equation (3.23),

$$z_1(t) = z_i - c \ln\left(1 + \frac{S_{r0}}{c} e^{z_i/c} t\right), \tag{3.21}$$

$$\frac{dz_2}{dt} = -S_{r0} e^{z_2/c} \left(1 - \phi_s(z_2,t)\right), \tag{3.22}$$

$$\phi_{fan}(z,t) = \frac{1}{2} - \frac{c}{S_{r0}t} e^{-z/c} + \frac{c}{S_{r0}t} e^{-(z+z_i)/(2c)} \sqrt{1 + \left(\frac{S_{r0}t}{2c}\right)^2 e^{(z+z_i)/c}}. \tag{3.23}$$

In figure 3.7b, the long time solution shows similar properties than the DEM results. In particular, the small particle phase seems to segregate as a layer of constant thickness. Despite the complexity of the solution (3.20), some simplifications can be made for long times (but smaller than t_1) to study the properties of the analytical solution. Indeed for $t \gg 4c/S_{r0}e^{z_i/c} \sim 1000$, it can be shown (see appendix B) that the square root term in

equation (3.23) simplifies to

$$1 + \left(\frac{S_{r0}t}{2c}\right)^2 e^{(z+z_i)/c} \sim \left(\frac{S_{r0}t}{2c}\right)^2 e^{(z+z_i)/c}, \tag{3.24}$$

and the volume fraction profile ϕ_s in the rarefaction fan simplifies as,

$$\phi_{fan}(z,t) = 1 - \frac{c}{S_{r0}t} e^{-z/c}. \tag{3.25}$$

Some simplifications can also be made on the boundary curves of the rarefaction zone z_1 and z_2. Introducing the long time solution (3.25) in the shock equation of z_2 (3.22), a much more simple equation of z_2 is obtained for long times

$$\frac{dz_2}{dt} = -\frac{c}{t}, \tag{3.26}$$

for which the solution is

$$z_2(t) = -c\ln(t) + \beta, \tag{3.27}$$

where β is an integration constant. Concerning the characteristic curve z_1, the term in the logarithm in equation (3.21) simplifies for long times to

$$1 + \frac{S_{r0}}{c} e^{z_i/c} t \sim \frac{S_{r0}}{c} e^{z_i/c} t, \tag{3.28}$$

and the following expression is obtained for z_1

$$z_1(t) = -c\ln(t) - c\ln\left(\frac{S_{r0}}{c}\right). \tag{3.29}$$

Therefore, the upper and lower bounds of the small particle layer, z_2 and z_1, both move down asymptotically as $-c\ln(t)$, and the layer thickness $z_2(t) - z_1(t)$ is constant. Lastly, the form of the flux considered in the continuum model $F_s \propto I^{0.85}\phi_s(1-\phi_s)$ implies that the vertical velocity of the small particles $w_s = -F_s/\phi_s$ is

$$w_s(z,t) = -\frac{S_{r0}}{I_0} I^{0.85}(z)(1 - \phi_s(z,t)). \tag{3.30}$$

Using equation (3.25), the vertical velocity can be expressed for long times as

$$w_s(z) = -\frac{S_{r0}}{I_0} I^{0.85} \frac{c}{S_{r0}t} e^{-z/c}, \tag{3.31}$$

and remembering that $I^{0.85} = I_0 e^{z/c}$,

$$w_s(z) = -\frac{c}{t}. \tag{3.32}$$

Considering long time solutions and an imposed forcing by the inertial number, the

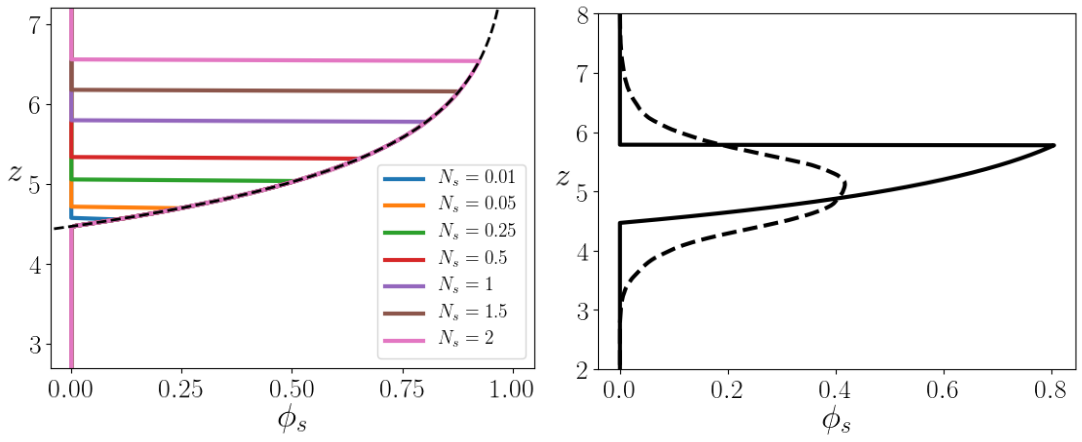

(a) (b)

Figure 3.8: (a) Profiles of concentration at time $t = 80870$ with the continuum model without diffusion for several values of N_s. Long time expression (3.25) is indicated as dashed line. The same values of S_{r0} and c have been used. (b) Comparison between DEM simulations (----) and segregation model (——) of the profile of concentration ϕ_s for the case $N_s = 1$ at time $t = 80870$.

model exhibits the exact same behavior observed in the DEM simulations. First, the small particles move down as a layer into the coarse particles, with the lower and upper bounds showing a logarithmic decrease with time (equations 3.27 and 3.29). This decrease, at a common slope $-c$ related to the forcing, imposes a constant layer thickness with time, as observed in the DEM simulations. The consequence is that the segregation velocity of the small particles is the same throughout the layer (eq. (3.32)). Considering the formulation of the downward velocity of small particles (eq. 3.30), this means that the product of the small particle concentration and the inertial number is constant within the small particle layer, so that

$$w_s(z,t) = -\frac{S_{r0}}{I_0} I^{0.85}(z)(1-\phi_s(z,t)) = -c/t. \tag{3.33}$$

This is a very important property. At a given time, it means that the shape of the small particle concentration profile responds directly to the variation of the inertial number as a function of z. At a point within the layer, the decrease of the inertial number observed when going downward is compensated for by an increase of the term $1-\phi_s$, and so a decrease of the small particle concentration. This competition between the effect of the inertial number and the local concentration results in the shape of solution profiles presented in figure 3.8a, for which the expression is given by equation (3.25).

In order to corroborate the explanation of the mechanisms at play, the lower bound of the small particle layer z_1 for which $\phi_s = 0$ is considered. It corresponds, in figure 3.8a, to the position where all profiles collapse to zero at the bottom. This position is the lower bound of the rarefaction fan and corresponds to the bottom of the small particle layer.

N_s	0.01	0.05	0.25	0.5	1	1.5	2
$\frac{\lvert z_1 - z_b \rvert}{z_1}(\%)$	0.28	0.22	0.50	0.09	0.04	0.73	0.95

Table 3.2: Mean error between the bottom position from the DEM simulations z_b and from the continuum model z_1. The maximal error of less than 1% between both positions suggests agreement.

At this position, as $\phi_s = 0$, the segregation velocity (eq. 3.30) is only a function of the inertial number at the bottom of the layer:

$$w_s(z,t) = -\frac{S_{r0}}{I_0} I_b^{0.85}, \tag{3.34}$$

where $I_b^{0.85} = I^{0.85}(z_1)$. As the segregation velocity is constant throughout the layer, this means that the vertical velocity of the whole layer is controlled by the inertial number at the bottom position. This corresponds exactly with the observations in the DEM simulations in §3.1.4, where the segregation velocity was shown to collapse as a function of the inertial number at a position considered to be the bottom of the small particle layer. The correspondence between the inertial number at the bottom position z_b observed in DEM and calculated from the analytical continuum model z_1 (table 3.2) confirms that the mechanisms described here are indeed the ones at play in the DEM simulations.

Finally it is interesting to note in figure 3.8a, that all the profiles tend to zero at the same position, meaning that the bottom position is the same whatever the quantity of small particles. This confirms the DEM result that the segregation velocity is independent of N_s. Indeed, if there are more small particles, they pile up above the others without changing the position of the bottom where the segregation dynamics is controlled.

To summarize this section, the continuum model has shown its ability to reproduce the main properties of the DEM results. The complex analytical solution has been analysed for long times. The small particle phase segregates as a layer of constant thickness, the velocity of which is controlled by the value of the inertial number at the bottom position. This layer behaviour is shown to be related to a local equilibrium between the influence of the concentration and of the inertial number. This explains the apparent contradiction with the literature concerning the effect of the concentration. The ϕ_s constant lines are parallels, going down at the same velocity, but this is the results of the combined effects of the inertial number and small particle concentration. So, there is a concentration effect in this segregation problem. Of course this complex segregation dynamics is the results of the complex forcing with an exponential inertial number profile.

The continuum model without diffusion, enabled understanding of the local segregation mechanisms and gave insights into the underlying physical mechanisms. While this model gives a good agreement at first order, as shown in figure 3.8b, it clearly lacks diffusion in

order to reproduce quantitatively the DEM simulations.

3.2.2 Diffusion and upscaling in a continuum framework

The continuum model used in the previous subsection can be expanded to account for diffusion (Gray and Chugunov, 2006), in order to quantitatively reproduce the DEM results. The equation to be solved is then given by,

$$\frac{\partial \phi_s}{\partial t} - \frac{\partial F_s}{\partial z} = \frac{\partial}{\partial z}\left(D\frac{\partial \phi_s}{\partial z}\right), \tag{3.35}$$

with a segregation flux of the form $F_s = S_{r0}e^{z/c}\phi_s(1-\phi_s)$, with $S_{r0} = 3.70 \times 10^{-8}$ fitted on the DEM simulations, and a diffusion coefficient $D(z)$, which is supposed to depend only on the vertical coordinate z.

Equation (3.35) is complex and the full solution can not be computed analytically. In the present work, a long time asymptotical solution is presented. At long times, DEM simulations have shown that the shape of the concentration profile ϕ_s is self-similar and is only advected downward like a travelling wave. Indeed, the layer of small particles moves down as a layer of constant thickness as $-c\ln(t)$ (see equation (3.11)) and the shape of the concentration profile does not evolve with time. The following change of variable is proposed to place the problem in the moving frame associated with the small particles,

$$\tau = t, \quad \xi = z + c\ln(t). \tag{3.36}$$

Equation (3.35) in the moving frame becomes

$$\frac{\partial \phi_s}{\partial \tau} + \frac{c}{\tau}\frac{\partial \phi_s}{\partial \xi} - \frac{\partial}{\partial \xi}\left(\frac{S_{r0}}{\tau}e^{\xi/c}\phi_s(1-\phi_s)\right) = \frac{\partial}{\partial \xi}\left(D(\xi - c\ln(\tau))\frac{\partial \phi_s}{\partial \xi}\right). \tag{3.37}$$

For a travelling wave, the solution to equation (3.37) should not depend on time τ. Assuming $\partial\phi_s/\partial\tau = 0$, this requires that $\tau D(\xi - c\ln(\tau))$ is independent of τ. This implies

$$\frac{\partial}{\partial \tau}\left(\tau D(\xi - c\ln(\tau))\right) = 0, \tag{3.38}$$

and distributing the derivative with τ, the following differential equation is obtained

$$D'(\xi - c\ln(\tau)) - \frac{1}{c}D(\xi - c\ln(\tau)) = 0, \tag{3.39}$$

for which the solution is

$$D = D_0 e^{(\xi - c\ln(\tau))/c} = D_0 e^{z/c}. \tag{3.40}$$

This shows that the only way to obtain a time independent solution is that the diffusion coefficient has an exponential structure with the same vertical dependence as the advection flux F_s. This exponential shape for the difusion coefficient is not really surprising. Indeed, diffusion is expected to be stronger for a more agitated bed, which in this configuration

decreases exponentially. Previous works (Campbell, 1997; Utter and Behringer, 2004; Cai et al., 2019) proposed to relate the diffusion coefficient to the shear rate. As $I^{0.85} = I_0 e^{z/c}$, equation (3.40) shows that, in the quasi-static part of the bed, the diffusion coefficient should be proportional to the inertial number with the same dependence as the segregation flux. Under this assumption, equation (3.37) becomes

$$c\frac{\partial \phi_s}{\partial \xi} - \frac{\partial}{\partial \xi}\left(S_{r0} e^{\xi/c}\phi_s(1-\phi_s)\right) = \frac{\partial}{\partial \xi}\left(D_0 e^{\xi/c}\frac{\partial \phi_s}{\partial \xi}\right). \tag{3.41}$$

By integration, and imposing $\phi_s \to 0$ when $\xi \to \pm\infty$, the following equation is obtained

$$\frac{\partial \phi_s}{\partial \xi} - \frac{S_{r0}}{D_0}\phi_s\left[\phi_s - \left(1 - \frac{c}{S_{r0}}e^{-\xi/c}\right)\right] = 0, \tag{3.42}$$

for which the solution is

$$\phi_s = \frac{e^{-\frac{S_{r0}}{D_0}\xi - \frac{c^2}{D_0}e^{-\xi/c}}}{C - \frac{S_{r0}}{D_0}\int_{-\infty}^{\xi}\left(e^{-\frac{S_{r0}}{D_0}\xi' - \frac{c^2}{D_0}e^{-\xi'/c}}\right)d\xi'}, \tag{3.43}$$

where C is a constant satisfying the mass conservation $N_s = \int_{-\infty}^{+\infty}\phi_s d\xi$. The travelling wave solution has a complex dependency on ξ and contains an integral which cannot be computed analytically. A semi-analytical approach is developed, where the integral is computed numerically and a numerical optimization is performed on the C coefficient so that $\int_{-\infty}^{+\infty}\phi_s d\xi$ corresponds to the initial mass of small particles introduced in the model.

Figure 3.9 compares the travelling wave solution (3.43) with concentration profiles from the DEM simulations (case $N_s = 1$, $r = 1.5$) at different times. The D_0 coefficient was computed in order to minimize the root mean square of the difference between the DEM and the travelling wave solution. The travelling wave solution agrees very well with all DEM profiles. Although the DEM concentration profile seems Gaussian, equation (3.43) shows that the profile is complex and not symmetric. This could have been inferred from the analytical solution without diffusion (figure 3.8a), which is not symmetric and exhibits a discontinuity at the top.

In order to keep the thickness of the small particle layer constant, both the advection and the diffusion coefficients must have the same exponential vertical structure. Defining a Peclet number as the ratio between the segregation intensity and the diffusion coefficient, $Pe = S_r(z)/D(z) = S_{r0}/D_0$, the travelling wave solution leads to a constant Peclet number with depth. The relative effect of segregation and diffusion fluxes is constant and independent of z. At each depth, the balance between advection and diffusion has to be the same to maintain the constant layer thickness observed in the DEM simulations.

The value of the Peclet number increases with the number of layers of small particles N_s and is plotted in figure 3.9b. Since the value of S_{r0} is the same whatever the number of layers of small particles, this result suggests that the value of the diffusion coefficient decreases

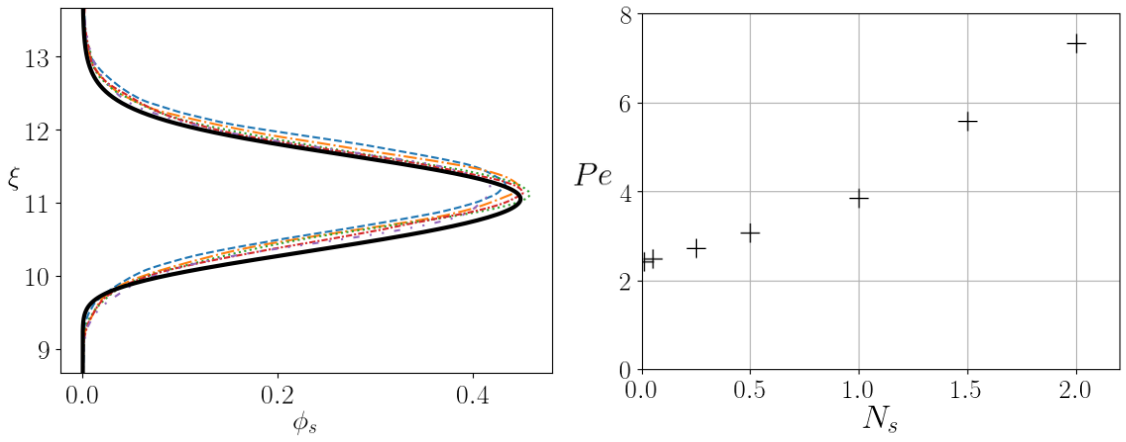

(a) (b)

Figure 3.9: (a) Travelling wave solution (——) and concentration profiles in the moving frame from DEM simulations at different times for the case $N_s = 1$, $r = 1.5$, $Pe = 3.86$. $t = 40435$ (----), $t = 50543$ (– · –), $t = 60652$ (·····), $t = 70761s$ (–·–·–), $t = 80870$ (–··–··–), (b) Value of the Peclet number as a function of the number of layers of small particles.

with N_s. This would indicate that diffusion is more efficient when there are fewer small particles. This is not surprising. Indeed if small particles are more concentrated, it will be more difficult for them to diffuse in the large particles. In addition, the mean value of the local small particle concentration ϕ_s globally increases with N_s (see figure 3.5b). Therefore, the dependence of the diffusion coefficient with N_s could be a global manifestation of a dependence of the diffusion coefficient with the local concentration ϕ_s. This dependence could be interpreted as a hindrance effect.

This study has shown that both the segregation flux and diffusion need to be proportional to the inertial number to the power 0.85 in order to represent the dynamics of segregation in bedload transport.

3.3 Conclusion

Vertical size-segregation in bedload transport has been studied with both a discrete and continuum approach. Focusing on the quasi-static region - common to any granular flow on an erodible bed - it has been shown with DEM simulations that small particles infiltrate the coarse quasi-static bed with the same behavior, irrespective of whether there are just a few isolated particles or two coherent layers of small particles. All the different configurations exhibit the same segregation velocity, related to a power law of the inertial number, generalizing the results observed for larger inertial numbers in confined bidisperse granular mixtures without fluid (Fry et al., 2018). In the present configuration, the dynamics of the infiltration of small particles is totally controlled by the bottom of the small particle layer, as the inertial number decreases exponentially from the top to the

bottom of the layer. As a consequence, the small particles segregate down as a layer of constant thickness.

The continuum size-segregation model of Gray and Thornton (2005), Thornton et al. (2006) and Gray and Chugunov (2006) has been shown to reproduce quantitatively the DEM simulations, with a small particle layer of constant thickness segregating at a velocity independent of the thickness of the layer. In the continuum model, this comes from a perfect balance, at any elevation, between the effect of the inertial number and the local small particle concentration. This analysis demonstrates that the macroscopic segregation behavior always results from a local equilibrium between the inertial number forcing and the local small particle concentration. Moreover, based on the derivation of an analytical solution with a travelling wave approach, the results show that the diffusion coefficient and the segregation flux in the continuum model should have the same dependency on the inertial number, leading to a constant Peclet number.

This chapter represents an original contribution on segregation processes in bedload transport, and more generally in granular flows. This is a first step toward upscaling particle scale results of grain size-segregation in continuum models for sediment transport. The macroscopic effects controlling size segregation have been understood. They have however not been related to the mechanisms at the particle scale. This is investigated in the next chapter.

Chapter 4

From particle-scale to continuum modelling of size segregation

The results presented in the previous chapter has given a precise description of both the dynamics and the controlling parameters of size segregation during bedload transport in the quasi-static regime. The continuum model shows very good agreement with the DEM simulations, indicating that size segregation can indeed be interpreted as a combination of advection and diffusion. The advection and diffusion coefficients have been shown to be directly proportional to the inertial number to the power 0.85. Although very accurate, this parametrisation still lacks a physical basis that could explain the form and dependencies of the coefficients.

The study presented in this chapter is the result of a collaborative work with Hugo Rousseau, PhD student at INRAE, and has led to submission of a scientific paper in *Journal of Fluid Mechanics*, currently under review. The prepint is available at `https://arxiv.org/abs/2005.09435`. This work originates from the observation that there is no continuum model for size segregation based on the particle scale forces. Based on the segregation force of Guillard et al. (2016) and interparticle drag force of Tripathi and Khakhar (2011a) presented in the introduction, Hugo Rousseau derived a new three phase flow model (two granular phases and one fluid phase) and a new advection-diffusion segregation model. The derivation provides advection and diffusion coefficient formulations as a function of particle scale forces, giving them a clear physical origin. The contribution of my PhD work is the development of a numerical method to solve this new advection-diffusion model and the analysis with the help of the results presented in the previous chapter.

In a first section, the derivation of the new advection-diffusion model is briefly presented. Then the numerical method is developed in section 4.2. The results are presented and compared with the DEM simulations in section 4.3.1. The new advection and diffusion coefficients are analysed to interpret the results obtained with the DEM simulations (section 4.3.2). By comparison with the DEM simulations, missing dependencies are revealed in the particle scale forces and new parametrisations are proposed.

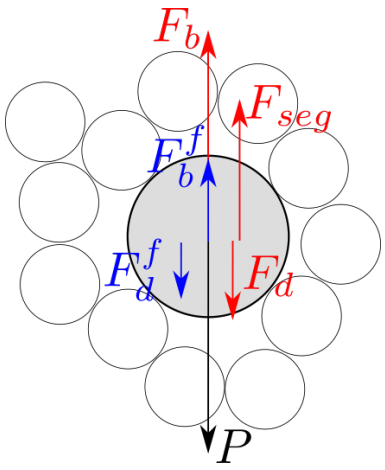

Figure 4.1: Forces applied on a single large intruder in a small particle bed immersed in a fluid. Interparticle forces are pictured in red and hydrodynamic forces in blue.

4.1 Advection-diffusion segregation model based on particle-scale forces

In the introduction chapter, it has been shown that a single large intruder of diameter d_l in a small particle bed of diameter d_s is submitted to four forces : its own weight $P = -\rho^p V_l g \cos(\alpha)$, a granular buoyancy force F_b, a segregation force F_{seg} and a granular drag force F_d. The granular buoyancy force was shown by Tripathi and Khakhar (2011a) to be proportional to the granular pressure as $F_b = -V_l/\Phi \partial P^p/\partial z$. The segregation force, evidenced by Guillard et al. (2016), is proportional to the granular pressure gradient and it has been shown in the introduction that it can be considered as a default of granular buoyancy force. The granular drag force has been demonstrated by Tripathi and Khakhar (2011a) to be a Stokesian drag force proportional to the granular viscosity and to the velocity difference between the intruder w_l and surrounding particles w_p as $F_d = -c\pi d_l \eta^p (w_l - w_p)$. In the bedload configuration, one also has to consider a fluid buoyancy force $F_b^f = \rho^f V_l g cos(\alpha)$, where ρ^f is the fluid density, and a fluid drag force F_d^f. For an intruder inside the bed, fluid inertial effects are small and can be neglected. The fluid drag force can therefore be approximated as a Stokesian drag force (Stokes, 1851) $F_d^f = 3\pi\eta^f d_l (w_l - w_f)$, where η^f is the fluid viscosity and w_f is the vertical fluid velocity. The equation of motion of the intuder is therefore,

$$\begin{aligned}
\rho^p V_l \frac{dw_l}{dt} =& P + F_b^f + F_b + F_{seg} + F_d + F_d^f \\
=& -\rho^p V_l g \cos(\alpha) + \rho^f V_l g cos(\alpha) - \frac{V_l}{\Phi}\frac{\partial P^p}{\partial z} \\
& - V_l \left(\mathcal{F}(\mu, r) - \frac{1}{\Phi}\right)\frac{\partial P^p}{\partial z} \\
& - c\pi d_l \eta^p (w_l - w_p) - 3\pi\eta^f d_l (w_l - w_f).
\end{aligned} \tag{4.1}$$

Due to the presence of the fluid, the granular pressure gradient is reduced to $\partial P^p/\partial z = -(\rho^p - \rho^f)\Phi g\cos(\alpha)$ and the granular buoyancy force is $F_b = (\rho^p - \rho^f)V_l g\cos(\alpha)$. Therefore the sum of the fluid and granular buoyancy force compensates exactly the weight of the large intruder : $P + F_b + F_b^f = 0$. The equation of the intruder simplifies as

$$\begin{aligned}\rho^p V_l \frac{dw_l}{dt} = &- V_l\left(\mathcal{F}(\mu, r) - \frac{1}{\Phi}\right)\frac{\partial P^p}{\partial z} \\ &- c\pi d_l \eta^p (w_l - w_p) - 3\pi\eta^f d_l (w_l - w_f).\end{aligned} \tag{4.2}$$

In this equation, the forcing mechanism for the rise of the large particle is the segregation force. Note that the pressure gradient is negative (pressure increases with depth) so that the segregation force is applied in the upward direction. Both drag forces correspond to resistive forces and slow down the motion of the intruder. This equation allows one to describe the vertical evolution of an intruder in a small particle bed immersed in a fluid. The fluid is here considered passive and only acts through buoyancy and drag forces.

In order to derive the advection-diffusion model, the first step has been to adapt equation (4.2) to a collection of large particles. Following Jackson (2000), this is done by multipliying each force by the number of large particles per unit volume. This led to the derivation of a new three phase flow model for size segregation (see appendix C for the full derivation made by Hugo Rousseau). The mass and momentum conservation equations of the small particle phase are

$$\frac{\partial \Phi_s}{\partial t} + \frac{\partial \Phi_s w_s}{\partial z} = 0 \tag{4.3}$$

$$\begin{aligned}\rho^p\left[\frac{\partial \Phi_s w_s}{\partial t} + \frac{\partial \Phi_s w_s w_s}{\partial z}\right] = &- \frac{\partial p^s}{\partial z} - \Phi_s \frac{\partial p^f}{\partial z} - \Phi_s \rho^p g\cos(\alpha) + \frac{18\eta^f \Phi_s}{d_s^2}(w_f - w_s) \\ &- \frac{6c\eta^p \Phi}{d_l^2}\left(w_s - w_m\right) + \Phi_l\left(\mathcal{F}(\mu, r) - \frac{1}{\Phi}\right)\frac{\partial P^p}{\partial z}.\end{aligned} \tag{4.4}$$

Based on a dimensional analysis, Rousseau et al. (subm) compared the granular and fluid stokes numbers and showed that the vertical fluid drag force can be neglected in the bedload configuration. The equivalent ambiant granular fluid formed by the surrounding small particles is indeed much more viscous than the fluid. Then, following the same procedure as in Thornton et al. (2006), Rousseau et al. (subm) isolated the vertical velocity of small particles from the momentum equation and introduced it in the mass conservation equation to obtain the following advection-diffusion model for size segregation (see appendix C)

$$\frac{\partial \phi_s}{\partial t} + \frac{\partial}{\partial z}\left(S_r \phi_s \phi_l\right) = \frac{\partial}{\partial z}\left(D\frac{\partial \phi_s}{\partial z}\right), \tag{4.5}$$

with

$$S_r = \mathcal{F}' St^p \frac{\partial P^p}{\partial z}, \quad \text{and} \quad D = \frac{\phi_s P^p St^p}{\Phi}, \tag{4.6}$$

where $\mathcal{F}' = \mathcal{F}(\mu, r) - 1/\Phi$, $St^p = \rho^p d_l\sqrt{g d_l}/6c\eta^p$, ϕ_s is the small particle concentration and

Φ is the mixture volume fraction. Note that because the pressure gradient is negative, the advection coefficient is negative and small particles segregate downward. The advection-diffusion equation (4.5) has been made dimensionless and the same dimensionless variables as in the previous chapter have been used to derive this equation,

$$\tilde{z} = \frac{z}{d_l}, \quad \tilde{t} = t\sqrt{g/d_l}, \quad \tilde{v} = \frac{v}{\sqrt{gd_l}}, \quad \widetilde{P^p} = \frac{P^p}{\rho^p d_l g} \tag{4.7}$$

In the following, the tildes have been dropped for clarity. This segregation model bridges the gap between the particle scale forces and continuum approaches of size segregation during bedload transport. Rousseau et al. (subm) verified that in the bedload configuration and for a unidirectional granular flow, the multiphase flow model and the advection-diffusion model are equivalent, showing the consistency of the hypothesis made to derive the latter model.

Similarly to the derivation of the Thornton et al. (2006) model, it has been necessary to assume that the total volume fraction is constant, i.e. $\Phi = Const$, meaning that the granular flow is incompressible. In the quasi-static part of the bed, the volume fraction is at the random close packing $\Phi \sim \Phi_{max}$. For bidisperse bed, mixtures of particles with different sizes lead to a local increase of the volume fraction. The amount of small particles is however small compared with the number of large particles and figure 3.3b shows that this local increase can be neglected and that the volume fraction can indeed be considered constant in the quasi-static part of the bed.

The segregation coefficient $\mathcal{F}$ was observed by Guillard et al. (2016) to depend on μ (see figure 4.2) and the authors proposed the following fit on the data,

$$\mathcal{F}(\mu) = 2.4 + 0.73 \exp\left(-(\mu - \mu_c)/0.051\right), \tag{4.8}$$

where μ_c is the static friction coefficient. This fit was obtained for 2D DEM simulations in the dense regime and is therefore only valid in this flow regime, i.e. for $\mu \geq \mu_c$. This study however focuses on the quasi-static regime where $\mu < \mu_c$ and where the proposed fit can not be used. Figure 4.2 also shows that $\mathcal{F}$ only have small variations with μ and a quite large scatter of the points around the fit. For all these reasons, $\mathcal{F}$ will at first be assumed constant such that $\mathcal{F}' = \mathcal{F} - 1/\Phi_{max} = 1$.

Estimation of the advection and diffusion coefficients expressed in equation (4.6) requires the granular viscosity $\eta^p = |\tau^p_{xz}|/\dot{\gamma}^p$, appearing in the granular Stokes number, and the granular pressure P^p. Viscosity and pressure are input parameters of the segregation model, the segregation dynamics being interpreted as a response to the granular state of the bed mixture. If a continuum granular model with segregation were considered, one could describe the granular phase as a mixture coupled with this segregation model. The profiles of τ^p_{xz}, P^p and $\dot{\gamma}^p$ are the response of the mixture granular phase to the fluid forcing, and are therefore inputs of the segregation model.

In the present case, the simplified expressions of the shear stress and granular pressure are taken from the derivation made in chapter 2 (eq. (2.42) and (2.43)), assuming the same

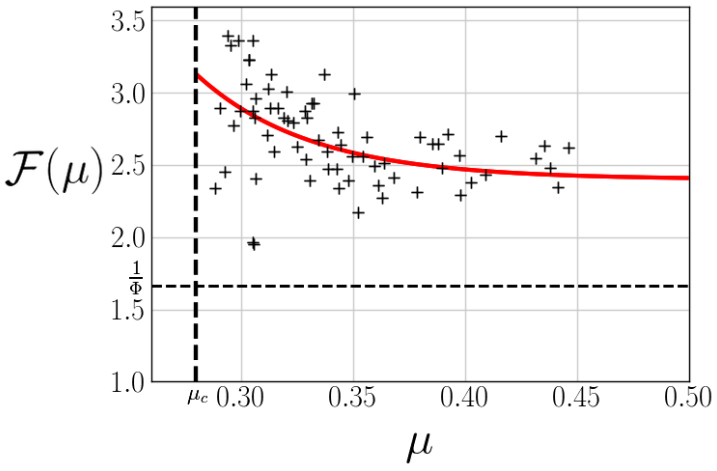

Figure 4.2: Empirical segregation function $\mathcal{F}(\mu)$ measured by Guillard et al. (2016) with 2D DEM simulations sketched in figure 1.5b. Each cross corresponds to a DEM simulation and the red continuous line correponds to proposed fit $\mathcal{F}(\mu) = 2.4 + 0.73 \exp\left(-(\mu - \mu_c)/0.051\right)$.

water depth as in the DEM simulations, corresponding to a macroscopic Shields number $\theta = \rho^f g h_w \sin(\alpha)/[(\rho_p - \rho_f) g d_l] = 0.17$. These expressions were obtained assuming an idealized step volume fraction profile in the momentum balance between fluid and granular phase. As this study focuses on the quasi-static part of the bed, they are particularly adapted to model the granular stresses in our problem, as shown in chapter 2.

The expression of the shear rate would require the resolution of the granular rheology. However, there is still no consensus on the granular rheology of the quasi-static part of the bed. The aim of the present study is to analyze size-segregation processes and modelling. Therefore, in order to avoid discrepancies due to an inaccurate description of the granular rheology and to focus on the segregation mechanisms, the shear rate $\dot{\gamma}^p$ is directly fitted on DEM simulations

$$\dot{\gamma}^p = \dot{\gamma}_0 e^{z/s_0}, \tag{4.9}$$

and plotted in figure 4.3a. The dimensionless shear stress τ^p_{xz} and granular pressure P^p are estimating from equations (2.42) and (2.43) as

$$\tau^p_{xz} = \frac{\rho^f}{\rho^p} \sin(\alpha) h_w + \left[\Phi_{max} + (1 - \Phi_{max}) \frac{\rho^f}{\rho^p}\right] \sin(\alpha)(H - z), \tag{4.10}$$

$$P^p = \Phi_{max} \frac{\rho^p - \rho^f}{\rho^p} \cos(\alpha)(H - z). \tag{4.11}$$

These two profiles are plotted against DEM data in figure 4.3b and c. They fit perfectly the DEM profiles and they will therefore be used as inputs for the advection and diffusion coefficients (4.6). Differentiating equation (4.11) with z provides the pressure gradient $\partial P^p/\partial z = -\Phi(\rho^p - \rho^f)/\rho^p cos(\alpha)$, needed in the advection coefficient. All parameters of the advection-diffusion model (4.5) can now be computed.

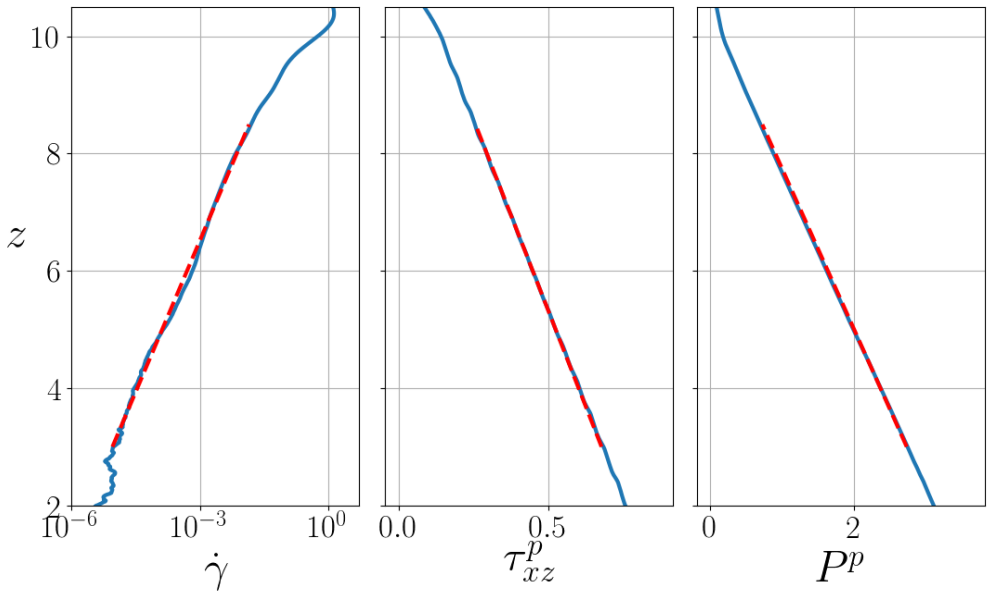

(a) (b) (c)

Figure 4.3: Shear rate (a), shear stress (b) and granular pressure (c). Full line are data from the DEM simulations and dotted lines are computed from equations (4.9), (4.10) et (4.11), with $\dot{\gamma}_0 = 1.68e-7$ and $s_0 = 0.75$

The form of the advection and diffusion coefficients are more complex than those proposed in the previous chapter for the Thornton et al. (2006) model and the new advection-diffusion model can not be solved analytically. In the next section, a numerical method for the new advection-diffusion model is proposed.

4.2 Numerical resolution strategy

In this section, the numerical resolution of the advection diffusion model (4.5) is presented. The advection and diffusion coefficients can be computed from the granular state of the mixture of small and large particles and are function of the vertical elevation z only. The small particles are transported by a non-linear advection flux noted $F_s(z, \phi_s) = S_r(z)\phi_s(1-\phi_s)$ and a diffusion flux noted $F_D = D(\phi_s, z)\partial\phi_s/\partial z$. As shown in the previous chapter, this kind of advection-diffusion problem, with a non linear advection flux can lead to formation and propagation of shocks (see figure 3.7). Therefore, a shock capturing finite volume method is adopted. This method is classical in transport equations and a general and exhaustive description can be found in reference books, such as Patankar (1980) and LeVeque (2002).

4.2.1 Formulation of the finite volume method

The spatial domain is subdivided into cells of discretization Δz and a time step Δt is considered (see figure 4.4). The average of ϕ_s in a cell centered in z_j and at time t^n is noted

$$\phi_{s_j}^n = \frac{1}{\Delta z} \int_{z_{j-1/2}}^{z_{j+1/2}} \phi_s(z', t^n)\, \mathrm{d}z'. \tag{4.12}$$

By spatial integration of equation (4.5) between $z_{j-1/2}$ and $z_{j+1/2}$, we get

$$\begin{aligned} \frac{\partial}{\partial t} \int_{z_{j-1/2}}^{z_{j+1/2}} \phi_s(z', t)\, \mathrm{d}z' = &- \Big(F_s(z_{j+1/2}, \phi_s(z_{j+1/2}, t)) - F_s(z_{j-1/2}, \phi_s(z_{j-1/2}, t))\Big) \\ &+ \Big(F_D(z_{j+1/2}, \phi_s(z_{j+1/2}, t)) - F_D(z_{j-1/2}, \phi_s(z_{j-1/2}, t))\Big) \end{aligned} \tag{4.13}$$

The time derivative is approximated by a first order Euler scheme as

$$\frac{\partial}{\partial t} \int_{z_{j-1/2}}^{z_{j+1/2}} \phi_s(z', t)\, \mathrm{d}z' = \frac{\Delta z}{\Delta t} \left(\phi_{s_j}^{n+1} - \phi_{s_j}^n\right), \tag{4.14}$$

where the expression of $\phi_{s_j}^n$ (equation (4.12)) has been introduced. We introduce the following notations, representing the mean value of the fluxes over one time step,

$$F_{s_{j-1/2}}^n = \frac{1}{\Delta t} \int_{t^n}^{t^{n+1}} F_s(z_{j-1/2}, \phi_s(z_{j-1/2}, t))\, \mathrm{d}t, \tag{4.15}$$

$$F_{D_{j-1/2}}^n = \frac{1}{\Delta t} \int_{t^n}^{t^{n+1}} F_D(z_{j-1/2}, \phi_s(z_{j-1/2}, t))\, \mathrm{d}t. \tag{4.16}$$

Assuming that the fluxes in equation (4.13) can be approximated by their temporal average values, equation (4.13) becomes

$$\phi_{s_j}^{n+1} = \phi_{s_j}^n - \frac{\Delta t}{\Delta z} \left(F_{s_{j+1/2}}^n - F_{s_{j-1/2}}^n\right) + \frac{\Delta t}{\Delta z} \left(F_{D_{j+1/2}}^n - F_{D_{j-1/2}}^n\right). \tag{4.17}$$

This equation indicates that the value of $\phi_{s_j}^n$ evolves according to the incoming and outgoing fluxes at the edges of the cell. The difficulty of the finite volume method is to estimate the value of these fluxes. Indeed, their expressions (4.15) and (4.16) are complex, and can not be computed directly. Classically, they are assumed to depend on the cell averaged value of the concentration on each edge of the cell

$$F_{s_{j+1/2}}^n = f(\phi_{s_j}^n, \phi_{s_{j+1}}^n), \tag{4.18}$$

where f is some numerical flux function. The choice of the numerical scheme corresponds to a choice of function f to estimate the flux. As the segregation and diffusion fluxes do not have a similar form, different schemes will be used for each of the flux and are detailed in the following.

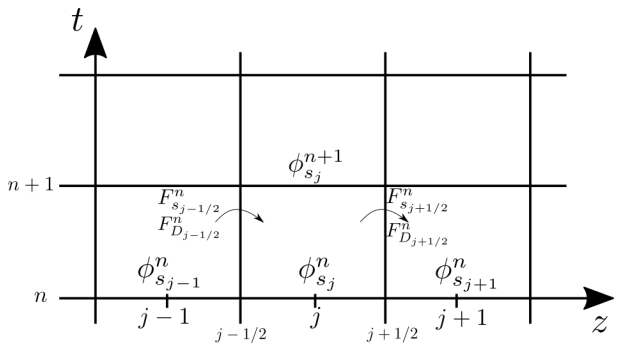

Figure 4.4: Schematic view of the finite volume grid considered for the numerical resolution of the advection-diffusion model

4.2.2 Estimation of the advective flux with Godunov scheme

This section focuses on the estimation of the advective flux. As we have seen in the previous chapter, this kind of non-linear advection coefficient can lead to the formation and propagation of shocks. For this reason, we choose a Godunov scheme that is able to capture shock dynamics. It has been derived by Godunov (1959) especially to solve discontinuous solution of hydrodynamics equations. The derivation of the Godunov fluxes are presented here for the specific quadratic advective flux considered in this model.

The aim is to estimate the advective flux. Its expression (eq. 4.15) shows that it is only necessary to estimate the evolution with time of the concentration at the edge of the cell and to integrate with time. Let us suppose that $\phi_s(z, t^n)$ is constant inside a cell equal to its mean value, i.e. $\phi_s(z, t^n) = \phi^n_{s_j}$ for $z_{j-1/2} < z < z_{j+1/2}$. This defines a piecewise constant function with discontinuity at each cell edge. The idea of the Godunov scheme is to consider each discontinuity as a Riemann problem, to solve it with the method of characteristics and to estimate the associated flux. Considering the discontinuity at $z_{j-1/2}$, the resolution of Riemann problems shows that a discontinuity can lead to shock propagation or rarefaction wave. Five different configurations are possible which are sketched in table 4.1. Cases (a) and (e) correspond to shock propagations, while cases (b), (c) and (d) correspond to rarefaction waves.

Classical analysis with the method of characteristics shows that the characteristic lines (gray lines in the figures of table 4.1) propagates at a velocity

$$c^n = \left.\frac{\partial F_s}{\partial \phi_s}\right|^n_{j-1/2} \tag{4.19}$$

$$= S_r(z_{j-1/2})(1 - 2\phi_s) \tag{4.20}$$

In addition the solution is constant on the characteristic lines equal to the value of the concentration at time t^n. Therefore, on the left of the shock or the rarefaction wave, characteristic lines propagate at a velocity $c^n = S_r(z_{j-1/2})(1 - 2\phi^n_{s_{j-1}})$ and the solution is $\phi^n_{s_{j-1}}$ along them. On the right, characteristic lines propagate at a velocity $c^n = S_r(z_{j-1/2})(1 - 2\phi^n_{s_j})$ and the solution is $\phi^n_{s_j}$. Inside the rarefaction wave, the solution

Configuration	Conditions	$F^n_{s_{j-1/2}}$
(a) 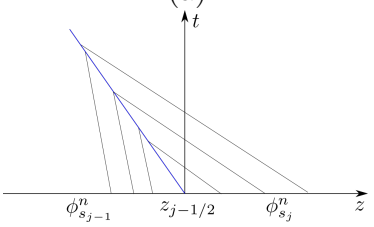	$\phi^n_{s_j} < \frac{1}{2}$ and $\phi^n_{s_{j-1}} < 1 - \phi^n_{s_j}$	$F^n_{s_{j-1/2}} = F_s(z_{j-1/2}, \phi^n_{s_j})$
(b) 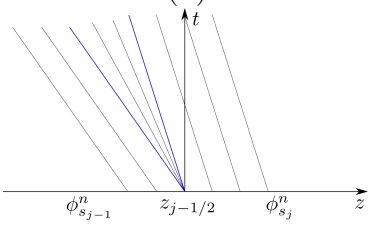	$\phi^n_{s_{j-1}} < \phi^n_{s_j} < \frac{1}{2}$	$F^n_{s_{j-1/2}} = F_s(z_{j-1/2}, \phi^n_{s_j})$
(c) 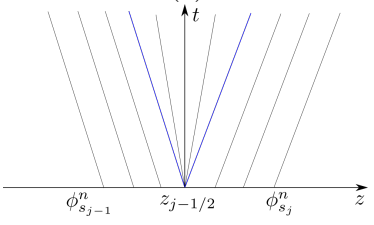	$\phi^n_{s_{j-1}} < \frac{1}{2} < \phi^n_{s_j}$	$F^n_{s_{j-1/2}} = F_s(z_{j-1/2}, \frac{1}{2})$
(d) 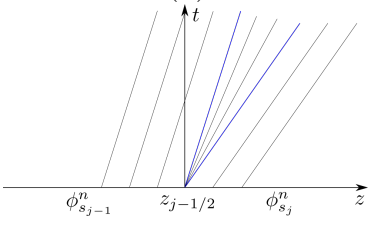	$\frac{1}{2} < \phi^n_{s_{j-1}} < \phi^n_{s_j}$	$F^n_{s_{j-1/2}} = F_s(z_{j-1/2}, \phi^n_{s_{j-1}})$
(e) 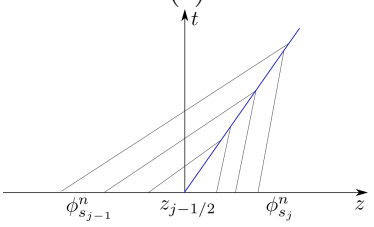	$\phi^n_{s_{j-1}} > \frac{1}{2}$ and $\phi^n_{s_j} > 1 - \phi^n_{s_{j-1}}$	$F^n_{s_{j-1/2}} = F_s(z_{j-1/2}, \phi^n_{s_{j-1}})$

Table 4.1: The five different possible configurations for the Riemann problem around discontinuity at $z_{j-1/2}$, their conditions for occurence and the corresponding Godunov flux.

is in between $\phi^n_{s_{j-1}}$ and $\phi^n_{s_j}$. To estimate the flux equation (4.15), we need the value of the concentration along $z = z_{j-1/2}$ and for all times during t^n and t^{n+1}. One can observe that, whatever the case, the solution is constant with time along the line $z = z_{j-1/2}$.

- For cases (a) and (b), $\phi_s(z_{j-1/2}, t) = \phi^n_{s_j}$, and replacing in equation (4.15), $F^n_{s_{j-1/2}} = F_s(z_{j-1/2}, \phi^n_{s_j})$.
- For cases (d) and (e), $\phi_s(z_{j-1/2}, t) = \phi^n_{s_{j-1}}$, and $F^n_{s_{j-1/2}} = F_s\left(z_{j-1/2}, \phi^n_{s_{j-1}}\right)$.
- Configuration (c) is more complex as the line $z = z_{j-1/2}$ is inside the rarefaction wave. One can note that the line $z = z_{j-1/2}$ is in fact a vertical characteristic line, so with a zero velocity. The only characteristic line with zero velocity are for $\phi_s = 1/2$. Therefore $\phi_s(z_{j-1/2}, t) = 0.5$ and $F_{s_{j-1/2}} = F_s(z_{j-1/2}, 0.5)$.

The Godunov flux can therefore take three different values. It remains to know when each case occurs. In case (a), the shock is going to the left. Its velocity is therefore negative. Applying the Rankine-Hugoniot relation, the shock velocity is given by

$$s = \frac{F_s(z_{j-1/2}, \phi^n_{s_j}) - F_s(z_{j-1/2}, \phi^n_{s_{j-1}})}{\phi^n_{s_j} - \phi^n_{s_{j-1}}} < 0, \tag{4.21}$$

which simplifies, by replacing the expression of F_s, into

$$\phi^n_{s_{j-1}} < 1 - \phi^n_{s_j}. \tag{4.22}$$

In addition, the characteristics coming from $\phi^n_{s_j}$ have a negative velocity, meaning $S_r(z_{j-1/2})(1 - 2\phi^n_{s_j}) < 0$, and remembering that $S_r(z_{j-1/2})$ is negative, yields $\phi^n_{s_j} < 0.5$. Similar reasoning can be performed for all configurations and are summurized in table 4.1. This gives a full description of all configurations and allows us to compute the Godunov flux. Noting that the conditions for case (b) are included in conditions for case (a), and that the conditions for case (d) are included in the conditions for case (e), this can be simply written as

$$F^n_{s_{j-1/2}} = \begin{cases} F_s(z_{j-1/2}, \phi^n_{s_{j-1}}), & \text{if } \phi^n_{s_{j-1}} > 1/2 \text{ and } \phi^n_{s_j} > 1 - \phi^n_{s_{j-1}}, \\ F_s(z_{j-1/2}, \frac{1}{2}), & \text{if } \phi^n_{s_{j-1}} < 1/2 < \phi^n_{s_j}, \\ F_s(z_{j-1/2}, \phi^n_{s_j}), & \text{if } \phi^n_{s_j} < 1/2 \text{ and } \phi^n_{s_{j-1}} < 1 - \phi^n_{s_j}. \end{cases} \tag{4.23}$$

Because the form of the flux F_s is quadratic in ϕ_s and has a unique minimum in $\phi_s = 1/2$, it is possible to verify that the expression of the Godunov flux (4.23) is strictly equivalent to the following expression

$$F^n_{s_{j-1/2}} = \max\left(F_s\left(z_{j-1/2}, \max(\phi^n_{s_{j-1}}, \frac{1}{2})\right), F_s(z_{j-1/2}, \min(\phi^n_{s_j}, \frac{1}{2})\right)\right), \tag{4.24}$$

which is much more simple to implement as it takes into acount all configurations in one expression.

The stability condition of the Godunov scheme has not been discussed yet. In the above analysis, we have implicitely assumed that the shocks or waves coming from one discontinuity could not meet with another one coming from a neighbouring cell. To ensure this condition, the shocks and waves should not travel more than half a cell ($\Delta z/2$) during the time Δt. The maximal wave or shock velocity is given by

$$c_n = \max_j |S_r(z_j)(1 - 2\phi^n_{s_j})|, \tag{4.25}$$

which depends on time. The stability condition has to be computed at each time step and can be written as

$$\max_j |S_r(z_j)(1 - 2\phi^n_{s_j})| \frac{\Delta t}{\Delta z} \leq \frac{1}{2}. \tag{4.26}$$

4.2.3 Estimation of the diffusive flux

The diffusion flux can be estimated more easily than the advective flux. Indeed, the diffusive flux is of the form (LeVeque, 2002) :

$$F_D(z, \phi_s) = D(\phi_s, z) \frac{\partial \phi_s}{\partial z}. \tag{4.27}$$

The diffusion coefficient depends on ϕ_s and z. As ϕ_s evolves in time, the diffusion coefficient will have to be evaluated at each time step and will be noted $D^n(z)$. Applying it in $z_{j-1/2}$ (ϕ^n_s is extrapolated linearly in $z_{j-1/2}$) and assuming that it remains constant during a time Δt, the numerical diffusion flux (4.16) is given by

$$F^n_{D_{j-1/2}} = D^n_{j-1/2} \left. \frac{\partial \phi_s}{\partial z} \right|^n_{j-1/2}. \tag{4.28}$$

The gradient of ϕ_s in $z_{j-1/2}$ can be estimated easily with the value of ϕ_s in each neighbouring cell

$$F^n_{D_{j-1/2}} = D^n_{j-1/2} \frac{\phi^n_{s_j} - \phi^n_{s_{j-1}}}{\Delta z}, \tag{4.29}$$

and the numerical advective flux is a function of $\phi^n_{s_{j-1}}$ and $\phi^n_{s_j}$. It can be interpreted as a natural physical diffusion, as the concentration goes from one cell to another at a rate proportional to the difference of concentration, and $D^n_{j-1/2}$ representing a conductivity between the two cells. The numerical scheme (4.17) becomes

$$\begin{aligned} \phi^{n+1}_{s_j} = \phi^n_{s_j} &- \frac{\Delta t}{\Delta z} \left(F^n_{s_{j+1/2}} - F^n_{s_{j-1/2}} \right) \\ &+ \frac{\Delta t}{\Delta z^2} \left(D^n_{j+1/2} \phi^n_{s_{j+1}} - (D^n_{j+1/2} + D^n_{j-1/2}) \phi^n_{s_j} + D^n_{j-1/2} \phi^n_{s_{j-1}} \right). \end{aligned} \tag{4.30}$$

The stability condition associated with the explicit diffusion scheme is

$$\max_j |D^n(z_j, \phi^n_{s_j})| \frac{\Delta t}{\Delta z^2} \leq \frac{1}{2}, \tag{4.31}$$

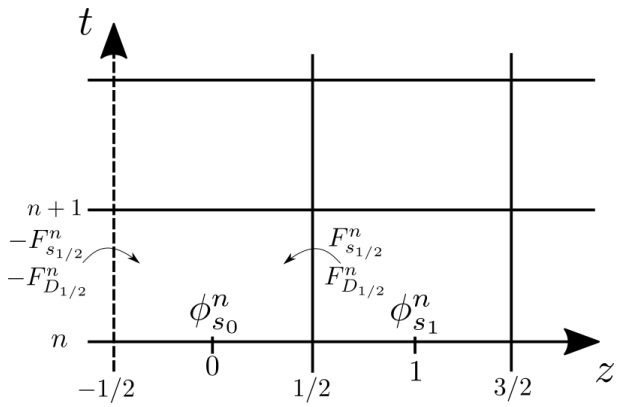

Figure 4.5: Schematic view of the first cell and the fluxes entering in the cell. The flux coming from outside the domain are imposed to be the opposites of the fluxes coming from the second cell.

and has to be evaluated at each time step.

4.2.4 Boundary condition

As for the Thornton et al. (2006) model, a no flux condition is applied at each boundary cell of the domain, i.e. in $j = 0$ and $j = J$. This boundary condition ensures that no mass is leaving the domain. Due to the finite volume construction, the first cell is delimited by $j = -1/2$ and $j = 1/2$, and the last cell by $j = J - 1/2$ and $j = J + 1/2$ (see example of the first cell in figure 4.5). The finite volume scheme (4.17) in the first cell becomes,

$$\phi^{n+1}_{s_0} = \phi^n_{s_0} - \frac{\Delta t}{\Delta z}\left(F^n_{s_{1/2}} - F^n_{s_{-1/2}}\right) + \frac{\Delta t}{\Delta z}\left(F^n_{D_{1/2}} - F^n_{D_{-1/2}}\right). \tag{4.32}$$

Equations (4.24) and (4.29) provides expressions to compute the fluxes coming from $j = 1/2$. In order to impose a no flux condition in $j = 0$, and to avoid a leak of mass at the boundary, the fluxes entering inside the domain in $j = -1/2$ are imposed to be the opposites of the fluxes coming from the second cell, i.e. $F^n_{s_{-1/2}} = -F^n_{s_{1/2}}$ and $F^n_{D_{-1/2}} = -F^n_{D_{1/2}}$. This can be interpreted as a reflective boundary for the segregation wave. Everything leaving the domain is reintroduced, and the total initial mass is conserved with time. The numerical scheme in the first cell becomes

$$\phi^{n+1}_{s_0} = \phi^n_{s_0} - 2\frac{\Delta t}{\Delta z}F^n_{s_{1/2}} + 2\frac{\Delta t}{\Delta z}F^n_{D_{1/2}}. \tag{4.33}$$

Proceeding similarly on the last cell, the numerical scheme is

$$\phi^{n+1}_{s_J} = \phi^n_{s_J} + 2\frac{\Delta t}{\Delta z}F^n_{s_{J-1/2}} - 2\frac{\Delta t}{\Delta z}F^n_{D_{J-1/2}}. \tag{4.34}$$

4.2.5 Algorithm implementation

The first step is to define a vertical grid with a discretization Δz. Based on the stability of the Godunov scheme and the diffusion scheme Δt^n is computed at each time step as

$$\Delta t^n = \frac{\Delta z}{2} \min\left(\frac{1}{\max_j |S_r^n(z_j)(1-2\phi_{s_j}^n)|}, \quad \frac{\Delta z}{\max_j |D^n(z_j, \phi_{s_j}^n)|} \right), \tag{4.35}$$

This ensures the stability of both conditions.

In order to gain computational time, the numerical resolution is done in a vectorial form. We note

$$\Phi_s^n = \begin{pmatrix} \phi_{s_J}^n \\ \vdots \\ \phi_{s_j}^n \\ \vdots \\ \phi_{s_0}^n \end{pmatrix}. \tag{4.36}$$

Following (4.30) and boundary conditions (4.33) and (4.34), the Godunov flux vector is formulated as

$$F_{godunov}^n = \begin{pmatrix} -2F_{s_{J-1/2}}^n \\ F_{s_{J-1/2}}^n - F_{s_{J-3/2}}^n \\ \vdots \\ F_{s_{3/2}}^n - F_{s_{1/2}}^n \\ 2F_{s_{1/2}}^n \end{pmatrix}, \tag{4.37}$$

where $F_{s_j}^n$ is given in equation (4.24). The diffusion flux is computed through the matricial operator M^n

$$F_{diffusion}^n = M^n \times \Phi_s^n, \tag{4.38}$$

where M^n is the diffusion matrix which has to be computed at each time step and $\times$ denotes for the matrix multiplication. Following (4.30) and boundary conditions (4.33) and (4.34), the diffusion matrix is a tridiagonal matrix and is formulated as

$$M^n = \begin{pmatrix} -2D_{J-1/2}^n & 2D_{J-1/2}^n & 0 & \dots & 0 \\ D_{J-1/2}^n & -(D_{J-1/2}^n + D_{J-3/2}^n) & D_{J-1/2}^n & 0 & \\ 0 & \ddots & \ddots & \ddots & \vdots \\ & D_{j+1/2}^n & -(D_{j+1/2}^n + D_{j-1/2}^n) & D_{j-1/2}^n & 0 \\ & & \ddots & \ddots & \ddots \\ \vdots & & & D_{3/2}^n & -(D_{3/2}^n + D_{1/2}^n) & D_{1/2}^n \\ 0 & \dots & & 0 & 2D_{1/2}^n & -2D_{1/2}^n \end{pmatrix}. \tag{4.39}$$

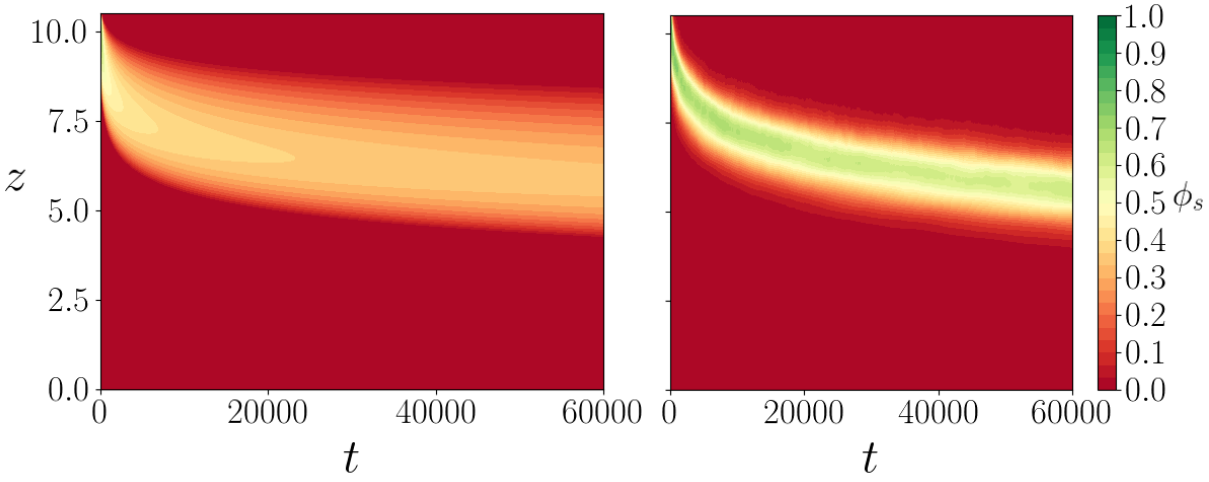

(a) (b)

Figure 4.6: Spatio temporal evolution of the small particle concentration for the case $N_s = 1.5$, computed with the advection-diffusion model (a) and obtained with the DEM simulation (b).

Finally the concentration vector at time t^{n+1} is computed as

$$\Phi_s^{n+1} = \Phi_s^n - \frac{\Delta t^n}{\Delta z} F_{godunov}^n + \frac{\Delta t^n}{\Delta z^2} M^n \times \Phi_s^n. \tag{4.40}$$

This numerical model has been implemented in python and is available at https://gitlab.com/remich/advdiffsegmodel. It is very efficient as it makes it possible to solve the segregation problem in a few minutes on a personal computer while the DEM simulations needed several weeks on our lab cluster and on several cores. It is in addition not restrictive to the advection-diffusion model presented in section 4.1. Indeed, the expression of the advection and diffusion coefficients S_r and D given in (4.6) have not been used to derive the numerical model and the code can be adapted very easily to any functional form of S_r and D.

4.3 Results and Discussion

4.3.1 Results

The advection-diffusion equation (4.5) with advection and diffusion coefficients (4.6) is solved numerically with the procedure presented in the previous section. The initial small particle concentration profile is a step of concentration

$$\phi_s(t = 0, z) = \begin{cases} 0, & z < z_i, \\ 1, & z \geq z_i, \end{cases} \tag{4.41}$$

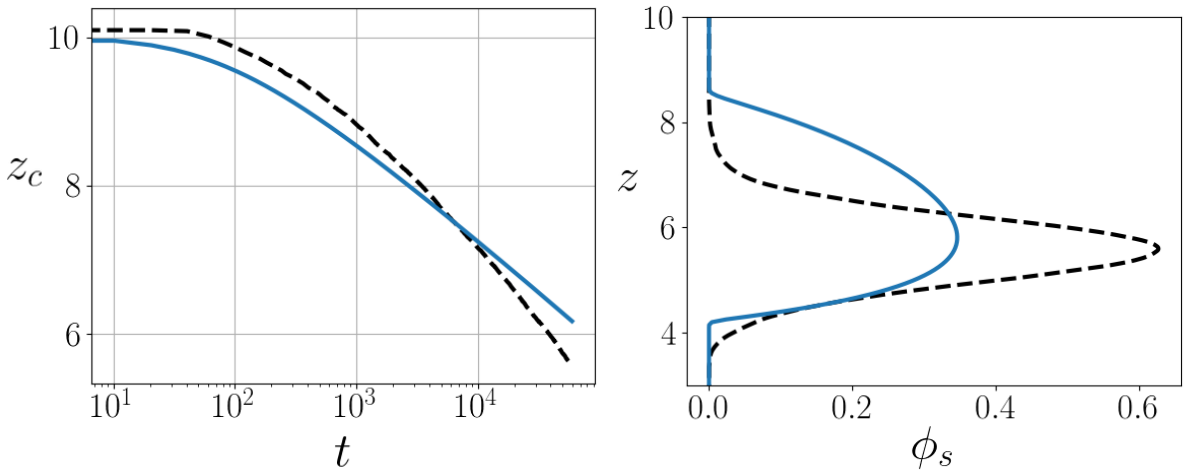

(a) (b)

Figure 4.7: Mass center evolution with time (a) and concentration profile at time $t = 60000$ (b) obtained with the advection diffusion model (full line) and with the DEM simulation (dashed line) for the case $N_s = 1.5$.

with $z_i = N_l$ and the case $N_s = 1.5$ is considered in the following. The spatio temporal evolution of the small particle concentration computed with the advection-diffusion model is plotted in figure 4.6a and compared with the DEM simulation in figure 4.6b. The advection diffusion predicts a similar dynamics as the DEM simulation with a logarithmic descent of the small particles with time. The small particles seem to percolate as a travelling wave but the profile is not self similar, i.e. the width of the wave increases while percolating.

More quantitatively, figure 4.7a compares, with the DEM simulation, the time evolution of the center of mass $z_c(t)$. After the first transient phase, the center of mass position is linear in the semi-logarithmic plot confirming the logarithmic descent with time of the small particles, as observed in the previous chapter (section 3.1.2), $z_c(t) = -a\ln(t) + b$. The absolute slope a of the logarithmic descent, characterising the segregation velocity ($dz_c/dt = -a/t$), are however different. Fitting the curves of figure 4.7a, the absolute slope is 0.59 with the advection diffusion model and 0.82 in the DEM simulation, representing a 28% error.

Figure 4.7b shows the small particle concentration at time $t = 60000$ obtained with the DEM simulation and with the advection-diffusion model. Both profiles are approximately at the same position, the bottom and maximal values are almost at the same position and the small particles are constricted in a layer. It indicates that the bottom controlled mechanism observed in the previous chapter is well reproduced by the advection diffusion model. However, the Gaussian like profile is not reproduced, the profile being wider than in the DEM simulation, with a bell shape, and as a consequence the maximum value is also smaller.

These results suggest that this new advection-diffusion model, with the physically based parametrisations for the advection and diffusion coefficients, is relevant to qualitatively

predict the segregation dynamics observed with the DEM simulations. This is quite remarkable. The particle scale forces of Guillard et al. (2016) and Tripathi and Khakhar (2011a) were obtained in completely different configurations and in 2D for the segregation force. In addition both the particle scale forces were derived in the dense regime while they are used here in the quasi-static regime. The capacity of the advection-diffusion model to reproduce qualitatively the DEM results indicates that the segregation force and the granular drag force may certainly be also valid in the quasi-static regime.

The error on the logarithmic slope and on the shape of the concentration profile indicates that some efforts are needed to improve the precision of the model. In the next section, the advection and diffusion coefficients are analysed in order to determine the origin of the discrepancies observed. Missing dependencies for the coefficients are highlighted in section 4.3.3, and new formulations for the segregation function $\mathcal{F}'$ and the drag coefficient c are proposed to better reproduce the DEM simulation.

4.3.2 Interpretation

The advection diffusion model is able to reproduce the logarithmic descent of the small particles as a layer. However the slope of the logarithmic descent in the semilog plot (figure 4.7a) is too small in comparison with the DEM simulation. To understand this difference, it is interesting to focus on the advection coefficient dependence with z. Indeed, in the previous chapter, it has been shown analytically that the logarithmic descent is a direct consequence of an exponential advection coefficient $S_r = S_{r0}e^{z/c}$ (equations (3.27) and (3.29)), and that the slope of the logarithmic descent is exactly $-c$. Therefore, the discrepency in the center of mass velocity should originate in the advection coefficient. The profile of the particle scale advection coefficient (4.6), $S_r = \mathcal{F}' St^p \partial P^p/\partial z$, is compared with the DEM advection coefficient in figure 4.8a. The semilog plot shows that the advection coefficient is exponential in both cases. Close to the top, both coefficients are quite close but differ when going deeper into the bed, and the slopes are not the same. This explains why the slope of the mass center evolution are not observed to be the same in figure 4.7a, and indicates a missing dependency with z in the advection coefficient $S_r = \mathcal{F}' St^p \partial P^p/\partial z$ to reproduce the DEM simulation.

It is however remarkable that the particle scale advection coefficient (4.6) has an exponential profile. As the pressure gradient is constant and the segregation function $\mathcal{F}'$ has been taken constant equal to 1, the only variable parameter in the expression of the advection coefficient is the viscosity η^p appearing in the Stokes number yielding $S_r \propto 1/\eta^p$. The inverse of the viscosity profile is plotted in figure 4.8c and the semi-logarithmic plot shows that it is an exponential function of z. This stems from the definition of the particle viscosity $\eta^p = |\tau^p_{xz}|/\dot{\gamma}^p$ being the ratio between the shear stress, which is linear, and the shear rate, which is exponential, resulting in an exponential profile for the inverse of the viscosity. Indeed, dividing an exponential profile by a linear function only modify the characteristic length of the exponential (modification of the exponential slope in the semi-logarithmic plot). Therefore the advection diffusion model based on the particle scale forces is able to predict the exponential form of the advection coefficient. By analogy with

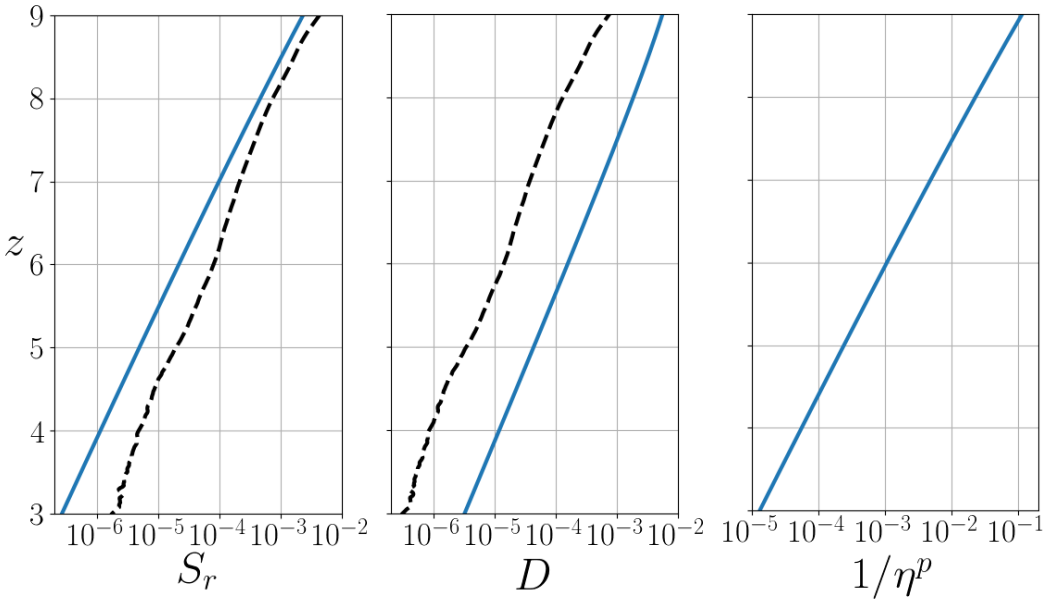

(a) (b) (c)

Figure 4.8: Case $N_s = 1.5$. Semilog plots of (a) Advection coefficient profile $S_r = \mathcal{F}' St^p \partial P^p / \partial z$ (full line) compared with the DEM advection coefficient $S_{r0} I^{0.85}$ (dashed line), (b) diffusion coefficient profile $D = \phi_s P^p St^p / \Phi$ for $\phi_s = 1$ (full line) compared with the DEM diffusion coefficient $D_0 I^{0.85}$ (dashed line) and (c) Inverse of the particle viscosity profile computed from the shear rate fit (4.9) and the shear stress expression (4.10).

hydrodynamics, the dependence of the advection coefficient to the inverse of the granular viscosity indicates that the segregation problem can be interpreted as a free fall of the small particles in a complex fluid having a spatially varying viscosity. The segregation force, through $\mathcal{F}'$, plays the role of a forcing mechanism, and the surrounding equivalent viscous fluid slows down the fall of the small particles. This highlights the fundamental role of granular viscosity in the segregation process.

In the previous chapter, the exponential profile of the advection coefficient was the result of a scaling with the inertial number (see figure 3.4b). The dependence with the granular viscosity obtained with the particle scale analysis gives clues to understand the origin of the inertial number scaling. Indeed, using the definition of the friction coefficient, the granular viscosity can be written as

$$\eta^p = \frac{\mu P^p}{\dot{\gamma}^p}. \tag{4.42}$$

The inertial number, with dimensionless variables, is

$$I = \frac{\dot{\gamma}^p}{\sqrt{P^p}}. \tag{4.43}$$

Inverting equation (4.43) and introducing it into (4.42), it comes

$$\frac{1}{\eta^p} = \frac{I}{\mu\sqrt{P^p}}. \tag{4.44}$$

The granular viscosity is therefore related to the inertial number. It means that the interpretation of size segregation, as a free fall in an ambiant viscous fluid, is not incompatible with the scaling with the inertial number highlighted by the dimensional analysis in the introduction chapter and observed in chapter 3. The advection coefficient can therefore be expressed as a function of the inertial number.

Concerning the diffusion coefficient, the previous chapter concluded that it should scale with the inertial number with the same dependency as the advection coefficient, i.e. $D = D_0 I^{0.85}$. The particle scale diffusion coefficient, $D = \phi_s P^p St^p / \Phi$, is plotted for $\phi_s = 1$ and compared with the DEM diffusion coefficient in figure 4.8b. The value is higher for the particle scale coefficient. The new advection-diffusion is therefore more diffusive than the DEM simulation explaining why the maximum value of the concentration profile is lower with the advection-diffusion model (see figure 4.7b). The curves are parallel in the semilog plot, indicating that the particle scale diffusion coefficient reproduces very well the exponential profile with the same slope as the DEM coefficient. Again this can be explained by the inverse of the particle viscosity dependency in the Stokes number which is exponential (figure 4.8). Using expression (4.44), and introducing it in the expression of the diffusion coefficient, a dependency with the inertial number can be derived

$$D = \frac{\phi_s}{\Phi} \frac{\sqrt{P^p} I}{6c\mu}. \tag{4.45}$$

Note that $\sqrt{P^p}I = \dot{\gamma}^p$, making the diffusion coefficient proportional to the shear rate which was observed by Cai et al. (2019) to control the diffusion of bidisperse mixtures. The particle scale diffusion coefficient, $D = \phi_s P^p St^p/\Phi$, also indicates a dependency with the local small particle concentration ϕ_s, that was not observed in the DEM results. The consequence of such a dependency is to increase the diffusion for large value of ϕ_s (in the middle of the concentration profile) and to reduce it in the tails. It results in the shape of concentration profile observed in figure 4.7b, very different from the DEM profile.

The present analysis has shown that the advection and diffusion coefficients (4.6), expressed as a function of particle-scale forces and without any tuning, reproduce qualitatively the advection and diffusion coefficients of the DEM simulations, in particular the exponential dependency with depth. The granular viscosity has been shown to have a fundamental role in the granular process and induces a dependency of both coefficients with the inertial number. Figure 4.8 shows that a depth dependency is missing in the advection coefficient. The diffusion coefficient is too large and contains a dependency with ϕ_s that was not observed in the DEM simulations. This ϕ_s dependency is at the origin of the discrepencies on the shape of the concentration profile.

4.3.3 Missing dependencies in particle scale forces

As mentioned previously, the advection and diffusion coefficients (4.6) have been derived from the particle scale segregation force of Guillard et al. (2016) and drag force of Tripathi and Khakhar (2013). The segregation force was obtained from $2D$ idealized DEM simulations with a simple forcing and the drag force from density segregation DEM simulations. In addition, both forces were obtained in dense flows. One can therefore expect these force formulations to miss some dependencies when considering the 3D case with complex forcing studied herein in the quasi-static regime. The purpose of this section is to use the DEM results to identify these missing dependencies and to propose new empirical parametrisations for the particle-scale forces.

The missing dependencies probably lie in the segregation function $\mathcal{F}'$ and in the drag coefficient c. Until now, both coefficients were considered constant, while Guillard et al. (2016) observed $\mathcal{F}'$ to have a slight dependency with μ and Tripathi and Khakhar (2013) suggested c to depend on the small particle concentration. Similarly to a hindrance function in a fluid flow, one expects an increase of the effective solid drag force on a particle with increasing concentration. Indeed, small particles more concentrated around a large particle should obtruct it more easily and apply a stronger drag force. This should affect the diffusion coefficient. In the following, a dependency with ϕ_s is assumed in the solid drag coefficient as well as additional dependencies with the physical parameters in the segregation function $\mathcal{F}'$ in order to correct the particle scale coefficients. These dependencies are deduced by direct identification of the particle scale advection and diffusion coefficients with the DEM results. The advection-diffusion model with these new empirical formulations is then verified to indeed reproduce the DEM simulations.

The drag coefficient is supposed to depend on the small particle concentration $c(\phi_s)$ and

$\mathcal{F}'$ is not assumed constant anymore. As shown in the previous section 4.3.2, the granular viscosity can be expressed as a function of the inertial number (eq. 4.44). Replacing in the expression of the advection and diffusion coefficients (4.6), they can also be written as a function of the inertial number

$$S_r = \frac{I\mathcal{F}'}{6c(\phi_s)\mu\sqrt{P^p}}\frac{\partial P^p}{\partial z}, \quad \text{and} \quad D = \frac{\phi_s}{\Phi_{max}}\frac{\sqrt{P^p}I}{6c(\phi_s)\mu}. \tag{4.46}$$

Focusing first on the diffusion coefficient, figure 4.8b shows that the DEM and the particle scale diffusion coefficients have the same vertical dependency. It means that, in this particular configuration,

$$\frac{\sqrt{P^p}I}{\mu} \propto I^{0.85}, \tag{4.47}$$

and fitting the curves of figure 4.8b, the ratio is estimated to $\sqrt{P^p}I/\mu I^{0.85} = C_0 = 1.13$. Comparing the diffusion coefficient 4.46 with the DEM diffusion coefficient $D = D_0 I^{0.85}$, it yields

$$\frac{\phi_s}{\Phi_{max}}\frac{C_0}{6c(\phi_s)} = D_0, \tag{4.48}$$

and isolating the drag coefficient, it follows, from the identification of the model with the DEM, a new formulation of c with a local small particle concentration dependency

$$c(\phi_s) = \frac{C_0}{6\Phi_{max}D_0}\phi_s = 31\phi_s. \tag{4.49}$$

The consequence of such a linear scaling in small particle concentration is to remove the ϕ_s dependency in the diffusion coefficient (4.46) that affects the shape of the concentration profile in figure (4.7)b. Formulation (4.49) vanishes when ϕ_s tends to zero, corresponding to the limit case where only one small particle is immersed in a bath of large particles. In such a limit case, Tripathi and Khakhar (2013) found the drag coefficient to reach a constant value $c(\phi_s \to 0) = 3$. In order to ensure a consistent formulation, the following slightly modified formulation of the drag coefficient is proposed

$$c(\phi_s) = 3 + 28\phi_s, \tag{4.50}$$

which tends to 3 when $\phi_s \to 0$ and to 31 when $\phi_s \to 1$.

Focusing now on the advection coefficient, both DEM and particle scale coefficients are identified

$$\frac{I\mathcal{F}'}{6c(\phi_s)\mu\sqrt{P^p}}\left|\frac{\partial P^p}{\partial z}\right| = S_{r0}I^{0.85}. \tag{4.51}$$

In order to correct the discrepancies of the particle scale advection coefficient (see figure 4.7a), a new expression for $\mathcal{F}'$ is desired from the DEM results. Isolating $\mathcal{F}'$ in

equation (4.51) provides a new formulation for the segregation function

$$\mathcal{F}'(\mu, P^p, \phi_s, I) = \frac{6S_{r0}c(\phi_s)\rho^p}{\Phi_{max}(\rho^p - \rho^f)}\mu\sqrt{P^p}I^{-0.15}. \tag{4.52}$$

As observed by Guillard et al. (2016), the segregation function is found here to depend on the friction coefficient. This dependency is linear in our configuration while it was more complex in Guillard et al. (2016) (eq. 4.8). Not surprisingly, when considering an ensemble of small and large particles, the segregation function is also found to depend on the small particle concentration. Additional dependencies with the granular pressure and the inertial number, which were not observed by Guillard et al. (2016), are proposed for $\mathcal{F}'$. These dependencies modify the depth dependency of the segregation function and therefore of the advection coefficient and allow reproducing the DEM results.

The proposed dependencies for the segregation function and the drag coefficient are based on fit on the DEM results and not on physical arguments. They should therefore be verified, but the present study does not permit to discuss more the proposed functional forms. However, this study allows us to draw two conclusions. First the dependence of the advection and the diffusion coefficients with the inertial number to the power 0.85 is the results of several combined effects, which all together scale with $I^{0.85}$. Second, the form proposed by Guillard et al. (2016) for $\mathcal{F}$ is not general and dependencies are missing to reproduce size segregation of an ensemble of particles in the quasi-static region.

The advection-diffusion model with the new parametrisations of the segregation function and the drag coefficient is now verified by comparison with DEM simulations. Different initial number of layers of small particles are considered ($N_s = 0.1$, 1, 1.5 and 2). The results are plotted in figure 4.9. Both the center of mass evolution with time and the concentration profile at time $t \sim 60000$ are very well reproduced by the advection diffusion model. As expected, the new parametrisations are therefore consistent with the DEM simulations. The solution with parametrisations from the literature (figure 4.7b) is also plotted in dotted line for comparison. One can observe that, with the new parametrisations, the shape of the concentration is significantly improved. As already mentioned, this is allowed by the linear dependency of the drag coefficient on the small particle concentration, which suppresses the ϕ_s dependency in the initial formulation of the diffusion coefficient (equation (4.6)).

The new parametrisations also make it possible to retrieve the travelling wave solution at constant thickness. Figure 4.10a plots the time evolution of the maximum value of the small concentration for the same simulations than in figure 4.9. For each simulation, the maximum value of ϕ_s is constant after an initial transient phase. This indicates that the shape of the concentration profile does not evolve with time and the small particles infiltrate as a self similar travelling wave with constant thickness. As demonstrated in the previous chapter, this means that the Peclet number, defined as the ratio between the advection and the diffusion coefficient, is constant. Indeed, both coefficients, with new parametrisations, are plotted in figure 4.10b. Both coefficients have the same vertical dependency and the Peclet $Pe = Sr/D$ is therefore almost constant with z around $Pe = 5$

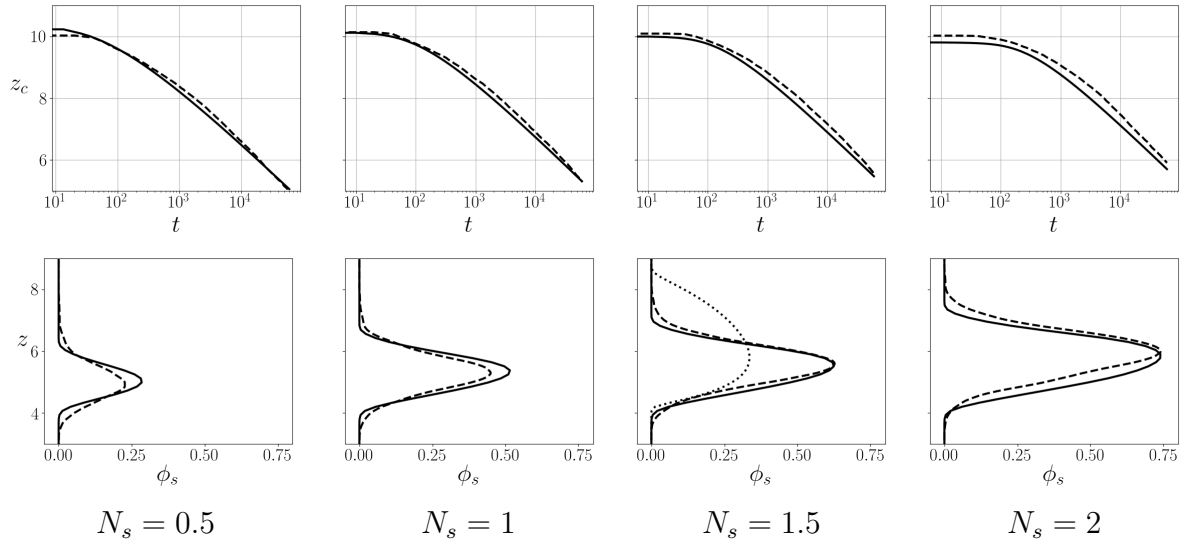

Figure 4.9: Comparison, for different numbers of layers of small particles, between the DEM simulations (dashed line) and the advection diffusion solution (full line) with new formulations of the segregation function (4.52) and drag coefficient (4.49). Upper panel corresponds to the time evolution of the small particles mass center and lower panel to the concentration profile at time $t \sim 60000$. For the case $N_s = 1.5$, the concentration profile without parametrisation is plotted for comparison (dotted line).

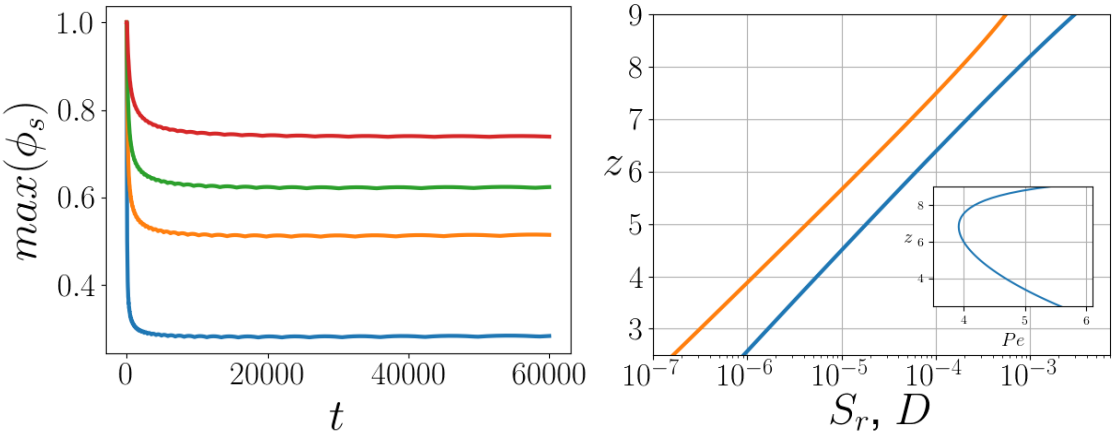

(a) (b)

Figure 4.10: (a) Time evolution of the maximum value of the small particle concentration for different value of N_s. $N_s = 0.5$: blue, $N_s = 1$: orange, $N_s = 1.5$: green and $N_s = 2$: red. (b) Advection and diffusion profiles with the new parametrisations.

(see inset of figure 4.10b). This is not surprizing. Indeed, the new parametrisations of the segregation function $\mathcal{F}'$ and the drag coefficients c have been computed by indentification with the DEM coefficients, which have both the same vertical dependency. In the previous chapter, the value of the Peclet number was observed to vary with the number of small particles N_s and this was interpreted as a global manisfestation of a ϕ_s dependency in the diffusion coefficient. The new parametrisation of the diffusion coefficient does not have a ϕ_s dependency anymore and therefore does not predict the increase of the Peclet number with N_s. This would require more work on diffusion mechanisms in bidisperse mixtures in order to determine the origin of this dependency of the diffusion coefficient with ϕ_s.

4.3.4 Influence of the size ratio

The influence of the size ratio has been studied in the previous chapter with DEM simulations. The segregation velocity was observed to increase strongly with the size ratio and a best fit on the results suggested a dependency $\mathcal{G}_1(r) = 0.45\left(e^{(r-1)/0.63} - 1\right)$ for the advection coefficient, where $r = d_l/d_s$ is the size ratio. In their work, Guillard et al. (2016) observed the segregation function $\mathcal{F}'$ to depend on the size ratio. The $\mathcal{G}_1(r)$ dependency is therefore introduced in the advection-diffusion model through the segregation function as

$$\mathcal{F}'(\mu, P^p, \phi_s, I, r) = \mathcal{G}_1(r)\frac{6S_{r0}c(\phi_s)\rho^p}{\Phi(\rho^p - \rho^f)}\mu\sqrt{P^p}I^{-0.15}. \tag{4.53}$$

This new parametrisation is tested against the DEM simulations for the size ratio $r = 1.25$, 1.5, 1.75, 2 and 2.25 in figure 4.11. The segregation dynamics is very well reproduced by the advection diffusion models. In each case, the predicted center of mass temporal evolution is almost superimposed with the DEM result. The predicted concentration profiles at time $t = 60000$ are also at the same position as the DEM profiles. Adding $\mathcal{G}_1(r)$ in the segregation function allows the model to reproduce the increased segregation velocity with the size ratio. This can be observed, at time $t = 60000$, by the lower position of the concentration profiles for higher size ratios. Focusing on the shape of the concentration profile, the width and maximum value are well reproduced for low size ratios ($r = 1.25$, 1.5) but more discrepancies are observed for larger size ratio ($r = 2$, 2.25). In these cases, the width of the concentration profile is too small and the maximum value too high, compared with the DEM simulation, indicating that diffusion is too weak in the advection-diffusion model. This means that the diffusion coefficient should probably contain a size ratio dependency. This would need more work on diffusion of bidisperse mixtures but it seems reasonable that diffusion should depend on the size ratio.

While Guillard et al. (2016) observed $\mathcal{F}'$ to reach a maximum for $r = 2$, the function $\mathcal{G}_1$ measured on DEM simulations increases exponentially with r and does not exhibit such a maximum. Two possible origins of this difference are put forward. As already discussed in the previous chapter (section 3.1.5) there exists an asymmetry in the segregation process when considering the rise of a large intruder or the infiltration of a small particle (Van der Vaart et al., 2015). This asymmetry is here highlighted when comparing the size ratio dependency in $\mathcal{F}'$ observed by Guillard et al. (2016) and the $\mathcal{G}_1(r)$ dependency measured

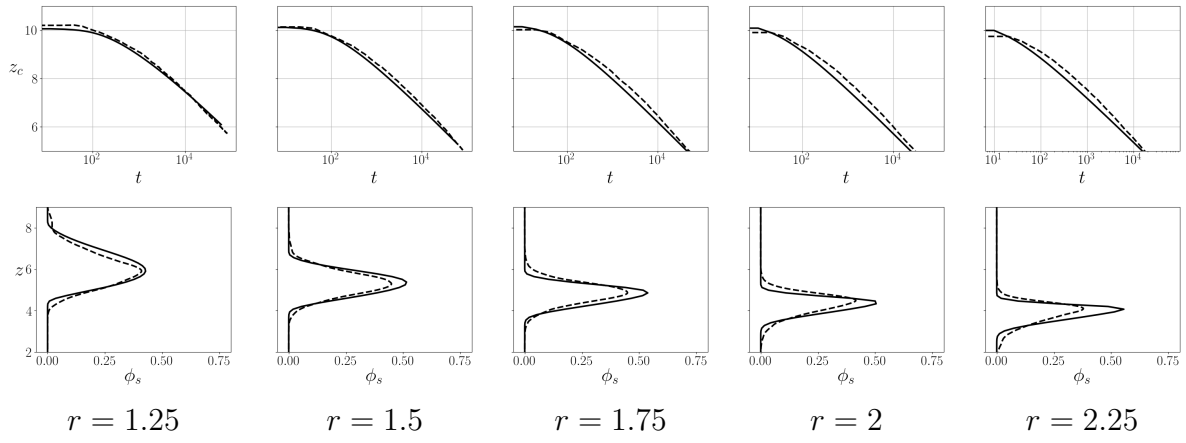

Figure 4.11: Comparison,for different values of the size ratio, between the DEM simulations (dashed line) and advection diffusion solution (full line) with new formulations of the segregation function (4.52) and drag coefficient (4.49) and for $N_s = 1$. Upper panel corresponds to the time evolution of the small particles mass center and lower panel to the concentration profile at time $t \sim 60000$.

in this study based on the DEM results.

Another possibility is that the measured dependency $\mathcal{G}_1(r)$ would be a combination of different size ratio dependencies. The analysis above indicates that the diffusion coefficient $D = \phi_s P^p St^p / \Phi$ depends on the size ratio. This dependency may lie in the drag coefficient, with a size ratio dependency in the Stokes number $St^p(r)$. The advection coefficient $S_r = \mathcal{F}' S_t^p \partial P^p / \partial z$ contains the product of the segregation function $\mathcal{F}'$ and the Stokes number S_t^p. The measured $\mathcal{G}_1$ functional form could therefore be the combination of these two dependencies. This is however purely speculative and further work is needed to describe these potential effects.

4.4 Conclusion

The DEM results obtained in the previous chapter have been analysed in the framework of the new advection-diffusion model proposed by *.Theoriginalityofthismodelisthatitisderivedfromparticl basedparametrisationsfortheadvectionanddiffusioncoefficients.Thisderivationmakesitpossibletoid*

A numerical method has been presented to solve the model. It can be used for any formulation of the advection and diffusion coefficients. Forcing only with rheological properties of the mixture bed (shear rate and bed stresses) and without any tuning, the model reproduces the main properties of the DEM results, in particular the logarithmic descent of the small particle layer with time. It is demonstrated that the granular viscosity plays a major role in the segregation process and implies a dependency of both coefficients with the inertial number as observed in the previous chapter. Using the DEM results, improved parametrisations for the advection and diffusion coefficients have been proposed. The segregation function of Guillard et al. (2016) is shown to depend on small particle concentration, pressure, inertial number and size ratio and the drag coefficient

of Tripathi and Khakhar (2013) to depend on the small particle concentration and size ratio.

This work represents a major step in the upscaling process toward continuum modelling of grain size sorting during bedload transport. The macroscopic segregation mechanisms observed in the previous chapter have been explained by interactions at the particle scale. The derivation of the model is not restricted to the current bedload configuration and could be applied to other bidisperse granular flow regimes and configurations.

Some additional dependencies have been proposed in the parameters of the particle scale forces in order to reproduce quantitatively the DEM results in the quasi-static regime. These dependencies should now be verified at the particle scale. Reverting to the study of a large intruder in a small particle bed, the segregation force and drag force should be isolated in order to study the dependencies of the segregation function $\mathcal{F}'$ and of the drag coefficient c. It would be interesting to verify these dependencies in the quasi-static regime, in the dense regime, and in other types of flow (Bagnold flow, dry heap flow...).

Chapter 5

Sediment mobility of bi-disperse mixtures during bedload transport

In previous chapters, the mechanisms responsible for size segregation and its modelling have been studied in quasi-static granular flows. This allowed us to characterise the parameters controlling the segregation velocity and to better understand the physical mechanisms at stake. Until here, the number of small particles were assumed to be sufficiently small to infiltrate the large particle bed without modification of the bulk properties. However, in practice, sediment beds are often found already segregated and the discussion in introduction shows that the presence of smaller particles may strongly influence the bed mobility. In this chapter, we therefore investigate the consequences of size segregation on sediment transport fluxes. As most of the transport is located in the bedload layer, the results presented in this chapter mainly focus on the dense granular flow regime. This work has led to the publication of a scientific paper in the journal *Physical Review Fluid* (Chassagne et al., 2020a).

In most classical bedload transport laws, the definitions of the Shields number and Einstein parameter are based on the surface composition of the bed, via the median diameter d_{50} or d_{84} (84% of grains are smaller than d_{84}), and do not account for the depth structure of the grain size distribution. The literature review presented in the introduction however highlights the influence of the depth structure on bed mobility. Indeed, in many studies, the presence of small particles at the base are observed to lubricate and increase the mobility of the whole flow. In bedload transport, segregated small particles, buried below the bed surface are therefore expected to affect the mobility of the overlying large particles. However, there is still no clear understanding of the responsible mechanisms for this enhanced mobility.

In this chapter, the mobility of bidispersed segregated beds is studied from a granular perspective, considering coupled fluid-DEM simulations of turbulent bedload transport. The analysis will be performed in the framework of the $\mu(I)$ rheology (GDR MiDi, 2004; Jop et al., 2006; Forterre and Pouliquen, 2008) extended for the bedload configuration by Maurin et al. (2016) as described in section 2.2.3.

The numerical setup is presented in section 5.1. The bed mobility is explored in section 5.2. Results are analysed within the $\mu(I)$ rheology framework in section 5.3 and the increased mobility is shown to be directly related to rheological consequences. Based on rheological arguments, a simple predictive model for the additional transport is derived and compared with DEM simulations in section 5.4. Finally the results are discussed in section 5.5.

5.1 Numerical setup

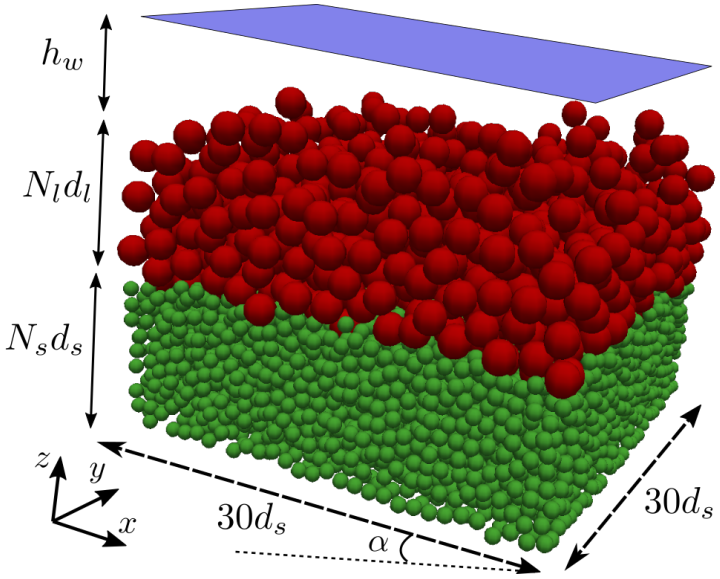

Figure 5.1: A typical numerical setup. Initially N_l layers of large particles ($d_l = 6$ mm) are deposited by gravity on N_s layers of small particles ($d_s = 3$ mm). The fluid of depth h_w flows by gravity due to the slope α and entrains particles.

The numerical setup is presented on figure 5.1. It is close to the one presented in chapter 3 but the initial state is already segregated with the large particles on top of the small ones. Initially, N_s layers of small particles of diameter $d_s = 3$ mm and N_l layers of large particles of diameter $d_l = 6$ mm are deposited by gravity over a rough fixed bed made of small particles. The height of the bed at rest is thus defined by $H = N_s d_s + N_l d_l$. The size of the 3-D domain is $30d_s \times 30d_s$ in the horizontal plane in order to have converged average values (Maurin et al., 2015) and is periodic in the streamwise and spanwise direction. The bed slope is fixed to 10% ($\alpha = 5.7°$), representative of mountain streams. As this study mainly focuses on cases where the bed surface is composed of only large particles, the Shields number definition is based on the large particle diameter as $\theta = \tau_f / ((\rho^p - \rho^f) g d_l)$, where $\tau_f = \rho^f g h_w sin(\alpha)$ is the fluid bed shear stress, with h_w the water depth. Only the macroscopic definition of the Shields number is used in this chapter (see discussion about the Shields number definition in section 2.2). Simulations were performed for Shields numbers ranging from 0.1 to 1, i.e. from a few isolated particles transported at the bed

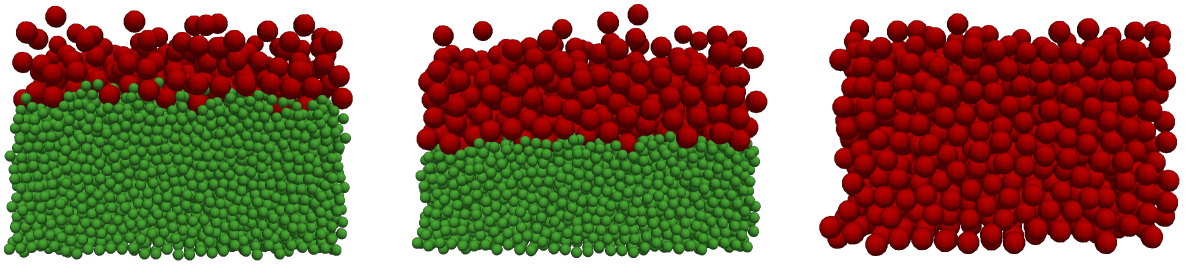

(a) (b) (c)

Figure 5.2: Illustration of some considered configurations. (a) $N_l = 2$, (b) $N_l = 4$, (c) monidisperse case

surface to a ten grain thick mobile layer. For each value of the Shields number, several configurations were considered with a varying number of layers of large particles $N_l = 1$, 2, 3 and 4 which will be compared with a monodisperse large particle configuration considered as a reference case (see figure 5.2). In each case N_s varies in order to keep the bed height H constant equal to $H = 8.5d_l$ for $\theta \leq 0.5$, $H = 10.5d_l$ for $0.5 < \theta \leq 0.7$ and $H = 16.5d_l$ for larger Shields numbers. This increase in the bed thickness is made in order to ensure an erodible bed bottom boundary condition. As we focus on transport, in this chapter, the origin of the vertical axis is set at the top of the particle bed at rest. The interface position, describing the transition between large and small particles, is therefore defined geometrically as $z_i = -N_l d_l$.

At the beginning of each simulation, the fluid flows by gravity and sets particles into motion. After approximately 20 seconds, a dynamical equilibrium is achieved between the fluid flow and the transport of sediment. The results are then time-averaged over a 280s time period to ensure converged results. A mixed layer forms at the interface between small and large particles resulting from an equilibrium between diffusion and size segregation. The present study focuses on the relation between the fluid forcing and sediment transport once the steady state is achieved. Similar to the Shields number, the Einstein parameter is based on the large particle diameter as $Q_s^* = Q_s / \left((\rho^p/\rho^f - 1)g d_l^3\right)^{0.5}$, where $Q_s = \int \Phi v_x^p dz$ is the transport rate per unit width in m^2/s, and v_x^p is the bulk streamwise velocity. The horizontal averaged volume fraction of small (resp. large) particles is defined as Φ_s (resp. Φ_l). By definition, the two volume fractions sum to Φ the total granular volume fraction,

$$\Phi_s + \Phi_l = \Phi. \tag{5.1}$$

5.2 Enhanced mobility due to bidispersity

In figure 5.3a is plotted the steady state dimensionless solid transport rate as a function of the Shields number. In all configurations, the dimensionless transport rate increases with the Shields number. The transport rate is remarkably stronger in all bidisperse configurations with respect to the monodisperse case, evidencing enhanced particle mobility. Figure 5.3b shows the bidisperse transport relative to monodisperse configurations,

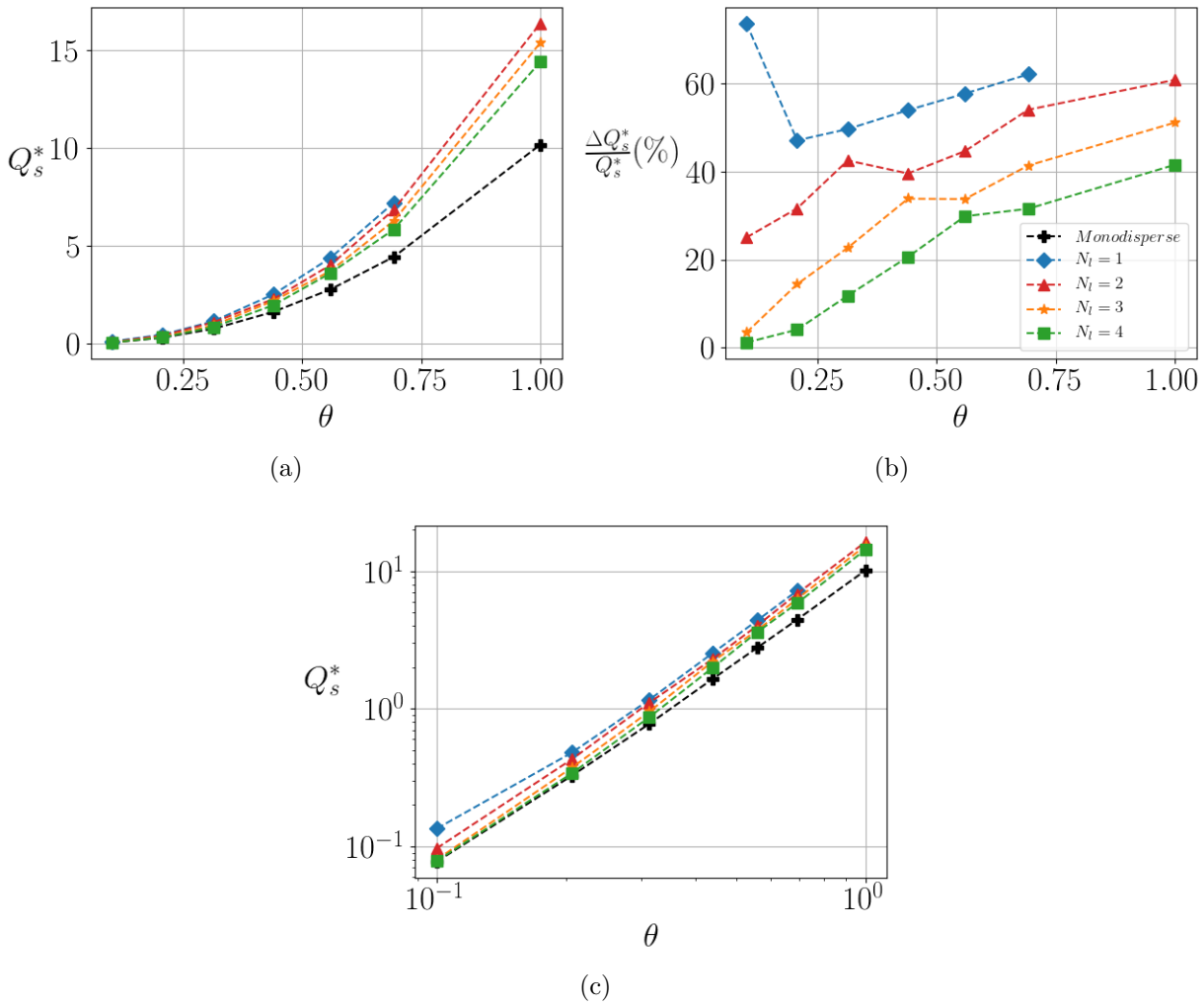

Figure 5.3: (a) Solid transport rate as a function of the Shields number for all simulations. (b) Increased transport rate in percentage compared with the monodisperse configuration. (c) Log-log plot of the Solid transport rate as a function of the Shields number.

increasing up to 50%. The increase of transport is almost linear with the Shields number and is stronger when the number of layers of large particles N_l is small. Indeed, for a lower N_l, small particles are closer to the surface (see figure 5.2) and are more likely to influence transport. This indicates that the depth of the interface between large and small particles, z_i, plays a role in the transport efficiency. At low Shields numbers and for $N_l = 4$, almost no increase of transport is observed. In that case, the interface position is too deep to affect the bed mobility, and the bidisperse bed behaves as if it were monodisperse. Overall, without modification of the fluid forcing, a substantial increase of transport is observed just by changing the particle size in the bed depth profile.

Figure 5.3c shows the dimensionless transport rate as a function of the Shields number in a log-log plot (same data as in figure 5.3a). The linearity of the curves shows that a power law relates both parameters in all configurations. The value of the exponent is not

sensitive to the bed composition, consistent with experimental observations of Houssais and Lajeunesse (2012) of bimodal beds, and a best fit on the curves yields a mean exponent of 2.20. The value of the prefactor is however higher in bidisperse configurations than in the monodisperse one, indicating an increase of transport in these configurations. The measured value of the exponent is larger than the 3/2 exponent in classical transport laws (Meyer-Peter and Müller, 1948; Einstein, 1950). This is however consistent with other simulations of intense bedload transport (Maurin et al., 2018; Chauchat, 2018) measuring an exponent around two. It is also consistent with the semi-empirical transport law proposed by Pähtz and Durán (2020), which unifies different transport regimes, predicting a 3/2 exponent for low transport and a 2 exponent for intense transport.

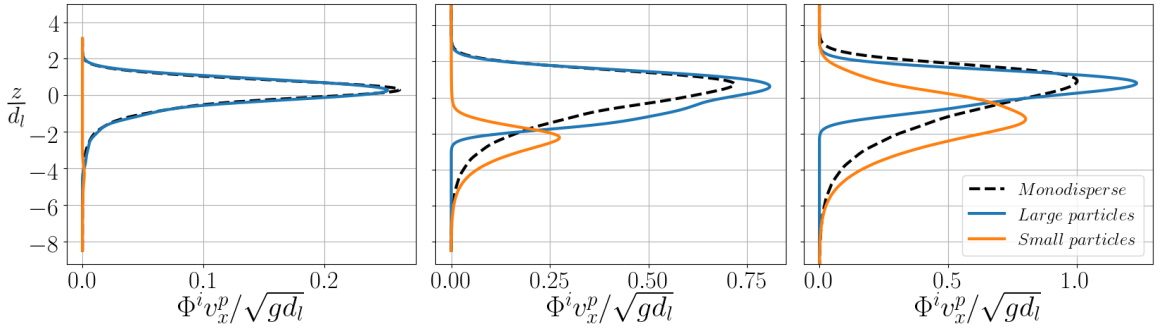

(a) $\theta \sim 0.2$, $N_l = 4$ (b) $\theta \sim 0.45$, $N_l = 2$ (c) $\theta \sim 0.55$, $N_l = 1$

Figure 5.4: Transport profiles of each class of particles for different configurations and Shields numbers. The transport profile of the large particles in the monodisperse case for the same Shields number is also plotted for comparison.

To expand the transport description, the local transport rate of each class of particle is defined as $q_s^i(z) = \Phi_i(z)v_x^p(z)$, where $\Phi_i(z)$ is the volume fraction of particle class $i = l, s$. Figure 5.4 shows the local transport rate depth profile of each class of particles for different typical configurations. The transport rate of large particles in the monodisperse case is also plotted in black dashed line for comparison. For $\theta \sim 0.2$ and $N_l = 4$ (figure 5.4a), almost no increase of transport ($\sim 4\%$) is observed, and the small particles are barely transported. Increasing the Shields number, figure 5.4b shows that the small particles are transported but remain buried in the bed. When comparing the transport rate profile of small particles with the monodisperse configuration (dashed line), the small particle transport is higher than the large one at the same depth. The same observation is true for the overlying large particles. The total transport, being the sum of both the small and large particle transport, is therefore much higher in the bidisperse case than in the monodisperse case. For $\theta \sim 0.55$ and $N_l = 1$ (figure 5.4c) the transport of small particles is even stronger and small particles are present up to the bed surface, while they remained buried in the previous configuration (figure 5.4b). It is therefore possible to draw two main conclusions. First, the observed increase of transport is a direct consequence of the mobility of the small particles. Second, even the large particle transport is significantly higher than in the monodisperse case.

Two types of phenomenology are observed in the results. On the one hand small and large particles remain well separated, with small particles buried deep in the bed (figure 5.4a, b). On the other hand, small and large particles are mixed at the surface (figure 5.4c). The width of the transition between small and large particles depends on the relative importance of segregation over diffusion, the ratio of which has been defined as the Peclet number P_e in section 3. If diffusion is strong enough compared to segregation, small buried particles can reach the surface. To characterise the surface state, the surface diameter is computed as the mean particle diameter above $z = 0$ as

$$d_{surf} = \frac{\int_0^{+\infty} \Phi_s(z) d_s + \Phi_l(z) d_l dz}{\int_0^{+\infty} \Phi_s(z) + \Phi_l(z) dz}. \tag{5.2}$$

The non-dimensional surface diameter is set between 0 (only small particles at surface) and 1 (only large particles) with the following transformation

$$\bar{d}_{surf} = \frac{d_{surf} - d_s}{d_l - d_s}. \tag{5.3}$$

Figure 5.5 shows in scatter plot the value of the surface diameter as a function of the Shields number and the number of layers of large particles. The domain is clearly separated into two parts deliminated by the dashed line. Above the dashed line, the bed surface is only composed of large particles while below it is composed of a mixture of both small and large particles. For a given value N_l, there exists a transition Shields number $\theta_t(N_l)$ which separates a monodisperse bed surface from a bidisperse one. For $\theta < \theta_t$, diffusion is weak compared to segregation, while for $\theta > \theta_t$ it is strong enough to move small particles up to the bed surface. This therefore indicates that the Peclet number P_e depends on the Shields number. In addition θ_t increases with N_l. Indeed, when N_l increases, the transition depth z_i between small and large particles is deeper in the bed and diffusion needs to be even stronger for the small particles to reach the surface. For $N_l = 4$ the surface is always composed of large particles. There is no doubt that increasing again the Shields number will eventually bring small particles at the surface. Two simulations for $N_l = 0.5$ have also been plotted for illustration. By definition in these cases, the bed surface is necessarily composed of a mixture of large and small particles.

In cases where the surface is composed of a mixture of small and large particles (below the dashed line), the increased transport can be attributed to a fluid effect. Indeed, at constant fluid shear stress, the ratio between the drag force contribution and the buoyant weight is inversely proportional to the diameter, so that the transport rate is *a priori* higher for a mixture surface state. In cases where the small and large particles are well separated (above the dashed line), the increased transport rate cannot be attributed to a fluid effect. Indeed, it has been shown in section 2.2.4 that for $z \leq 0$ the fluid shear stress was already completely transmitted to the granular phase. The interface depth between large and small particles being always below $z = 0$, the increased transport is necessarily due to a granular process. In the next section, the study focuses only on the configurations where small and large particles are well separated and where the bed surface is composed only of large particles. The granular process responsible for the increase of mobility is

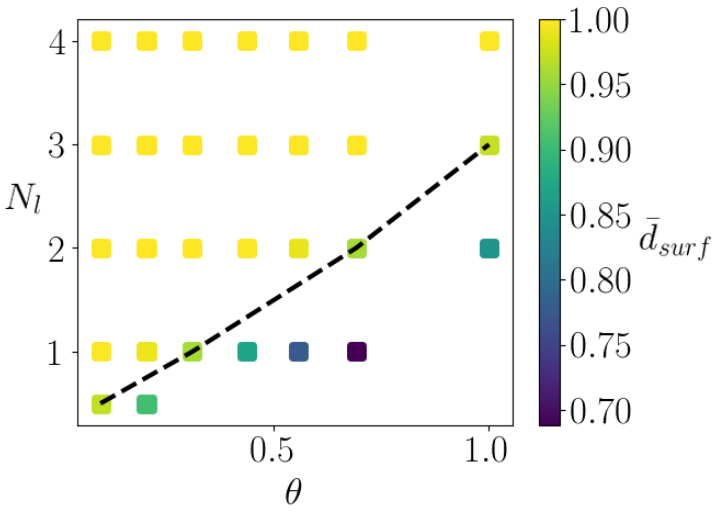

Figure 5.5: Mean surface diameter as a function of the Shields number and the large particle number of layers. The dashed line shows the transition between a large particle surface state and a mixture surface state.

investigated through a mechanical analysis of the granular bed properties.

5.3 Interpretation as a granular process

The granular stress tensor σ^p can be computed from the DEM. The procedure has been described in section 2.1.4 and it was demonstrated that in this configuration, the granular stress can be described by only two scalar parameters, which are the granular pressure $P^p = \sigma^p_{zz}$ and the shear stress $\tau^p_{xz} = \sigma^p_{xz}$. For readability, the shear stress will be noted τ^p in the following.

Figure 5.6a compares, for $\theta \sim 0.45$, the monodisperse and the bidisperse ($N_l = 2$) components of the stress tensor. The pressure and the shear stress exhibit the same behavior in the monodisperse and bidisperse configurations. For the same forcing, the response of the bed in terms of granular stresses is therefore the same whatever the constitution of the bed. However, the transport profiles (figure 5.4b) show that the bidisperse bed is more mobile than the monodisperse one. This means that the dynamical response is dependent on the bed composition. This is analysed within the framework of the $\mu(I)$ rheology, relating the friction coefficient $\mu = \tau^p/P^p$ to the inertial number I. The diameter to consider in the expression of the inertial number (2.29) is the local volume-averaged diameter (Rognon et al., 2007; Tripathi and Khakhar, 2011b) $d = \phi_s d_s + \phi_l d_l$ (which simplifies to $d = d_l$ in the monodisperse case). Following GDR MiDi (2004), the rheology of dense granular flows can be seen as follows. If $\mu \leq \mu_c$, where μ_c is the static friction coefficient, no motion is observed and $I = 0$. If $\mu > \mu_c$, there exists a one to one correspondence between the friction cofficient μ and the inertial number I.

The friction coefficient is plotted in figure 5.6b and, as expected from the similarity

of the granular stress profiles (figure 5.6a), it is the same in the bidisperse and the monodisperse configuration. As a consequence, the inertial number profiles should be the same in both configurations and that is indeed the case as observed in figure 5.6c. The dashed line (----), defines a depth z_1 such that $\mu(z_1) = \mu_c$, the theoretical transition between static and dense granular flows. The dashed-dotted line (– · –) shows the interface depth z_i between small and large particles.

Figure 5.6d shows the bulk particle velocity for both configurations. For $\mu < \mu_c$ or equivalently $z < z_1$, the inertial number and the velocity are indeed small but not exactly zero. This is due to non-local effects, that the $\mu(I)$ rheology is not able to capture (Kamrin and Koval, 2012; Bouzid et al., 2013). It corresponds to a quasi-static flow, or creeping regime, studied in chapter 3, in which the velocity is exponentially decreasing into the bed. In order to understand the increased mobility in the bidisperse configuration, the quasi-static regime has a negligible impact in terms of transport and is not considered in this study. For $z > z_1$, as the friction coefficient is similar in both configurations (see figure 5.6b), the inertial number is also supposed to be the same

$$I_b = I_m, \tag{5.4}$$

where subscript b (resp. m) denotes the bidisperse (resp. monodisperse) configuration. For $z_1 < z < z_i$, the particle diameter in the bidisperse simulation is $d_b \sim d_s$, and $d_m = d_l$ for the monodispserse case. Equation 5.4 becomes

$$\frac{d_s \dot{\gamma}_b}{\sqrt{P^p/\rho^p}} \sim \frac{d_l \dot{\gamma}_m}{\sqrt{P^p/\rho^p}}. \tag{5.5}$$

The granular pressure being the same in both configurations (see figure 5.6a), it gives

$$\dot{\gamma}_b \sim \frac{d_l}{d_s} \dot{\gamma}_m. \tag{5.6}$$

Integrating equation 5.6 from z_1 to $z \leq z_i$, and assuming that the velocities are zero in z_1, yields

$$v_b^p(z) \sim \frac{d_l}{d_s} v_m^p(z), \tag{5.7}$$

and therefore the velocity is higher in the bidisperse case than in the monodisperse case. Figure 5.6d shows indeed that, for $z_1 \leq z \leq z_i$ (between the two dashed lines), the velocity is higher in the bidisperse configuration than in the monodisperse one. It means that for the same granular stress state, small particles are transported more easily than larger particles. This is a direct consequence of the $\mu(I)$ rheology.

For $z > z_i$, the particle diameter is d_l in both configurations and equation (5.5) simplifies to

$$\dot{\gamma}_b \sim \dot{\gamma}_m, \tag{5.8}$$

and by integration from depth z_i to z,

$$v_b^p(z) \sim v_m^p(z) + (v_b^p(z_i) - v_m^p(z_i)) \sim v_m^p(z) + \Delta v, \tag{5.9}$$

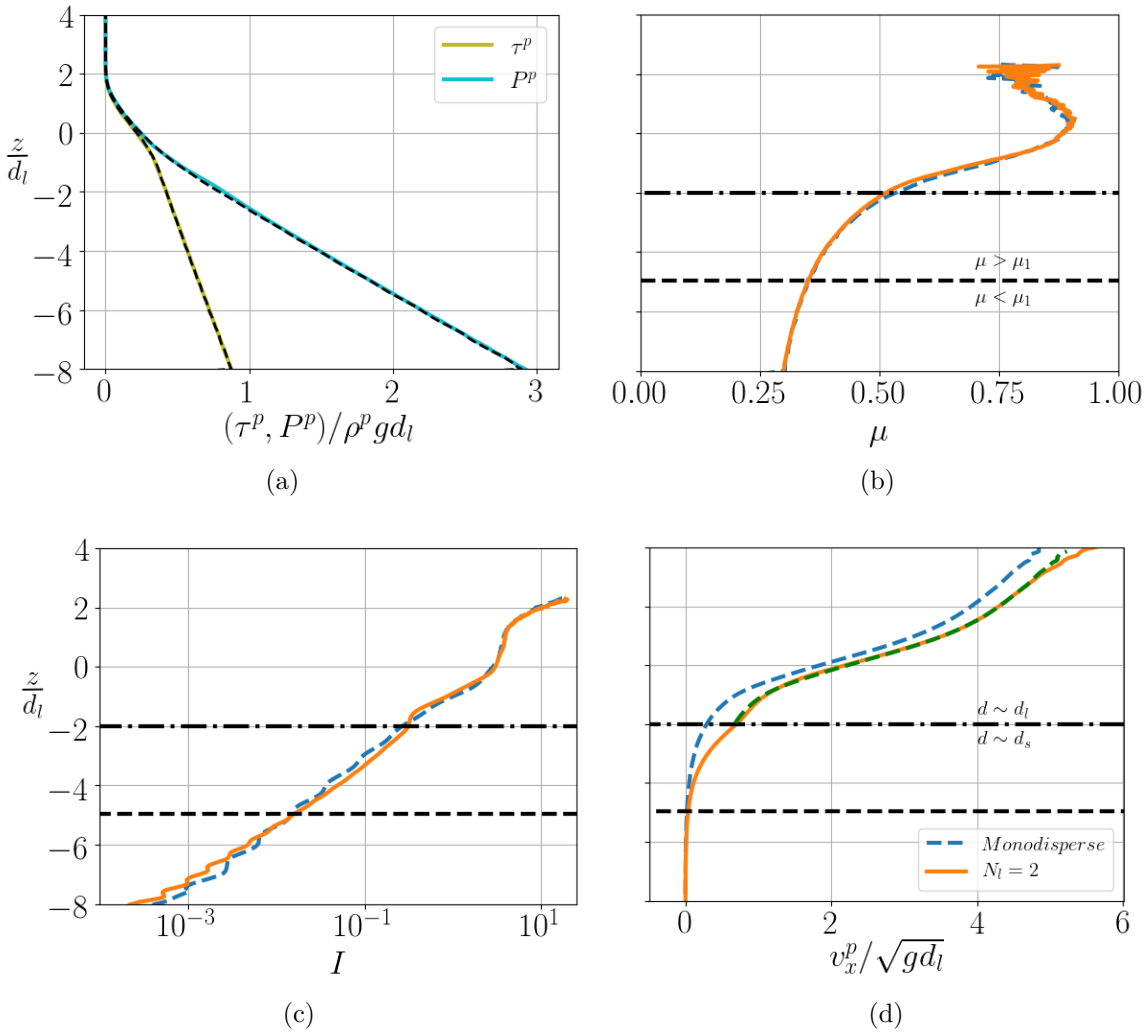

Figure 5.6: Comparison of the monodisperse (dotted line) and the bidisperse $N_l = 2$ (full line) configuration for $\theta \sim 0.45$. (a) Pressure and shear stress profiles, (b) friction coefficient profiles, (c) inertial number profiles and (d) velocity profiles. The dotted green line corresponds to a translation of $\Delta v = 0.383\sqrt{g d_l}$ of the monodisperse velocity profile (blue dotted line). The horizontal line (----) separates the quasi-static regime from the flowing regime. The horizontal line (– · –) shows the transition from small to large particles in the bidisperse configuration.

meaning that the particle velocity profile in the bidisperse case is just a translation of the velocity profile in the monodisperse case. In figure 5.6d is plotted, in the upper part of the bed, $v_m^p(z) + \Delta v$, with $\Delta v = 0.383\sqrt{gd_l}$ measured in the DEM simulation. The obtained curve is completely superimposed on the velocity profile in the bidisperse configuration. In both configurations, the large particles at the top have exactly the same behaviour.

The proposed granular analysis explains the observation made previously in figure 5.4, in which a layer of small particles was observed to be transported faster than larger particles at the same depth. Small particles consequentely play the role of a conveyor belt for the overlying particles and Δv represents a slip velocity. It additionally shows that the enhanced mobility is not a roughness effect, due to the reduction of roughness by smaller particles below the large particle layer. Indeed, if particles do not move at the interface, $\Delta v = v_b^p(z_i) - v_m^p(z_i)$ is zero and no enhanced mobility is observed, as in figure 5.4a. The fluid origin for the increased mobility can be discarded because the fluid shear stress is already fully transferred to the granular shear stress below $z = 0$. This analysis confirms that the enhanced mobility originates in the granular rheological properties of bidisperse beds.

This rheological analysis gives a qualitative understanding of the granular bed behaviour in the bidisperse configuration. To be more quantitative, the previous conclusions are used in order to predict analytically the additional transport in the bidisperse case.

5.4 A predictive model for the additional transport

In this section, a simple model is derived, the purpose of which is to predict the additional transport observed in the bidisperse case. To obtain a predictive model, the additional transport will be expressed as a function of the monodisperse quantities (Φ_m, v_m^p, etc...). The configuration is ideally simplified as a two layer problem in which small and large particles are completely separated at the interface depth z_i. The mixed layer of small and large particles, observed in the bidisperse DEM simulations, is here neglected. Therefore it is assumed that the mixture concentration profiles are identical in the bidisperse and in the monodisperse configuration, ie. $\Phi_m(z) = \Phi_b(z)$.

The transport in the bidisperse case is expressed as,

$$Q_b = \int_{-\infty}^{+\infty} v_b^p(z)\Phi_b(z)dz. \tag{5.10}$$

Below the interface between large and small particle, i.e. $z \leq z_i$, the previous analysis has shown that $v_b^p(z) = d_l/d_s v_m^p(z)$, while for $z > z_i$, $v_b^p(z) = v_m^p(z) + \Delta v$. Splitting the integral into two parts, below and above z_i, placing the velocity expression into equation (5.10) and recalling that $\Phi_b(z) = \Phi_l(z) + \Phi_s(z)$ is assumed to be equal to $\Phi_m(z)$, one obtains

$$Q_b = \int_{-\infty}^{z_i} \frac{d_l}{d_s} v_m^p(z)\Phi_m(z)dz + \int_{z_i}^{+\infty} (v_m^p(z) + \Delta v)\Phi_m(z)dz. \tag{5.11}$$

Distributing the second term and combining it with the first term,

$$Q_b = Q_m + (\frac{d_l}{d_s} - 1) \int_{-\infty}^{z_i} v_m^p(z)\Phi_m(z)dz + \int_{z_i}^{+\infty} \Delta v \Phi_m(z)dz. \tag{5.12}$$

where $Q_m = \int_{-\infty}^{+\infty} v_m^p(z)\Phi_m(z)dz$ is the monodisperse transport rate. Recalling that Δv is independent of z, the additional transport due to the presence of small particles can therefore be expressed as

$$\Delta Q = (\frac{d_l}{d_s} - 1) \int_{-\infty}^{z_i} v_m^p(z)\Phi_m(z)dz + \Delta v \int_{z_i}^{+\infty} \Phi_m(z)dz = \Delta Q_1 + \Delta Q_2. \tag{5.13}$$

The term ΔQ_1 represents the additional transport below the interface of the small particles, more mobile than larger particles. The term ΔQ_2 represents the additional transport of the large particles at the surface due to the conveyor belt effect. Note that in the monodisperse limit (i.e. $d_s = d_l$), both terms vanish. This is obvious for ΔQ_1. For ΔQ_2, it is $\Delta v = v_b^p - v_m^p$, which cancels in the monodisperse limit ($v_b^p = v_m^p$). Note that the additional transport in the bidisperse configuration (equation (5.13)) is expressed only as a function of monodisperse variables.

In order to verify that the model is consistent with the transport mechanisms at play, equation (5.13) is first tested using DEM monodisperse simulations as inputs. The additional transport terms ΔQ_1 and ΔQ_2 are computed using the DEM velocity and concentration profiles v_m^p, Φ_m and estimating the slip velocity Δv directly on the DEM simulations. The predicted dimensionless additional transport rates are plotted in figure 5.7. The additional transport in the bidisperse case is very well predicted by equation (5.13) for all values of Shields number and for all numbers of layers of large particles. The small errors obtained with equation (5.13) show that the model contains the significant physical ingredients acting in this transport process.

In practice, the concentration and velocity profiles, as well as the slip velocity, are difficult to obtain, and computing the additional transport due to the presence of small particles is not straightforward. In the following, a method to compute the two additional transport terms is proposed. The particles are assumed to be transported without dilatation of the bed. The concentration is therefore hypothesized constant and equal to $\Phi_{max} = 0.61$ in the bed with the top of the bed exactly at $z = 0$ (see figure 5.8a) as

$$\Phi_m(z) = \begin{cases} \Phi_{max} = 0.61, & z \leq 0 \\ 0, & z > 0 \end{cases} \tag{5.14}$$

To compute the ΔQ_1 additional small particle transport term, the monodisperse velocity profile for $z \leq z_i$ needs to be estimated. It can be derived using the $\mu(I)$ rheology (equation 2.30). The stress state (normal and shear stresses) of the granular bed needs to be computed. Based on the two-phase volume-averaged equations for turbulent bedload transport Jackson (2000); Chauchat (2018) and for the idealized step volume fraction profile (equation 5.14), the granular pressure and shear stress profiles were computed

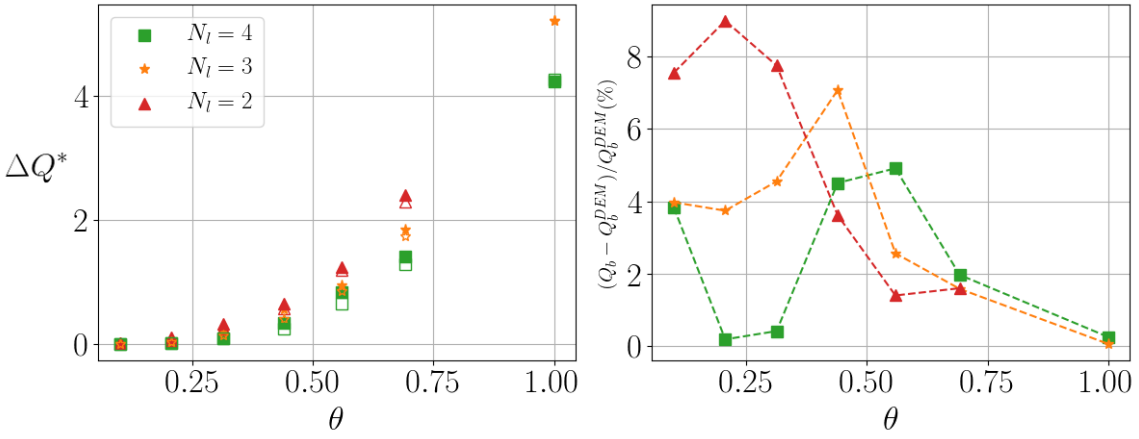

(a) (b)

Figure 5.7: (a) Dimensionless additional transport measured in the DEM simulations (full symbols) and predicted by equation (5.13) (empty symbols), for different values of the Shields number and N_l. Only cases for which the surface is composed of large particles only are presented for readability. (b) Error between the total transport predicted by equation (5.12) and the measured one with the DEM simulations.

analytically in section 2.2.4. It yielded

$$P^p(z) = \left(\rho^p - \rho^f\right) g \cos(\alpha) \Phi_{max} z, \tag{5.15}$$

$$\tau^p = \tau_b + \left(\rho^f + (\rho^p - \rho^f)\Phi_{max}\right) g \sin(\alpha) z, \tag{5.16}$$

where $\tau_b = \rho^f g h_w \sin(\alpha)$ is the fluid bed shear stress. The friction coefficient can be computed analytically as $\mu = \tau^p / P^p$ with these profiles. Inverting the $\mu(I)$ rheology (equation 2.30), replacing the inertial number I by its expression (equation 2.29) with the large particle diameter and integrating, a velocity profile is obtained

$$v_m^p(z) = \begin{cases} 0, & \mu(z) < \mu_c, \\ \displaystyle\int_{z_1}^{z} \left(\sqrt{\frac{P^p(\zeta)}{\rho^p}} \frac{I_0}{d_l} \frac{\mu(\zeta) - \mu_c}{\mu_2 - \mu(\zeta)} \right) d\zeta, & \mu_c \leq \mu(z) < \mu_2, \end{cases} \tag{5.17}$$

where $\mu_c = 0.35$, $\mu_2 = 0.97$ and $I_0 = 0.69$ are the set of parameters proposed by Maurin et al. (2016) for bedload transport. The integral can be computed numerically with the analytical expression of the granular pressure and of the friction coefficient and without any data from the DEM simulations.

To verify that this derivation is consistent with the DEM simulations, figure 5.8 compares, for the monodisperse simulation at $\theta \sim 0.45$, (a) the idealized concentration, (b) the pressure and shear stress, (c) the friction coefficient and (d) the velocity profile with the DEM results. The idealized step concentration profile obviously does not reproduce

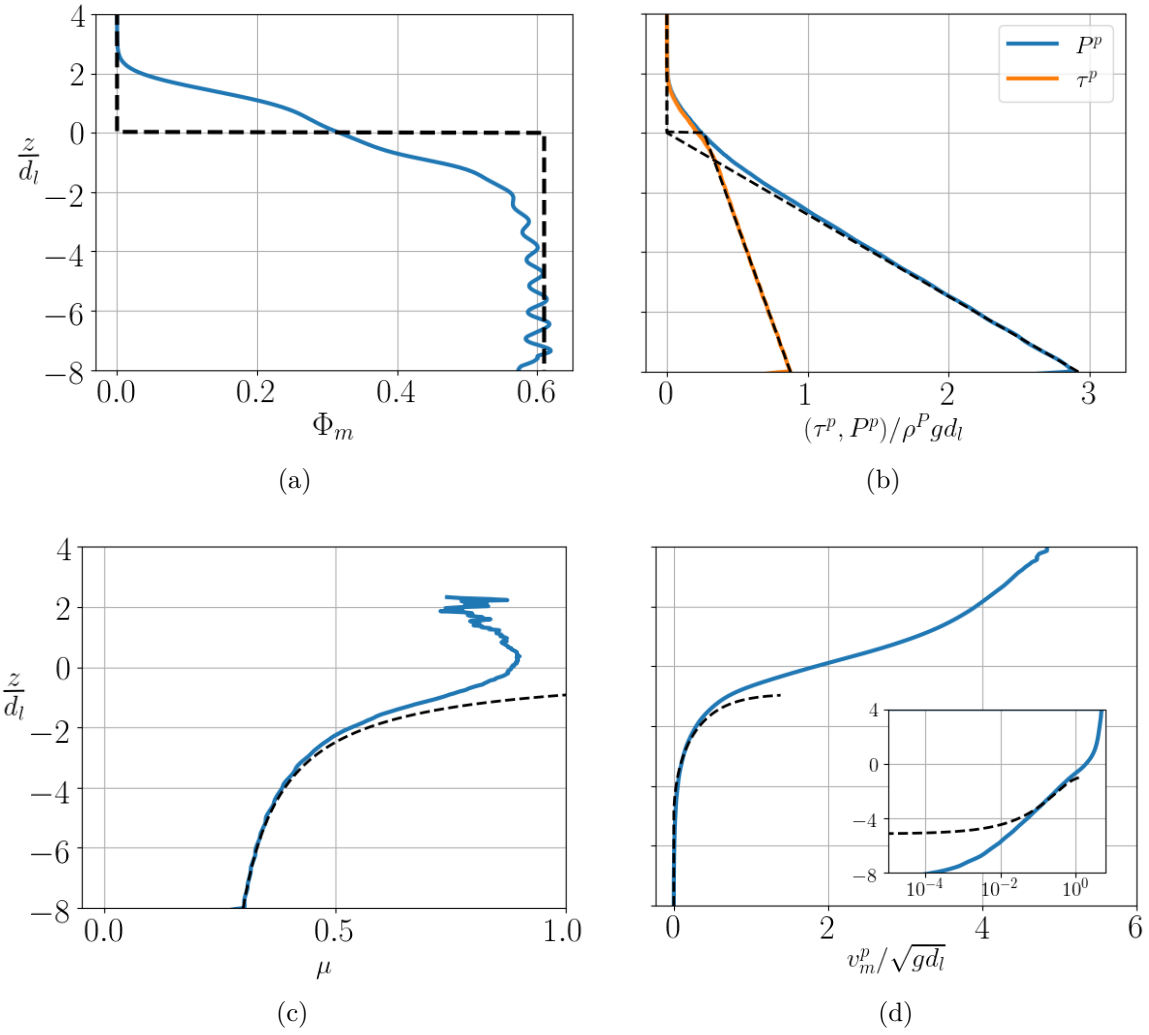

Figure 5.8: Comparison between idealized (dotted lines) and DEM profiles (full lines) in the monodisperse configuration for $\theta \sim 0.45$. (a) Concentration profiles, (b) granular pressure and shear stress profiles, (c) friction coefficient profiles and (d) velocity profiles.

the dilatation of the bed at the surface. As a result, the pressure and shear stresses correspond with the DEM results in most part of the bed but differ close to the surface. Similarly, discrepancies near the bed surface appear for the friction coefficient and the velocity profiles. However, in the expression of ΔQ_1, the velocity and concentration profiles are needed only for $z \leq z_i$, where the idealized concentration and stresses agree very well with the DEM ones. Concerning the velocity profile (figure 5.8d), the $\mu(I)$ rheology can not predict the quasi-static regime as already mentioned (see inset of figure 5.8d). The velocity profile is well predicted in the dense regime but the rheology fails to predict the velocity in the upper part of the bed for $\mu \geq \mu_2$, which corresponds to a more dilute flow regime. In order to use the predictive model, it is therefore necessary that $\mu(z_i) < \mu_2$, which is the case in all our simulations and should be the case in classical bedload transport configurations. Otherwise, it would mean that small particles are in the dilute flow regime and would be present at the bed surface, configuration which has already been discarded. With the velocity profile (5.17), it is now possible to compute the first additional transport term ΔQ_1 without any data from the DEM simulations.

To compute the second additional transport term ΔQ_2, both the Δv slip velocity and the $\int_{z_i}^{+\infty} \Phi_m(z)dz$ term need to be estimated. The second term represents the amount of large particles slipping above the small particles. With the idealized concentration profile, it can be directly computed as

$$\int_{z_i}^{+\infty} \Phi_m(z)dz = \Phi_{max} N_l d_l. \tag{5.18}$$

Lastly, the slip velocity remains to be estimated. By definition, for $z \geq z_i$, $\Delta v = v_b^p(z) - v_m^p(z)$. It is therefore valid in $z = z_i$, where $v_b^p(z_i) = d_l/d_s v_m^p(z_i)$. The slip velocity is therefore finally given by

$$\Delta v = \left(\frac{d_l}{d_s} - 1\right) v_m^p(z_i), \tag{5.19}$$

with $v_m^p(z_i)$ which can be computed from the velocity profile equation (5.17) derived previously. All additional transport terms can now be computed and the total additional transport can be expressed as

$$\Delta Q = (\frac{d_l}{d_s} - 1)\Phi_{max} \left(\int_0^{z_i} v_m^p(z)dz + N_l d_l v_m^p(z_i) \right), \tag{5.20}$$

with $v_m^p(z)$ given by equation (5.17). This additional transport term can be computed without any DEM data and only uses the $\mu(I)$ rheology.

Equation (5.20) is tested and compared with the additional transport rate directly measured with the DEM simulations in figure 5.9. The model predicts well the additional transport with an error of less than 10% in most cases and a maximum error around 20%. The error is generally smaller when N_l is larger. For each configuration, there is a region where the error is maximum. The Shields number at which the maximum is reached seems to depend on the large particle number of layers (see figure 5.9b). The results are discussed

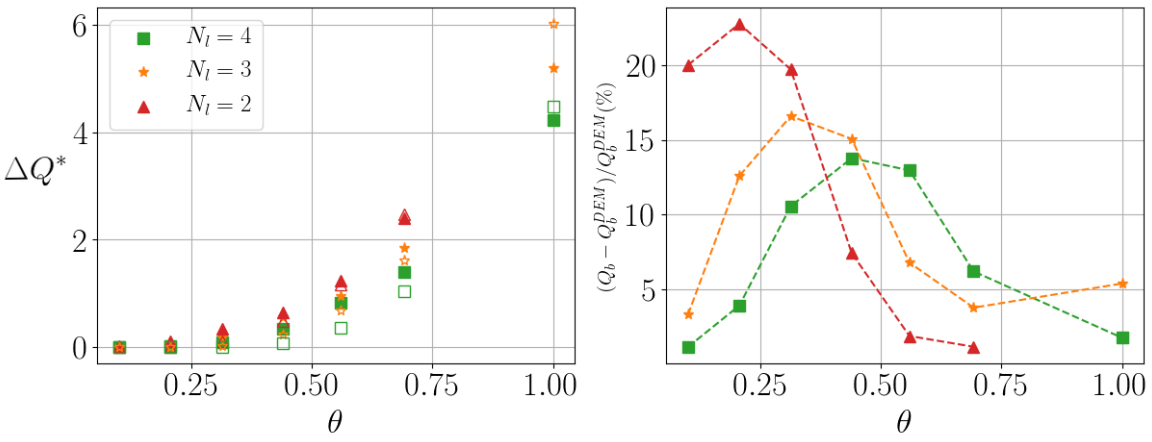

(a) (b)

Figure 5.9: (a) Dimensionless additional transport in the bidisperse case measured with the DEM simulations (full symbols) or computed with equation (5.20) (empty symbols), for different values of Shields number and N_l. Only cases for which the surface is composed of large particles only are presented for readability. (b) Error between the total bidisperse transport predicted by equation (5.20) and the measured one with the DEM simulations.

and interpreted in the next section.

5.5 Discussion and conclusion

This study has shown that the additional transport evidenced in an inversely graded bidispersed bed is a granular process. In a granular flow, small particles being more mobile than larger ones, they play the role of a conveyor belt for the overlying large particles. Assuming that large and small particles are completely separated and are transported without dilatation of the bed, a model for the enhanced transport has been derived based on rheological arguments. The results have shown that our model contains the significant physical ingredients of the transport process and is able to predict acccurately the additional transport due to bidispersity in bedload transport. The developed model allows improving upon classical transport laws by taking into account not only the classical bed surface state, but the entire mobile granular bed structure.

This model can also be used as a tool to interpret the different transport mechanisms observed in this bidisperse granular flow configuration. The different regimes observed are summarized in figure 5.10. The map has been built from the regions of validity of the model, the blue squares showing regions where the error between the model prediction and the DEM is less than 10% while the brown ones show regions where the error is higher. This criterion enables us to define four different regimes of granular flows, corresponding to different granular depth structures and flowing mechanisms. Regime 1 corresponds to cases where small and large particles are well mixed, with small particles present at the

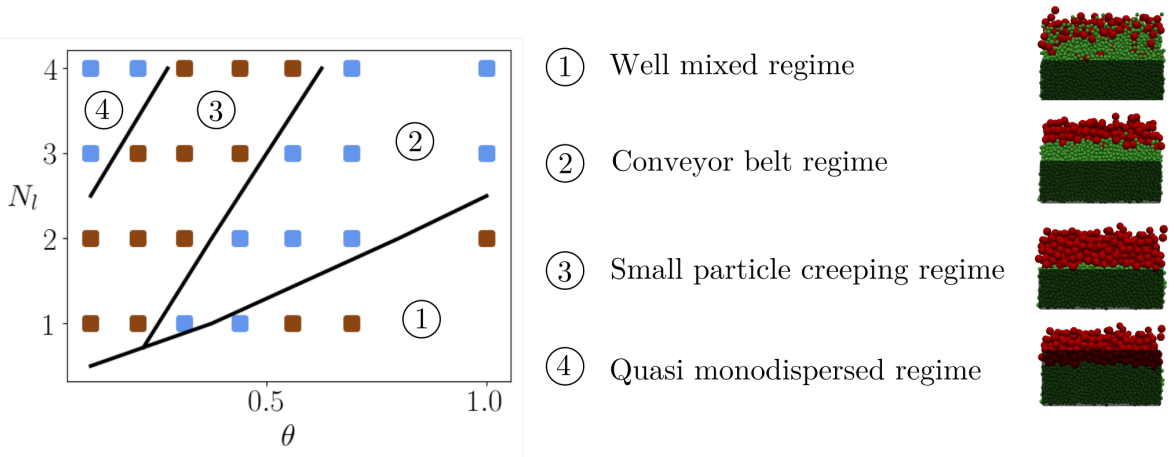

Figure 5.10: Mapping of the four different observed phenomenologies in the bidisperse transport process. Each regime is illustrated with a typical simulation picture where the creeping flow has been shaded in gray. Results are plotted in colored squares and split into two classes : blue (predicted transport error less than 10%) and brown (larger error).

bed surface. In those cases, the additional transport is a combination of granular and fluid processes. Indeed, smaller particles at the surface are more easily entrained by the fluid flow and the mixture of small and large particles can affect the flowing properties of the granular mobile layer. Regime 2 corresponds to the domain of validity of the proposed model, where all assumptions are verified. In this regime, the fluid-driven large particles entrain the small ones, which create a so-called conveyor belt effect, due to their higher mobility. The transition depth between small and large particles is here located in the dense granular flow region. When the transition is located deeper in the bed, near or inside the creeping flow region, the $\mu(I)$ rheology is no longer valid and the model predicts erroneously a zero velocity inside the small particle layer (see inset figure 5.8d). This third regime therefore leads to small ($< 25\%$) but non negligible errors in the model predictions, due to the absence of modelled slip velocity and additional transport. This indicates that the quasi-static part of the bed may play a non neglible role in the sediment transport process (Houssais et al., 2015; Ferdowsi et al., 2017). Regime 4 corresponds to cases where the transition depth is very deep in the bed and no additional transport due to the presence of small particles is observed in the DEM simulations or predicted by our model. The bidisperse nature of the bed can be neglected in this regime.

The model and the phenomenology map have been derived considering assumptions a priori valid for any granular flow on a pile. Therefore, this analysis should remain valid for other flow configurations of bidisperse mixtures with larger particles on top of smaller ones. In addition, the mechanisms described herein rely only on rheological arguments and one can expect the analysis to hold for any granular flow. Indeed, when submitted to the same stress, small particles are more mobile than larger particles and the effect observed for polydisperse granular collapses (Linares-Guerrero et al., 2007; Lai et al., 2017) or granular avalanches, for example, can be interpreted similarly. During the collapse, the small particles segregate and form a basal flowing layer, setting up a conveyor belt effect

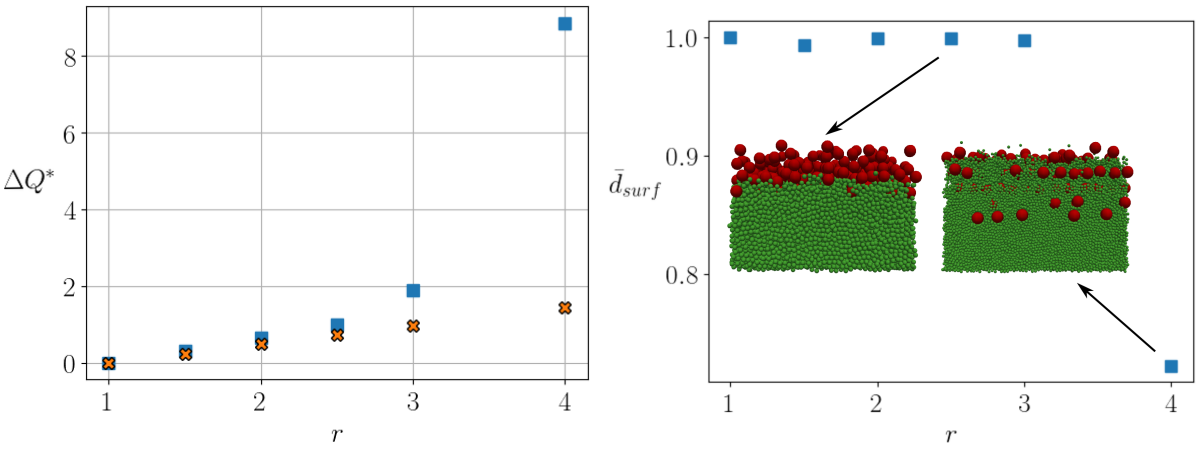

(a) (b)

Figure 5.11: (a) Additional transport rate predicted by equation (5.20) (orange crosses) and computed from the DEM simulations (blue squares) for different size ratios at $\theta \sim 0.45$ and $N_l = 2$. (b) Non-dimensional surface diameter in the DEM simulations as defined in equation (5.3) as a function of the size ratio. Cases $r = 2.5$ and $r = 4$ are illustrated with a picture from the DEM simulation.

and increasing the runout distance of the collapse.

The results obtained in this study can be put into perspective by considering the dependency of the results on the size ratio. Varying the size ratio between $r = 1.5$ and $r = 4$ for a given configuration ($\theta = 0.45$, $N_l = 2$), one can evidence that the transport predicted by the model is valid up to $r = 2.5$ (see figure 5.11a). For a larger size ratio, the increased transport observed in the DEM is much higher than predicted by the model. This effect seems to be related to a drastic change in the granular flow structure. Indeed, the mean surface particle diameter, representative of the mixing of small and large particles changes drastically between a size ratio of $r = 3$ and $r = 4$ (see figure 5.11b). This indicates that diffusion remixing increases significantly, and can be related to the onset of inverse segregation as observed in this range of size ratio by Thomas (2000). This link between diffusion and inverse size segregation challenges our understanding of size segregation and deserves future work.

Chapter 6

Conclusions and perspectives

The present PhD study has focused on the analysis of gravity-driven size segregation in bedload transport. The aim was to improve our understanding of the mechanisms controlling and responsible for size segregation in this particularly complex configuration, and to study its impact on the sediment transport rate. This PhD work has addressed different size segregation problems in bedload transport, with a panel of complementary approaches and in different configurations. Size segregation has been studied in both the quasi-static and the dense regimes, and analysed with discrete and continuum models. The segregation dynamics and its impacts on sediment transport were investigated. This study therefore gives an overview of size segregation during bedload transport and opens new challenging perspectives.

6.1 Conclusions

For this study, the coupled fluid-DEM model developed by Maurin et al. (2015) has been adapted to bidisperse configurations. It allowed us to study the segregation mechanisms in bedload transport in two different configurations.

In the first one, the mechanisms controlling the infiltration of small particles in a bed made of large particles have been investigated in the quasi-static regime. Small particles have been observed to infiltrate the bed all together, as a travelling wave, forming a layer of constant thickness. This segregation dynamics has been shown to be controlled by the inertial number to the power 0.85 and by the local small particle concentration, confirming and extending results observed in other dense granular flow configurations (Fry et al., 2018; Dolgunin and Ukolov, 1995; Jones et al., 2018). The segregation velocity has also been observed to increase with the size ratio, but with no evidence of a local maximum at a size ratio of two as observed in other configurations (Golick and Daniels, 2009; Thornton et al., 2012; Guillard et al., 2016). The existence and stability of the small particle layer was demonstrated to be related to the exponential profile of the inertial number, specific to flows on erodible beds, and to result from an equilibrium of the combined effects of the inertial number and of the small particle concentration. Finally, diffusive remixing of small particles into the large particle phase was demonstrated to be controlled by the inertial number with the same dependency as segregation. It means that the Peclet number,

defined as the ratio of segregation over diffusion is constant in the quasi-static regime.

In a second configuration, the evolution of initially segregated beds has been studied with the coupled fluid-DEM model. The interface depth between large and small particles was set in the dense regime. It was observed that, depending on the depth of the interface, on the Shields number and on the size ratio, the bed can remain well separated or can be well mixed. This bed state has been shown to result from the relative importance of size segregation over diffusion. The dependence on the Shields number allowed us to conclude that, in the dense regime, the Peclet number is not constant, that is to say that diffusion remixing do not scale as segregation. This represents a main difference between the quasi-static and the dense regime for the segregation processes.

The discrete simulation results have been upscaled to a continuum framework, using the advection-diffusion model for size segregation of Gray and Thornton (2005), Thornton et al. (2006) and Gray and Chugunov (2006). First, the infiltration of small particles in the quasi-static bed has been studied. With advection and diffusion coefficients proportional to the inertial number to the power 0.85, the dynamics of segregation is perfectly reproduced. In this PhD, the advection-diffusion model has been used not only to upscale results but also to evidence the complex interplay between the effects of the inertial number, of the small particle concentration and of diffusion. This represents an original way to use continuum models.

In order to enrich our understanding of the size segregation processes, physically based parametrisations of the advection and diffusion coefficients were necessary. At the particle scale, a large intruder is submitted, due to interactions with surrounding small particles, to a buoyancy segregation force (Guillard et al., 2016) and a granular drag force (Tripathi and Khakhar, 2011a). Based on these particle scale forces, a new advection-diffusion model for segregation has been derived by Hugo Rousseau, a PhD colleague at INRAE. This model therefore contains advection and diffusion coefficients with dependencies on local physical parameters, such as the small particle concentration, granular pressure and its gradient, the granular Stokes number and the segregation function. In this PhD, a numerical method to solve the model has been proposed. The numerical solution has been compared with the DEM results of the first configuration. Without any tuning parameters, the model reproduces qualitatively the DEM results, in particular the infiltration as a layer and the logarithmic descent with time. The granular viscosity has been shown to play a major role in the segregation process, which can be interpreted as a free fall of small particles in a complex fluid with varying viscosity.

In order to reproduce quantitatively the DEM results, additional dependencies with the inertial number, the pressure, the small particle concentration and the size ratio have been proposed in the segregation function and the drag coefficient. These dependencies are based on fits and should therefore be verified on other, more canonical, flow configurations. The capacity of this new advection-diffusion model to reproduce our simulations is very encouraging and represents a first step in the upscaling process since it has been derived from solid physical arguments using particle scale forces obtained in independent configurations. It would be of major interest to use this model in other flow configurations.

Finally the impact of size segregation on sediment transport has been studied in the already segregated configuration with DEM simulations. It was observed that, for the same flow conditions, the transport rate is higher in the bidisperse configuration than in the monodisperse one. In cases where the small particles hardly mix with the overlying large particles and for the range of studied size ratios ($r < 4$), it has been shown that the increased mobility is not due to the reduction of roughness of the underlying small particles, but to a granular flow effect due to rheological granular properties. Small particles being more mobile than larger particles, they play the role of a conveyor belt for the overlying large particles, increasing the total mobility of the bed. A simple predictive model for the increase of transport, based on these rheological arguments, has been proposed. It reproduces quantitatively the DEM results. The results of the model were used to identify four different transport regimes of bidisperse mixtures, depending on the mechanisms responsible for the mobility of the small particles. These results highlight the role of the depth structure on the bed mobility and shows that, not only hydrodynamics but also granular effects may impact sediment transport laws of bidisperse mixtures. This represents an alternative and original approach of bidisperse bed mobility based on physical granular media theories, relevant for intense transport regimes.

This PhD research represents an original contribution to the understanding of size segregation in bedload transport and in granular flows in general. Bedload transport allowed us to explore size segregation in a complex forcing configuration and for a wide range of inertial numbers. The result similarities with other studies indicate that the obtained results could be more general. A first step toward larger scales has been achieved with continuum segregation models. This PhD also shows that size segregation can not be dissociated from the study of diffusive remixing, which is part of the size segregation process. Diffusive remixing in granular media has been barely studied and this opens new perspectives for size segregation.

6.2 Perspectives

This PhD has addressed several size segregation problems during bedload transport with different approaches. Some questions have been answered but many have been raised. First, the generalization of the results, to laboratory experiments and to other granular flow configurations, can be questioned. Second, it has been attempted to relate particle scale results to continuum models. Despite the success of the study, it was shown that some efforts are still needed to understand the nature of size segregation at the particle scale. Finally, the role of diffusion in the segregation processes has been highlighted, emphasizing the necessity to investigate diffusive remixing.

6.2.1 Interpretation of size segregation in laboratory experiments

The results presented in this PhD have been obtained in idealized 3D configurations and with coupled fluid-DEM simulations. This model is built on grain-grain and fluid-grain

interaction laws that could be inaccurate. A comparison with laboratory experiments would therefore be of major interest.

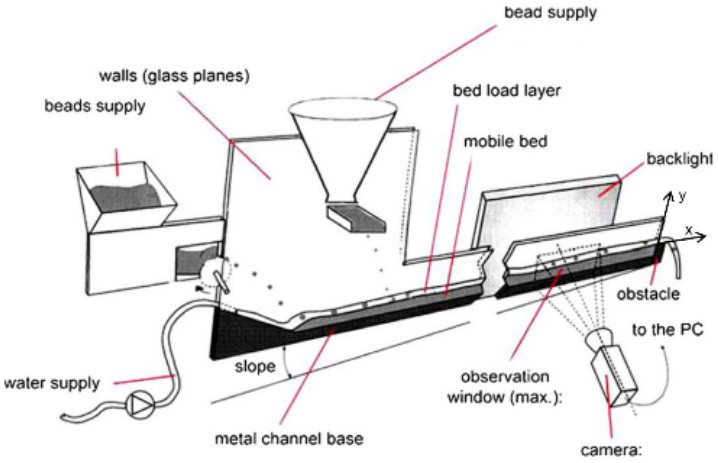

Figure 6.1: Scheme of the experimental device (adapted from Frey et al. (2020)).

At INRAE, a quasi-2D channel is used to study bedload transport at the particle scale. The experimental device is presented in figure 6.1 and has been recently used to study size segregation mechanisms (Frey et al., 2020) and its impact on sediment mobility (Dudill et al., 2017, 2018). The fluid and solid flow rates are imposed upstream and the slope adjusts itself so that the transport capacity of the channel corresponds to the solid supply. This configuration differs from the one studied in this PhD work as it is space dependent in the streamwise direction. Indeed, small particles are advected not only vertically due to size segregation but also in the streamwise direction by the mean granular flow (the term $\nabla \cdot (\boldsymbol{u}\phi_s)$ does not vanish in the advection-diffusion models). In order to interpret experiments performed in this channel, it would be necessary to transpose the results of this PhD work to this configuration.

However the same segregation patterns have been observed in the channel experiments. In Frey et al. (2020), the infiltration of small particles was studied. As in the DEM simulations, a small particle layer occured (see figure 6.2a) showing a logarithmic time elevation descent. Dudill et al. (2018) studied the slope evolution upon infiltration of fine particles. In some cases, as in figure 6.2b, a small particle layer builds below the surface and the slope decreases. The conveyor belt effect, highlighted in chapter 5 is particularly visible in picture 6.2b. This indicates that the bed mobility increased, a lower slope being sufficient to transport a higher quantity of sediments. To go further, it would be interesting to relate the increased mobility mechanism described in this PhD work to the slope evolution, which is a key parameter when studying the geomorphological evolution of rivers.

It seems therefore that this device is particularly relevant to verify experimentally the results obtained in the present PhD work. It is a more complex system, with a great variety of segregation processes, complementary to the DEM simulations.

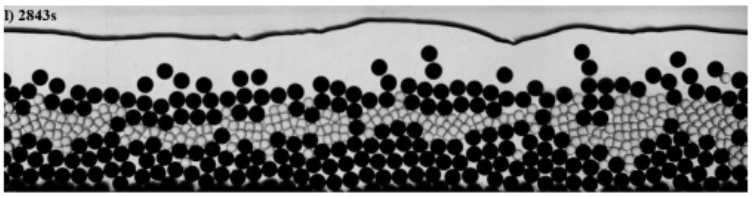

(a)

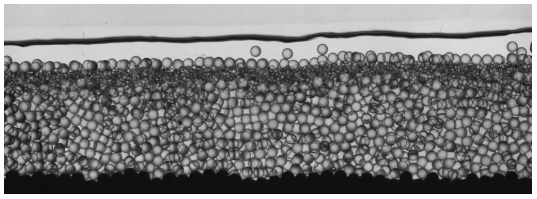

(b)

Figure 6.2: Example of laboratory experiments of bidisperse bed during bedload transport. (a) A small particle layer infiltrates the bed made of large particles, from Frey et al. (2020). (b) The flow is from left to right and the picture is taken parallel to the bottom slope. A small particle layer builds below the surface resulting in a reduction of the bed slope (image Frey unpublished).

6.2.2 Extension to other configurations

The bedload configuration allowed us to study size segregation in a complex forcing. In particular the exponential form of the inertial number was shown to influence strongly the segregation dynamics. In addition, part of the results were obtained in the quasi-static regime and it would be interesting to know if they are more general. Similarities with other works in the dense regime, in particular the scaling with the inertial number (Fry et al., 2018) and the dependence on the small particle concentration (Dolgunin and Ukolov, 1995; Jones et al., 2018), suggest that it is the case. A comparison between the segregation dynamics in several dry canonical configurations, such as Bagnold flows, heap flows and simple shear configurations would be valuable to understand size segregation in the general case.

As mentioned in the introduction, the granular community started to investigate the mobility of bidisperse avalanches (Linares-Guerrero et al., 2007) and of granular collapses with fractal size distributions (Lai et al., 2017). They observed the formation of a small particle basal layer due to size segregation correlated with an increase of mobility of the granular flow. They did not propose physical explanations, but it reminds the conveyor belt effect highlighted in the mobility problem studied in this PhD work. It would therefore be interesting to verify if the rheological arguments provided in chapter 5 are still valid in the dry configurations of Linares-Guerrero et al. (2007) and Lai et al. (2017).

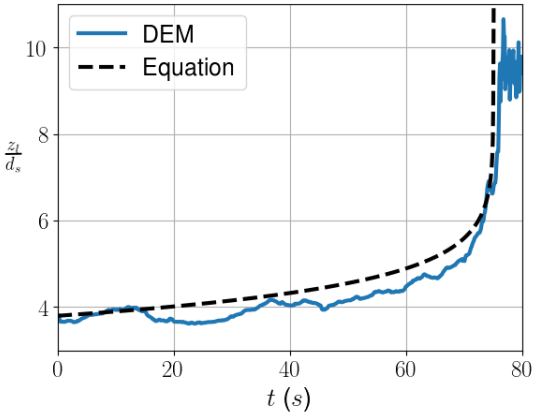

Figure 6.3: Vertical position with time of a large intruder in a small particle bed obtained with a DEM simulation and compared with equation (6.1). $\theta \sim 0.3$, $r = 2$.

6.2.3 Rise of a large intruder

In chapter 4, the segregation dynamics has been studied based on particle scale forces. In order to reproduce quantitatively the DEM results, some additonal dependencies were proposed in the segregation function of Guillard et al. (2016) and in the drag coefficient (Tripathi and Khakhar, 2011a).

To verify these dependencies, that are at the base of discrete and continuum modelling of size segregation, it would be interesting to investigate the case of a single large intruder in a small particle bed and to study its elevation evolution. This configuration can be set up very easily with DEM simulations. The DEM is a very powerful tool to study these dependencies as it allows one to access the number of contacts and the forces applied by other particles on the intruder. My intuition is that the number of contacts and the repartition of forces on the intruder are key parameters to understand the nature of size segregation and the effect of the size ratio. The geomechanics community could provide useful tools to analyse size segregation and the related dependencies with such an approach.

With the intruder configuration, it is also possible to track the rise of the large particle. Figure 6.3 shows the elevation evolution with time of a large intruder obtained with a DEM simulation. The segregation velocity is low in the quasi-static regime and strongly increases while elevating. The elevation of the intruder can be compared with the following equation of motion

$$\rho^p V_l \frac{dw_l}{dt} = V_l \left(\mathcal{F} - \frac{1}{\Phi} \right) \Phi(\rho^p - \rho^f) g \cos(\alpha) - c\pi d_l \eta^p (w_l - w_p). \tag{6.1}$$

Assuming a constant value of $\mathcal{F} = 1.78$ and $c = 3$, equation (6.1) is solved numerically and plotted in figure 6.3a (dashed line). The numerical solution represents almost perfectly the trend of the DEM solution, showing that it contains the good physical ingredients. However, the numerical solution is very sensitive to the value of $\mathcal{F}$, which had to be tuned. This shows that the segregation $\mathcal{F}$ is a key parameter of the segregation equation, and comparisons with DEM simulations could help to infer the underlying dependencies.

The experimental device presented in figure 6.1 could also be used to study the rise of the intruder. Indeed, the quasi-2D nature of the channel allows the tracking of the intruder. It could be used to compare with DEM simulations but also with the equation of motion (eq. 6.1).

6.2.4 Diffusive remixing

All along this PhD work, the lack of knowledge on diffusive remixing has been noticed. It has however been stressed out that size segregation can not be dissociated from diffusive remixing. Additionally, this is a question of primary importance for industrial applications, when a well-mixed granular medium is needed, and for geophysical applications, for example to know whether the surface state of the bed is well mixed or segregated. The present PhD started to address this issue by considering the Peclet number, defined as the ratio between segregation and diffusion. The Peclet number was observed constant in the quasi-static regime but non constant in the dense regime, suggesting a difference of behaviour between both granular flow regimes.

To focus deeper on the study of diffusive remixing, the intruder configuration could also be used. Adopting a statistical approach, information on the diffusion coefficient could be obtained computing the standard deviation around the mean trajectory. This could be performed in the bedload configuration, with DEM simulations or the experimental channel, and in other dry granular flows such as Bagnold or simple shear flows. This is classically done to study self-diffusion (Campbell, 1997; Utter and Behringer, 2004), and can be extended to bidisperse configurations.

The already segregated configuration is also very interesting to study diffusive remixing. As mentioned in chapter 5, the width of the transition between small and large particles depends on the relative importance of segregation over diffusion. The shape and width of the transition could be studied in more details, using the advection-diffusion model, to extract more information on segregation and diffusion.

When increasing the size ratio, a completely different phenomenology occured, which deserves a special attention. The granular flow structure was observed to drastically change at $r = 4$ (figure 5.11). Trains of large particles formed deep in the bed and found stable positions, as shown in figure 6.4. This sudden transition of the bed structure with the size ratio suggests a granular instability. By analogy with fluid dynamics, this situation could be analysed as a Rayleigh-Benard instability in stratified fluids. Indeed, small particles are more mobile than the overlying large particles. The granular temperature is therefore expected to be higher below the transition depth. The problem can be interpreted as a two-layer problem with a hot region below a colder region, resulting in a vertical transfer of particles. This mixing process could therefore be approached as a turbulent mixing process. This situation reminds of the reverse segregation of large beads observed experimentally by Thomas (2000) in dry granular avalanches. The author observed a transition around $r = 4$ from normal to reverse segregation, exactly as in our simulations. The mechanisms at play may therefore to be the same. This configuration represents a very promising problem

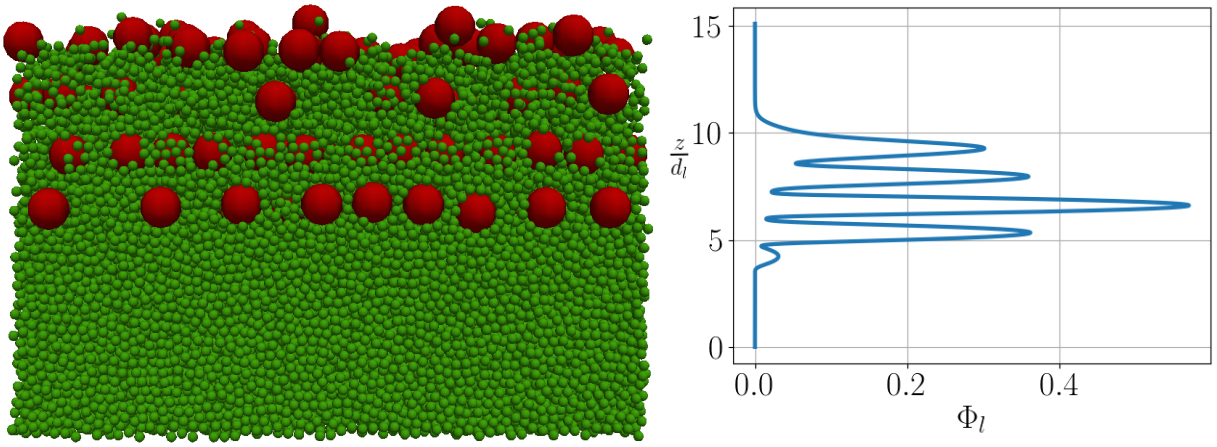

(a) (b)

Figure 6.4: Initially $N_l = 2$ layers of large particles were placed above small particles, with a size ratio $r = 4$. At steady state, trains of large particles formed inside the bed, suggesting a granular instability. (a) Picture of the DEM simulation at steady state. (b) Volume fraction of large particles.

to study segregation and diffusion mechanisms in granular media. This challenges the classical vision of size segregation and opens nice perspectives.

Appendix A

Sensitivity analysis of the fluid-DEM model in bidisperse configurations

Maurin (2015) performed a sensitivity analysis on the exact same coupled fluid-DEM code with monodisperse simulations and showed that the DEM results were not so sensitive to the input parameters. In order to verify again the robustness in bidisperse configuration, a new sensitivity analysis has been performed. In the DEM, the adjustable parameters are the restitution coefficient e_n, which is not easy to determine *a priori*, and the particle friction coefficient μ_p. The fluid coupling only depends on the drag formulation, in which the hindrance correction function can be questionned. In this sensitivity analysis, the restitution coefficient e_n is strongly varied around $e_n = 0.5$, the value used in this PhD, and the particle friction coefficient is increased, as the one used in this PhD is already a low value ($\mu_p = 0.4$). Concerning the drag formulation, only the case without hindrance is tested, i.e. $\zeta = 0$. The different simulations, with corresponding parameters, are reported in table A.1. They have been made at $N_s = 1$ and $d_s = 0.004$ m, as this is the reference case in this PhD. The 'Ref' simulation corresponds to the one presented in the PhD (restitution coefficient $e_n = 0.5$, particle friction coefficient $\mu_p = 0.4$, hindrance exponent $\zeta = 3.1$).

Run	e_n	μ_p	ζ
Ref	0.5	0.4	3.1
$e_n = 0.25$	0.25	0.4	3.1
$e_n = 0.75$	0.75	0.4	3.1
$\mu_p = 0.6$	0.5	0.6	3.1
$\mu_p = 0.8$	0.5	0.8	3.1
$\zeta = 0$	0.5	0.4	0.0

Table A.1

The results of these simulations are shown in figure A.1. The packing fraction profile is barely not affected by the modification of the parameters. Concerning the velocity profile, the same behaviour is observed in all simulations. The velocity is exponentially

decreasing into the bed. The slope seem however slightly affected by the parameters. This is not surprising as the hindrance coefficient modifies the fluid-particle coupling, and the friction and restitution coefficients affect the vertical structure of the granular flow. On the whole, this sensitivity analysis shows that the behaviour of the mixture bed is not so much affected by the parameters.

Concerning the segregation dynamics, figure A.1c shows the segregation velocity of the small particles as a function of the local inertial number. Despite the small variations observed on the velocity profile, the segregation velocity scales with the inertial number exactly the same way in all simulations. The same 0.85 exponent is recovered and the curves are superimposed. This shows that the input parameters are not influencing the segregation dynamics and the scaling with the inertial number is valid whatever the value of the restitution coefficient, friction coefficient or hindrance. It conforts the results presented in this PhD work.

In this sensitivity analysis, the fluid model resolution parameters, such as the size of the averaging weighting function, have not been tested. Indeed, the exact same values as in Maurin et al. (2015) have been used, and Maurin (2015) showed that the model is not sensitive to these parameters, which are not modified by the bidisperse nature of the bed.

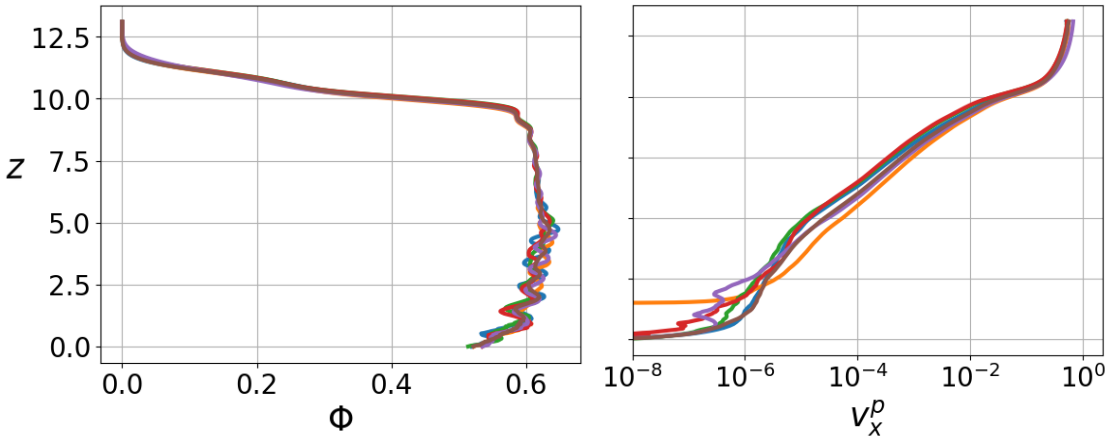

(a) (b)

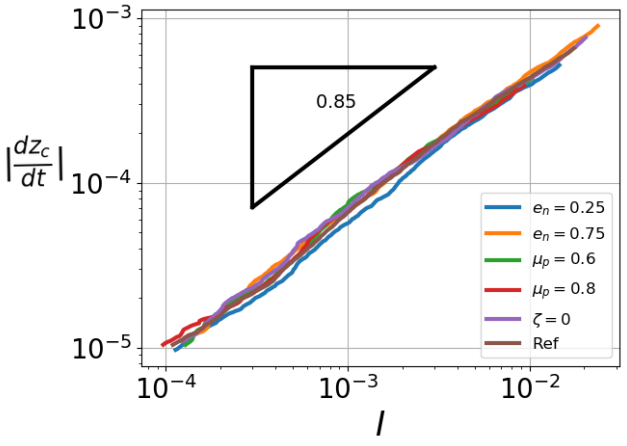

(c)

Figure A.1: Sensitivity analysis for all simulations presented in table A.1. (a) Packing fraction profile, (b) velocity profile and (c) segregation velocity as a function of the inertial number.

Appendix B

Solution of the purely advective segregation model

May et al. (2010) already derived a solution to the model of Thornton et al. (2006) with an exponential dependence of the segregation flux with z. In this appendix, the full solution is presented in the bedload configuration. The segregation equation to solve is

$$\frac{\partial \phi_s}{\partial t} - \frac{\partial F_s}{\partial z} = 0, \tag{B.1}$$

with the flux $F_s = S_{r0} e^{z/c} \phi_s (1 - \phi_s)$ and an initial step condition in concentration

$$\phi_{s0} = \phi_s(z, 0) = \begin{cases} 0, & z < z_i, \\ 1, & z \geq z_i. \end{cases} \tag{B.2}$$

The boundary conditions ensure that there is no flux at $z = 0, H$, which requires that

$$\phi_s = 0 \text{ or } 1, \quad \text{at} \quad z = 0 \text{ and } H. \tag{B.3}$$

Substituting the flux into (B.1) implies

$$\frac{\partial \phi_s}{\partial t} + W(z, \phi_s) \frac{\partial \phi_s}{\partial z} = S(z, \phi_s) \tag{B.4}$$

where

$$W(z, \phi_s) = S_{r0} e^{z/c} \left(2\phi_s - 1\right), \tag{B.5}$$

$$S(z, \phi_s) = \frac{S_{r0}}{c} e^{z/c} \phi_s (1 - \phi_s). \tag{B.6}$$

Due to dependence of the flux both on z and ϕ_s, the equation to solve has a non-linear advective velocity and a source term. In the following, this problem is solved using the method of characteristics.

On a characteristic curve $(Z(s), t(s))$,

$$\frac{d\phi_s}{ds} = \frac{\partial \phi_s}{\partial t}\frac{dt}{ds} + \frac{\partial \phi_s}{\partial z}\frac{dz}{ds} = S. \tag{B.7}$$

Comparing coefficients of (B.4) and (B.7)

$$\frac{d\phi_s}{ds} = S, \tag{B.8}$$

$$\frac{dt}{ds} = 1, \tag{B.9}$$

$$\frac{dZ}{ds} = W. \tag{B.10}$$

Eliminating s implies

$$\frac{d\phi_s}{dt} = S \tag{B.11}$$

$$\frac{dZ}{dt} = W. \tag{B.12}$$

The problem (B.4) is thus equivalent to the following system

$$\begin{cases} \dfrac{d}{dt}\phi_s(Z(t),t) &= S\left(Z(t), \phi_s\left(Z(t),t\right)\right), \\ \dfrac{dZ(t)}{dt} &= W\left(Z(t), \phi_s\left(Z(t),t\right)\right), \\ Z(0) &= z_0. \end{cases} \tag{B.13}$$

The first equation indicates that ϕ_s is not constant along a characteristic curve and the second equation that the characteristic curves are not linear. The method of characteristics consists in solving the value of ϕ_s along the characteristics curves. If a characteristic curve passing by each time and space position exists, then the problem can be fully resolved. In order to compute the value of ϕ_s along a characteristic curve, the first equation of (B.13) is differentiated with time

$$\frac{d^2}{dt^2}\phi_s(Z(t),t) = \frac{d}{dt}\left[S\left(Z(t), \phi_s\left(Z(t),t\right)\right)\right], \tag{B.14}$$

distributing the derivative,

$$\frac{d^2}{dt^2}\phi_s(Z(t),t) = \frac{dZ}{dt}\frac{\partial S}{\partial z} + \frac{d\phi_s\left(Z(t),t\right)}{dt}\frac{\partial S}{\partial \phi_s}, \tag{B.15}$$

and introducing the first and second equation of (B.13) it implies,

$$\frac{d^2}{dt^2}\phi_s(Z(t),t) = W\frac{\partial S}{\partial z} + S\frac{\partial S}{\partial \phi_s}. \tag{B.16}$$

Using equation (B.5) and (B.6), one can remark that $\partial S/\partial z = S/c$ and $\partial S/\partial \phi_s = -W/c$. Introducing this in (B.16), the second derivation with time of ϕ_s along a characteristic curve is identically null,

$$\frac{d^2}{dt^2}\phi_s(Z(t),t) = 0. \tag{B.17}$$

Integrating twice with time, a linear dependence on time of ϕ_s is obtained,

$$\phi_s(Z(t),t) = \phi_{s0}(z_0) + S\left(z_0, \phi_{s0}(z_0)\right) t. \tag{B.18}$$

The value of ϕ_s along the characteristic curve is entirely determined by its inititial value and therefore by the initial condition ϕ_{s0}. It is now possible to compute the position with time of a characteristic curve. Introducing (B.18) in the second equation of (B.13) and integrating, a relation for the characteristic curves is obtained,

$$e^{-Z(t)/c} - e^{-z_0/c} = -\frac{S_{r0}}{c}(2\phi_{s0}(z_0) - 1)t - \frac{S_{r0}}{c}S\left(z_0, \phi_{s0}(z_0)\right) t^2, \tag{B.19}$$

$$\Leftrightarrow \quad Z(t) = z_0 - c\ln\left(1 - \frac{1}{c}W\left(z_0, \phi_{s0}(z_0)\right) t - \frac{S_{r0}}{c}e^{z_0/c}S\left(z_0, \phi_{s0}(z_0)\right) t^2\right), \tag{B.20}$$

and the characteristic curve is entirely determined by the value of the initial solution ϕ_{s0} in its origin position z_0. Finally the solution to system (B.13) is

$$\begin{cases} \phi_s(Z(t),t) &= \phi_{s0}(z_0) + S\left(z_0, \phi_{s0}(z_0)\right) t, \\ \\ Z(t) &= z_0 - c\ln\left(1 - \frac{1}{c}W\left(z_0, \phi_{s0}(z_0)\right) t - \frac{S_{r0}}{c}e^{z_0/c}S\left(z_0, \phi_{s0}(z_0)\right) t^2\right). \end{cases} \tag{B.21}$$

Equation (B.21) is a general solution for any initial condition. In the present configuration the initial solution (B.2) is a step of concentration with a discontinuity at z_i and represents an initial state where a pure layer of small particles is placed above a bed of only large particles. Figure B.1 shows the full solution for the case $z_i = 6$, and the derivation of this solution is presented below. According to the second equation of (B.13), the characteristic curves coming from $z_0 < z_i$ have a negative velocity and are going down. Conversely, those coming from $z_0 > z_i$ are going up. Therefore there is a rarefaction fan, where no characteristic curves are present.

For $z_0 < z_i$, $\phi_{s0}(z_0) = 0$, the equation of the characteristic curves are $Z(t) = z_0 - c\ln\left(1 + \frac{S_{r0}}{c}e^{z_0/c}t\right)$. Along these characteristics, $\phi_s(Z(t),t) = 0$. z_1 is defined as the characteristic curve at the bottom of the rarefaction zone (coming from z_i): $z_1(t) = z_i - c\ln\left(1 + \frac{S_{r0}}{c}e^{z_i/c}t\right)$. z_1 is the lower bound of the rarefaction zone. The time at which z_1 meets the bottom of the domain is called $t_1 = \frac{c}{S_{r0}}(1 - e^{-z_i/c})$ and corresponds to the time when the first small particle reaches the bottom.

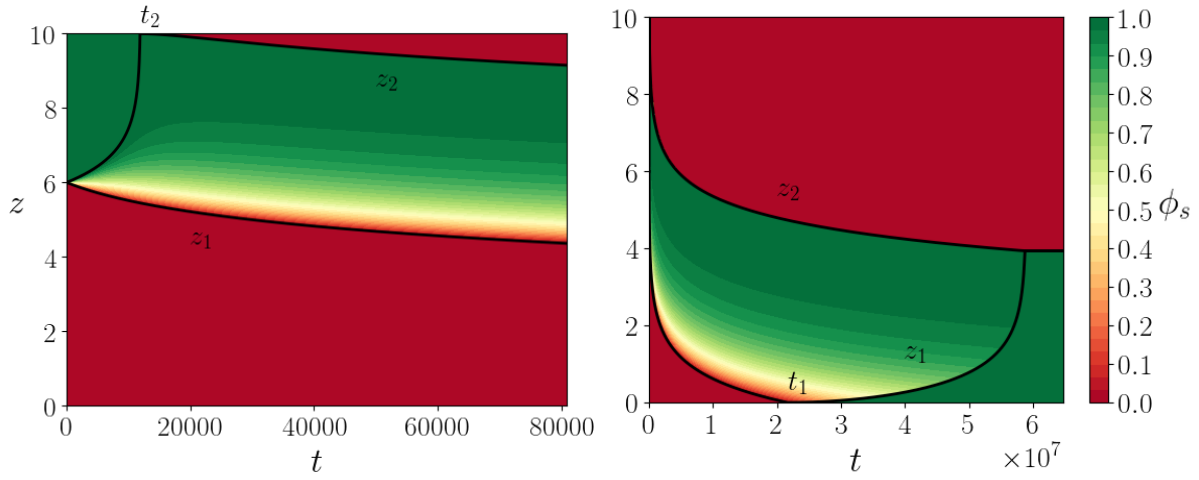

Figure B.1: Example of solution obtained by the method of characteristics. $z_i = 6$ (a) First time steps, (b) full solution.

For $z_0 > z_i$, $\phi_{s0}(z_0) = 1$, the equation of the characteristic curves are $Z(t) = z_0 - c\ln\left(1 - \frac{S_{r0}}{c}e^{z_0/c}t\right)$. Along these characteristics, $\phi_s(Z(t), t) = 1$. z_2 is defined as the characteristic curve coming from z_i: $z_2(t) = z_i - c\ln\left(1 - \frac{S_{r0}}{c}e^{z_i/c}t\right)$. z_2 is the upper bound of the rarefaction zone. The time at which z_2 meets the top of the domain is called $t_2 = \frac{c}{S_{r0}}(e^{-z_i/c} - e^{-H/c})$ and corresponds to the time when the first large particle reaches the top.

Once z_2 reaches the top of domain at t_2 the boundary condition (B.3) implies that $\phi(H, t_2)$ jumps from 1 to 0. A shock forms and the position of the shock must satisfy the Rankine-Hugoniot relation, which ensures the conservation of momentum through the shock

$$z_2' = -\frac{F_s(\phi^+) - F_s(\phi^-)}{\phi^+ - \phi^-}. \tag{B.22}$$

Above the shock $\phi^+ = 0$ and below ϕ^- is the solution in the rarefaction zone

$$z_2' = -S_{r0}e^{z_2/c}\left(1 - \phi_s(z_2, t)\right). \tag{B.23}$$

A similar expression applying the Rankine-Hugoniot relation is found for z_1 for $t > t_1$. For now, as no solution in the rarefaction has been computed, the shock evolution equation (B.23) cannot be solved. The solution in the rarefaction zone is now computed. The rarefaction zone is delimited by z_1 and z_2. Due to the discontinuity in the initial solution, no characteristic curves are present in the rarefaction wave ($z_1 \leq z \leq z_2$). In order to find a solution, it is considered that there is an infinity of characteristic curves coming from the point of discontinuity z_i, each of them being associated to a different initial value, noted $\bar{\phi}_{s0}$ and verifying $\phi_{s0}(z_c)^- = 0 \leq \bar{\phi}_{s0} \leq 1 = \phi_{s0}(z_c)^+$. In other words, for (z, t) in the rarefaction zone, one looks for a characteristic curve coming from z_i associated to an

initial value $\bar{\phi}_{s0}$ and verifying system (B.21)

$$\left\{\begin{array}{rcl} \phi_s(z,t) & = & \bar{\phi}_{s0} + S\left(z_i, \bar{\phi}_{s0}\right) t, \\ e^{-z/c} - e^{-z_i/c} & = & -\dfrac{S_{r0}}{c}(2\bar{\phi}_{s0} - 1)t - \dfrac{S_{r0}}{c} e^{z_i/c} S\left(z_i, \bar{\phi}_{s0}\right) t^2. \end{array}\right. \tag{B.24}$$

To compute the value of ϕ_s in the rarefaction zone with the first equation of (B.24), only the value of $\bar{\phi}_{s0}$ is missing. It is computed by an invertion of the second equation of (B.24) (quadratic equation and choosing the relevant solution)

$$\bar{\phi}_{s0} = \frac{1}{2} + \frac{c}{S_{r0}t} e^{-z_i/c} \left(1 - e^{(z_i - z)/c} \sqrt{1 + \left(\frac{S_{r0}t}{2c}\right)^2 e^{(z+z_i)/c}}\right). \tag{B.25}$$

Inserting (B.25) into the first equation of (B.24) the solution in the rarefaction zone is

$$\phi_s(z,t) = \frac{1}{2} - \frac{c}{S_{r0}t} e^{-z/c} + \frac{c}{S_{r0}t} e^{-(z+z_i)/(2c)} \sqrt{1 + \left(\frac{S_{r0}t}{2c}\right)^2 e^{(z+z_i)/c}}. \tag{B.26}$$

The equation of the shock (B.23) can now be solved. However due to the complex form of the solution in the rarefaction zone (B.26) the equation of the shock (B.23) is solved numerically. Finally the full solution is presented on figure B.1.

A long time asymptotic analysis can be performed on the solution in the rarefaction zone B.26. Remembering that the lower bound of the rarefaction zone is z_1 and focusing on the sqare root term in (B.26)

$$\left(\frac{S_{r0}t}{2c}\right)^2 e^{(z+z_i)/c} \geq \left(\frac{S_{r0}t}{2c}\right)^2 e^{(z_1+z_i)/c}. \tag{B.27}$$

The expression of z_1 is

$$z_1(t) = z_i - c \ln\left(1 + \frac{S_{r0}}{c} e^{z_i/c} t\right). \tag{B.28}$$

For $t \gg t_0 = c/S_{r0}e^{-z_i/c}$,

$$1 + \frac{S_{r0}}{c} e^{z_i/c} t \sim \frac{S_{r0}}{c} e^{z_i/c} t, \tag{B.29}$$

and the following expression is obtained for z_1

$$z_1(t) = -c \ln\left(\frac{S_{r0}t}{c}\right). \tag{B.30}$$

Replacing the latter expression of z_1 in (B.27),

$$\left(\frac{S_{r0}t}{2c}\right)^2 e^{(z+z_i)/c} \geq \frac{S_{r0}t}{4c} e^{z_i/c}, \tag{B.31}$$

and for $t \gg 4t_0 = 4c/S_{r0}e^{-z_i/c}$,

$$\left(\frac{S_{r0}t}{2c}\right)^2 e^{(z+z_i)/c} \geq \frac{S_{r0}t}{4c}e^{z_i/c} \gg 1. \tag{B.32}$$

Finally for $t \gg 4t_0$,

$$1 + \left(\frac{S_{r0}t}{2c}\right)^2 e^{(z+z_i)/c} \sim \left(\frac{S_{r0}t}{2c}\right)^2 e^{(z+z_i)/c}, \tag{B.33}$$

and the solution in the expansion fan simplifies to,

$$\phi_s(z,t) = 1 - \frac{c}{S_{r0}t}e^{-z/c}. \tag{B.34}$$

In the present configuration, $c \sim 1$, $S_{r0} \sim 1e-8$, $z_i \sim 10$. The simplified expression of ϕ_s is therefore valid for dimensionless times larger than $t_0 \sim 1e3$, time achieved very rapidly during simulations.

Appendix C

Derivation of the Rousseau et al. (subm) models for size segregation

In this appendix, the mutliphase flow and advection-diffusion models, based on the particle scale forces of Guillard et al. (2016) and Tripathi and Khakhar (2011b), are derived. This is part of Rousseau et al. (subm), and had been only slightly modified to be consitent with the notations used in this PhD.

C.1 Volume averaged multi-phase flow model

Following Jackson (1997, 2000), the mass and momentum balance equations for each class are given by

$$\frac{\partial \epsilon \rho^f \mathbf{u}^f}{\partial t} + \nabla . \left(\epsilon \rho^f \mathbf{u}^f \right), \tag{C.1}$$

$$\frac{\partial \Phi^i \rho^p \mathbf{u}^i}{\partial t} + \nabla . \left(\Phi^i \rho^p \mathbf{u}^i \right), \tag{C.2}$$

$$\frac{\partial \epsilon \rho^f \mathbf{u}^f}{\partial t} + \nabla . \left(\epsilon \rho^f \mathbf{u}^f \otimes \mathbf{u}^f \right) = \nabla . \mathbf{S}^f - \epsilon \rho^f \mathbf{g} - n_l \mathbf{f}_{f \to l} - n_s \mathbf{f}_{f \to s} \tag{C.3}$$

$$\frac{\partial \Phi^i \rho^p \mathbf{u}^i}{\partial t} + \nabla . \left(\Phi^i \rho^p \mathbf{u}^i \otimes \mathbf{u}^i \right) = \nabla . \mathbf{S}^i - \Phi^i \rho^p \mathbf{g} + n_i \mathbf{f}_{f \to i} + n_i \mathbf{f}_{\delta \to i}, \tag{C.4}$$

where f is the fluid and indices $i = l, s$ denote the large particle phase and the small particle phase respectively ($\delta = l$ if $i = s$ and $\delta = s$ if $i = l$). Φ^l and Φ^s are the volume fractions for the large and small grains and verify $\Phi^s + \Phi^l = \Phi$ where Φ is the volume fraction of the mixture, i.e. the total solid volume fraction. Consequently, the fluid volume fraction is $\epsilon = 1 - \Phi^l - \Phi^s$. $\mathbf{S}^k$ is the stress tensor associated with phase k with $k = l, s$ or f. They can be separated into pressure and shear stress contribution

$$\mathbf{S}^k = -p^k \mathbf{I} + \tau^k, \tag{C.5}$$

where τ^k is the shear stress tensor and p^k is the pressure of phase k. It should be noticed that for a solid phase, the static pressure arises from the enduring contacts between the particles. Thanks to the mixture model approaches (Morland, 1992), it can be assumed that each particle phase carries the total overburden pressure p^m according to their local volume fraction as

$$p^i = \frac{\Phi^i}{\Phi} P^p, \tag{C.6}$$

where P^p is the bulk granular pressure.

The momentum equations (C.3) and (C.4) contain two terms coming from the momentum exchange between the different phases: $n_i \mathbf{f}_{f\to i}$ and $n_i \mathbf{f}_{\delta\to i}$. The term $n_i \mathbf{f}_{f\to i}$ is the averaged value of the resultant forces exerted by the fluid on the particles of phase i. Jackson (2000) showed that for a collection of immersed particles, this interaction force can be written as

$$n_i \mathbf{f}_{f\to i} = -\Phi^i \nabla p^f + n_i \mathbf{f}_d^{f\to i}, \tag{C.7}$$

where $\Phi^i \nabla p^f$ is the buoyancy force exerted by the fluid phase on the particles and $n_i \mathbf{f}_d^{f\to i}$ is the particle averaged viscous drag force between the particles and the fluid phase. The term $n_i \mathbf{f}_{\delta\to i}$ is the averaged value of all interacting forces between large and small particle phases. It can be directly expressed in 3D from the local segregation force of Tripathi and Khakhar (2013) and Guillard et al. (2016).

Therefore, the developed model is general and can be applied to 3D configurations. For simplicity and for the purpose of the present study, the model will be only developed for a 1D uniform flow.

C.2 Simplified 1D vertical multi-phase flow model

The multi-phase flow model (equations C.1 to C.4) is simplified by considering a uniform flow in the streamwise direction. From now, all the variables only depend on the vertical position z. Therefore, the spatially averaged velocity of the phase k can be written as $\mathbf{u}^k = u^k(z)\mathbf{e}_x + w^k(z)\mathbf{e}_z$. The mass conservation equations simplify to

$$\frac{\partial \epsilon}{\partial t} + \frac{\partial \epsilon w^f}{\partial z} = 0 \qquad \text{and} \qquad \frac{\partial \Phi^i}{\partial t} + \frac{\partial \Phi^i w^i}{\partial z} = 0, \tag{C.8}$$

and the momentum balance equations in the vertical direction are:

$$\rho^f \left[\frac{\partial \epsilon w^f}{\partial t} + \frac{\partial \epsilon w^f w^f}{\partial z} \right] = -\epsilon \frac{\partial p^f}{\partial z} - \epsilon \rho^f g \cos\alpha - n_l < f_d^{f\to l} > - n_s < f_d^{f\to s} >, \tag{C.9}$$

$$\rho^p \left[\frac{\partial \Phi^l w^l}{\partial t} + \frac{\partial \Phi^l w^l w^l}{\partial z} \right] = -\frac{\partial p^l}{\partial z} - \Phi^l \frac{\partial p^f}{\partial z} - \Phi^l \rho^p g \cos\alpha + n_l < f_d^{f\to l} > + n_l < f_{s\to l} >, \tag{C.10}$$

$$\rho^p \left[\frac{\partial \Phi^s w^s}{\partial t} + \frac{\partial \Phi^s w^s w^s}{\partial z} \right] = -\frac{\partial p^s}{\partial z} - \Phi^s \frac{\partial p^f}{\partial z} - \Phi^s \rho^p g \cos\alpha + n_s < f_d^{f\to s} > + n_s < f_{l\to s} > . \tag{C.11}$$

In the two last equations, the solid pressures p^l and p^s are given by equation (C.6). To solve these equations, it is necessary to prescribe closures for the spatially averaged fluid/grain interaction and grain-grain interactions, and for the granular and fluid pressures.

Considering the fluid-grain interaction, both small and large granular phases interact with the fluid phase through $\Phi^i \nabla p^f$ and the drag force $n_i \mathbf{f}_d^{f\to i}$. For an assembly of particles, the spatial averaging of the vertical total drag force applied by the fluid gives

$$n_l < f_d^{f\to i} >= \frac{\Phi^i \rho^p}{t_i} \left(w^f - w^i \right), \tag{C.12}$$

where $t_i = \rho^p d_i^2 (1-\Phi)^3 / 18\eta^f$ is the particle response time and d_i is the particle diameter of phase i. The factor $(1-\Phi)^3$ is a correction proposed by Richardson and Zaki (1954) to take into account hindrance effects. Since the drag is linear, the spatial averaging is simply the drag force applied on one particle, given by $F_d^f = 3\pi\eta^f d_i (w^i - w^f)$, multiplied by the number of particles per unit volume $n_i = \Phi^i / V^i$ (Jackson, 2000), where V^i is the volume of a single large particle.

The granular phases also interact with each other and the grain-grain interaction closure should be prescribed in the model. For a single large grain in a bath of small particles, it has been shown in in the introduction chapter 1.3.1 that small particles exert three forces on a large intruder. The granular buoyancy force is included in the pressure gradient term. Therefore, the granular interaction term is reduced to the segregation force and the granular drag force,

$$f_{s\to l} = F_d + F_{seg}. \tag{C.13}$$

To extend these forces to a collection of large particles, the interaction force $f_{s\to l}$ is spatially averaged. Since this force is linear, it amounts to multiplying $f_{s\to l}$ by the number of large particles per unit volume $n_l = 6\Phi^l / \pi d_l^3$. Therefore, the total solid interaction force exerted by the small particles on the large ones is given by

$$n_l < f_{s\to l} >= \frac{\Phi^l \rho^p}{t_{ls}} \left(w^s - w^l \right) + \Phi^l \mathcal{F}'(\mu) \frac{\partial P^p}{\partial z}, \tag{C.14}$$

where $t_{ls} = \rho^p d_l^2 / 6c\eta^p$ is the particle response time for the drag force between small and large particles and $\mathcal{F}'(\mu) = \mathcal{F}(\mu) - \dfrac{1}{\Phi}$ with $\mathcal{F}(\mu)$ is the segregation function proposed by Guillard et al. (2016). According to the Newton's third law, the force exerted by the large particles on the small ones (equation C.11) is

$$n_s < f_{l\to s} >= -n_l < f_{s\to l} > . \tag{C.15}$$

The solid mixture phase is made of both particle phases and is noted with $i = m$. Its momentum balance is obtained by summing (C.10) and (C.11). Since the mixture phase does not distinguish between small and large particles, the solid interaction forces should not appear in this equation. Equation (C.15) ensures that these forces vanish when developing the mixture momentum equation.

The proposed volume-averaged multi-phase flow model describes size segregation of a bi-disperse mixture immersed in a fluid. This represents an improvement upon the model of Thornton et al. (2006), which was based on semi-empirical parametrisation of the interparticle forces between small and large particles. The present model provides closures based on forces applied on a single particle, and bridges the gap between granular scale processes and continuum modelling in size segregation. This important result will be used in the following to derive an advection-diffusion model for size segregation.

C.3 Derivation of the advection-diffusion model

A classical continuum approach to model size segregation is the advection-diffusion model (Dolgunin and Ukolov, 1995; Gray and Thornton, 2005). These models can be derived from the multicomponent mixture theory (Thornton et al., 2006; Gray and Ancey, 2011) by substituting the percolation velocity of one particle-size into the mass conservation equation. The advection and diffusion coefficients can be modelled using experimental and theoretical closures (Dolgunin et al., 1998; Van der Vaart et al., 2015; Ferdowsi et al., 2017; Cai et al., 2019) or can be derived as a simplification from the continuum model of Thornton et al. (2006) and Gray and Chugunov (2006). In the present section, the multi-phase model developed in the previous section (equations C.9 to C.11) makes it possible to derive an advection-diffusion model similar to Thornton et al. (2006) and Gray and Chugunov (2006), with advection and diffusion coefficients depending on the segregation and the drag forces (Guillard et al., 2016; Tripathi and Khakhar, 2013) determined in independent idealised configurations.

Combining equations (C.11), (C.12), (C.14) and (C.15), the momentum balance of small particles can be written as:

$$\rho^p\left[\frac{\partial \Phi^s w^s}{\partial t}+\frac{\partial \Phi^s w^s w^s}{\partial z}\right]=-\frac{\partial p^s}{\partial z}-\Phi^s\frac{\partial p^f}{\partial z}-\Phi^s\rho^p g\cos\alpha+\frac{\rho^p\Phi^s}{t_s}\left(w^f-w^s\right)$$
$$-\frac{\rho^p\Phi}{t_{ls}}\left(w^s-w^m\right)+\Phi^l\mathcal{F}'(\mu)\frac{\partial P^p}{\partial z}. \quad \text{(C.16)}$$

The total volume fraction $\Phi = \Phi^s + \Phi^l$ is assumed to be constant and equal to $\Phi_{max} = 0.61$ since particle velocity fluctuations are small. For a deposited bed, the particle momentum balance in the wall-normal direction reduces to a hydrostatic pressure distribution for both

the fluid and the particle phases (Chauchat, 2018):

$$\frac{\partial p^f}{\partial z} = -\rho^f g \cos\alpha \quad \text{and} \quad \frac{\partial P^p}{\partial z} = -\Phi\left(\rho^p - \rho^f\right) g \cos\alpha. \tag{C.17}$$

Assuming a constant mixture solid phase volume fraction, the pressure gradient can be integrated to give the pressure distributions:

$$p^f = \rho^f g \cos\alpha\,(h - z) \quad \text{and} \quad p^m = \Phi\left(\rho^p - \rho^f\right) g \cos\alpha\,(h - z)\,. \tag{C.18}$$

Following Thornton et al. (2006), the volume fraction per unit granular volume is introduced as $\phi^i = \Phi^i/\Phi$. This notation is more convenient since it ensures $\phi^s + \phi^l = 1$. Using equation (C.6), the momentum equation (C.16) for small particles is rewritten as follows:

$$\Phi\rho^p\left[\frac{\partial \phi^s w^s}{\partial t} + \frac{\partial \phi^s w^s w^s}{\partial z}\right] = -p^m\frac{\partial \phi^s}{\partial z} + \frac{\rho^p\phi^s\Phi}{t_s}\left(w^f - w^s\right) - \frac{\rho^p\Phi}{t_{ls}}\left(w^s - w^m\right) + \phi^l\Phi\mathcal{F}'(\mu)\frac{\partial p^m}{\partial z}. \tag{C.19}$$

Using the same dimensionless variables proposed in equation (4.7) for a single intruder, the equation (C.19) is made dimensionless as follows:

$$\frac{\partial \phi^s\tilde{w}^s}{\partial \tilde{t}} + \frac{\partial \phi^s\tilde{w}^s\tilde{w}^s}{\partial \tilde{z}} = -\frac{\tilde{p}^m}{\Phi}\frac{\partial \phi^s}{\partial \tilde{z}} + \frac{\phi^s}{St^f}\left(\tilde{w}^f - \tilde{w}^s\right) - \frac{(\tilde{w}^s - \tilde{w}^m)}{St^p} + \phi^l\mathcal{F}'(\mu)\frac{\partial \tilde{p}^m}{\partial \tilde{z}}. \tag{C.20}$$

Rousseau et al. (subm) showed that $St^f >> St^p$ in the granular bed and therefore the fluid drag force can be neglected. Furthermore, assuming a quasi-steady state and neglecting inertial terms, equation (C.20) can be rewritten as

$$-\frac{\tilde{p}^m}{\Phi}\frac{\partial \phi^s}{\partial \tilde{z}} - \frac{(\tilde{w}^s - \tilde{w}^m)}{St^p} + \phi^l\mathcal{F}'(\mu)\frac{\partial \tilde{p}^m}{\partial \tilde{z}} = 0, \tag{C.21}$$

from which, assuming $w^m = 0$ (Thornton et al., 2006), the flux of small particles can be expressed as

$$\phi^s\tilde{w}^s = -\frac{\phi^s}{\Phi}\tilde{p}^m St^p\frac{\partial \phi^s}{\partial \tilde{z}} + \phi^l\phi^s\mathcal{F}'(\mu)St^p\frac{\partial \tilde{p}^m}{\partial \tilde{z}}. \tag{C.22}$$

Equation (C.22) is then substituted in the mass conservation equation (C.8) to obtain the following advection-diffusion equation for the percolation of small particles:

$$\frac{\partial \phi^s}{\partial \tilde{t}} + \frac{\partial}{\partial \tilde{z}}\left(\phi^l\phi^s S_r\right) = \frac{\partial}{\partial \tilde{z}}\left(D\frac{\partial \phi^s}{\partial \tilde{z}}\right), \tag{C.23}$$

with

$$S_r = \mathcal{F}'(\mu)St^p\frac{\partial \tilde{p}^m}{\partial \tilde{z}} \quad \text{and} \quad D = \frac{\phi^s\tilde{p}^m St^p}{\Phi}, \tag{C.24}$$

Since the pressure gradient is negative, S_r is negative which ensures a downward flux for the small particle phase.

Bibliography

ACI committee 238 (2008). ACI. Report on measurements of workability and rheology of fresh concrete. Technical Report ACI 238. 1R-08., Farmington Hills: American Concrete Institute.

Ancey, C. (2020). Bedload transport: A walk between randomness and determinism. Part 2. Challenges and prospects. *Journal of Hydraulic Research*, 58(1):18–33.

Ancey, C., Davison, A. C., Böhm, T., Jodeau, M., and Frey, P. (2008). Entrainment and motion of coarse particles in a shallow water stream down a steep slope. *Journal of Fluid Mechanics*, 595:83–114.

Andreotti, B., Forterre, Y., and Pouliquen, O. (2013). Granular Media: Between Fluid and Solid. /core/books/granular-media/E1D234B8D868A9856C9E95B4750470AB.

Bacchi, V., Recking, A., Eckert, N., Frey, P., Piton, G., and Naaim, M. (2014). The effects of kinetic sorting on sediment mobility on steep slopes. *Earth Surface Processes and Landforms*, 39(8):1075–1086.

Bagnold, R. A. (1956). The flow of cohesionless grains in fluids. *Philosophical Transactions of the Royal Society of London. Series A, Mathematical and Physical Sciences*, 249(964):235–297.

Bathurst, J. (2007). Effect of Coarse Surface Layer on Bed-Load Transport. *Journal of Hydraulic Engineering*, 133(11):1192–1205.

Bigillon, F. (2001). *Etude Du Mouvement Bidimensionnel d'une Particule Dans Un Courant d'eau Sur Forte Pente*. These de doctorat, Grenoble 1.

Bouzid, M., Trulsson, M., Claudin, P., Clément, E., and Andreotti, B. (2013). Nonlocal rheology of granular flows across yield conditions. *Physical Review Letters*, 111(23):238301.

Bridgwater, J., Foo, W., and Stephens, D. (1985). Particle mixing and segregation in failure zones—theory and experiment. *Powder Technology*, 41(2):147–158.

Bridgwater, J. and Ingram, N. (1971). Rate of Spontaneous Inter-Particle Percolation. *Transactions of the Institution of Chemical Engineers*, 49(3):163–169.

Cai, R., Xiao, H., Zheng, J., and Zhao, Y. (2019). Diffusion of size bidisperse spheres in dense granular shear flow. *Physical Review. E*, 99(3-1):032902.

Campbell, C. S. (1997). Self-diffusion in granular shear flows. *Journal of Fluid Mechanics*, 348:85–101.

Capart, H. and Fraccarollo, L. (2011). Transport layer structure in intense bed-load. *Geophysical Research Letters*, 38(20).

Carson, J. W. (1988). Overcoming Particle Segregation in the Pharmaceutical and Cosmetics Industries. *Drug Development and Industrial Pharmacy*, 14(18):2749–2758.

Cassar, C., Nicolas, M., and Pouliquen, O. (2005). Submarine granular flows down inclined planes. *Physics of Fluids*, 17(10):103301.

Charru, F., Mouilleron, H., and Eiff, O. (2004). Erosion and deposition of particles on a bed sheared by a viscous flow. *Journal of Fluid Mechanics*, 519:55–80.

Chassagne, R., Frey, P., Maurin, R., and Chauchat, J. (2020a). Mobility of bidisperse mixtures during bedload transport. *Physical Review Fluids*, 5:114307.

Chassagne, R., Maurin, R., Chauchat, J., Gray, J. M. N. T., and Frey, P. (2020b). Discrete and continuum modelling of grain size segregation during bedload transport. *Journal of Fluid Mechanics*, 895:A30.

Chauchat, J. (2018). A comprehensive two-phase flow model for unidirectional sheet-flows. *Journal of Hydraulic Research*, 56(1):15–28.

Chedeville, C. and Roche, O. (2014). Autofluidization of pyroclastic flows propagating on rough substrates as shown by laboratory experiments. *Journal of Geophysical Research: Solid Earth*, 119(3):1764–1776.

Courrech du Pont, S., Gondret, P., Perrin, B., and Rabaud, M. (2003). Granular Avalanches in Fluids. *Physical Review Letters*, 90(4):044301.

Cumberland, D. J. and Crawford, R. J. (1987). *The Packing of Particles*. Elsevier.

da Cruz, F., Emam, S., Prochnow, M., Roux, J.-N., and Chevoir, F. (2005). Rheophysics of dense granular materials: Discrete simulation of plane shear flows. *Physical Review E*, 72(2):021309.

Dalla Valle, J. M. (1943). *Micromeritics: The Technology of Fine Particles*. Pitman.

Dhont, B. and Ancey, C. (2018). Are Bedload Transport Pulses in Gravel Bed Rivers Created by Bar Migration or Sediment Waves? *Geophysical Research Letters*, 45(11):5501–5508.

Ding, Y., Gravish, N., and Goldman, D. I. (2011). Drag Induced Lift in Granular Media. *Physical Review Letters*, 106(2):028001.

Dolgunin, V. N., Kudy, A. N., and Ukolov, A. A. (1998). Development of the model of segregation of particles undergoing granular flow down an inclined chute. *Powder Technology*, 96(3):211–218.

Dolgunin, V. N. and Ukolov, A. A. (1995). Segregation modeling of particle rapid gravity flow. *Powder Technology*, 83(2):95–103.

Drake, T. G. and Calantoni, J. (2001). Discrete particle model for sheet flow sediment transport in the nearshore. *Journal of Geophysical Research: Oceans*, 106(C9):19859–19868.

du Boys, P. (1879). Le Rhône et les rivières à lit affouillable - Étude du régime du Rhône et de l'action exercée par les eaux sur un lit à fonds de graviers indéfiniment affouillable. *Annales des Ponts et Chaussées*, 49:141–95.

Dudill, A. (2016). *Étude Expérimentale de La Ségrégation En Transport Solide Par Charriage*. These de doctorat, Université Grenoble Alpes (ComUE) et University of British Columbia.

Dudill, A., Frey, P., and Church, M. (2017). Infiltration of fine sediment into a coarse mobile bed: A phenomenological study. *Earth Surface Processes and Landforms*, 42(8):1171–1185.

Dudill, A., Lafaye de Micheaux, H., Frey, P., and Church, M. (2018). Introducing Finer Grains Into Bedload: The Transition to a New Equilibrium. *Journal of Geophysical Research: Earth Surface*, 123(10):2602–2619.

Durán, O., Andreotti, B., and Claudin, P. (2012). Numerical simulation of turbulent sediment transport, from bed load to saltation. *Physics of Fluids*, 24(10):103306.

Edwards, A. N., Viroulet, S., Kokelaar, B. P., and Gray, J. M. N. T. (2017). Formation of levees, troughs and elevated channels by avalanches on erodible slopes. *Journal of Fluid Mechanics*, 823:278–315.

Egiazaroff, I. V. (1965). Calculation of Nonuniform Sediment Concentrations. *Journal of the Hydraulics Division*, 91(4):225–247.

Einstein, A. (1906). Eine neue Bestimmung der Moleküldimensionen. *Annalen der Physik*, 324(2):289–306.

Einstein, H. (1942). Formulas for the transport of bed sediment. *Transactions of the American Society of Civil Engineers*, 107:561–574.

Einstein, H. (1950). The Bed-Load Function for Sediment Transportation in Open Channel Flows. Technical Report 156389, United States Department of Agriculture, Economic Research Service.

Fan, Y. and Hill, K. M. (2015). Shear-induced segregation of particles by material density. *Physical Review E*, 92(2):022211.

Fan, Y., Schlick, C. P., Umbanhowar, P. B., Ottino, J. M., and Lueptow, R. M. (2014). Modelling size segregation of granular materials: The roles of segregation, advection and diffusion. *Journal of Fluid Mechanics*, 741:252–279.

Farin, M., Mangeney, A., and Roche, O. (2014). Fundamental changes of granular flow dynamics, deposition, and erosion processes at high slope angles: Insights from laboratory experiments. *Journal of Geophysical Research: Earth Surface*, 119(3):504–532.

Ferdowsi, B., Ortiz, C. P., Houssais, M., and Jerolmack, D. J. (2017). River-bed armouring as a granular segregation phenomenon. *Nature Communications*, 8(1):1363.

Fernandez-Luque, R. and Van Beek, R. (1976). Erosion And Transport Of Bed-Load Sediment. *Journal of Hydraulic Research*, 14(2):127–144.

Forterre, Y. and Pouliquen, O. (2008). Flows of Dense Granular Media. *Annual Review of Fluid Mechanics*, 40(1):1–24.

Frey, P. (2014). Particle velocity and concentration profiles in bedload experiments on a steep slope. *Earth Surface Processes and Landforms*, 39(5):646–655.

Frey, P. and Church, M. (2009). How River Beds Move. *Science*, 325(5947):1509–1510.

Frey, P. and Church, M. (2011). Bedload: A granular phenomenon. *Earth Surface Processes and Landforms*, 36(1):58–69.

Frey, P., Lafaye de Micheaux, H., Bel, C., Maurin, R., Rorsman, K., Martin, T., and Ducottet, C. (2020). Experiments on grain size segregation in bedload transport on a steep slope. *Advances in Water Resources*, 136:103478.

Fry, A. M., Umbanhowar, P. B., Ottino, J. M., and Lueptow, R. M. (2018). Effect of pressure on segregation in granular shear flows. *Physical Review E*, 97(6):062906.

Furbish, D. J., Haff, P. K., Roseberry, J. C., and Schmeeckle, M. W. (2012). A probabilistic description of the bed load sediment flux: 1. Theory. *Journal of Geophysical Research: Earth Surface*, 117:F03031.

Gajjar, P. and Gray, J. M. N. T. (2014). Asymmetric flux models for particle-size segregation in granular avalanches. *Journal of Fluid Mechanics*, 757:297–329.

GDR MiDi (2004). On dense granular flows. *The European Physical Journal E*, 14(4):341–365.

Gilbert, G. K. (1914). The transportation of débris by running water. *USGS Professional paper 86*.

Godunov, S. (1959). A difference method for numerical calculation of discontinuous solutions of the equations of hydrodynamics. *Mat. Sb. (N.S.)*, 47 (89)(3):271–306.

Goldhirsch, I. (2010). Stress, stress asymmetry and couple stress: From discrete particles to continuous fields. *Granular Matter*, 12(3):239–252.

Golick, L. A. and Daniels, K. E. (2009). Mixing and segregation rates in sheared granular materials. *Physical Review E*, 80(4):042301.

Gray, J. M. N. T. (2018). Particle Segregation in Dense Granular Flows. *Annual Review of Fluid Mechanics*, 50(1):407–433.

Gray, J. M. N. T. and Ancey, C. (2011). Multi-component particle-size segregation in shallow granular avalanches. *Journal of Fluid Mechanics*, 678:535–588.

Gray, J. M. N. T. and Chugunov, V. A. (2006). Particle-size segregation and diffusive remixing in shallow granular avalanches. *Journal of Fluid Mechanics*, 569:365–398.

Gray, J. M. N. T. and Thornton, A. R. (2005). A theory for particle size segregation in shallow granular free-surface flows. *Proceedings of the Royal Society A: Mathematical, Physical and Engineering Sciences*, 461(2057):1447–1473.

Guazzelli, É. and Morris, J. F. (2011). *A Physical Introduction to Suspension Dynamics*. Cambridge University Press.

Guillard, F., Forterre, Y., and Pouliquen, O. (2014). Lift forces in granular media. *Physics of Fluids*, 26(4):043301.

Guillard, F., Forterre, Y., and Pouliquen, O. (2016). Scaling laws for segregation forces in dense sheared granular flows. *Journal of Fluid Mechanics*, 807:R1.

Guo, Y., Wu, J., Wang, C., and Zhang, F. (2020). Study on the influence of the shape and size of coarse aggregate on the strength of concrete. *IOP Conference Series: Materials Science and Engineering*, 780:042008.

Guyon, E., Hulin, J.-P., and Petit, L. (2001). *Hydrodynamique physique*. EDP Sciences.

Hergault, V. (2011). *Etude Microstructurelle Du Transport Par Charriage de Mélanges Bidisperses à Forte Pente*. These de doctorat, Grenoble.

Hergault, V., Frey, P., Métivier, F., Barat, C., Ducottet, C., Böhm, T., and Ancey, C. (2010). Image processing for the study of bedload transport of two-size spherical particles in a supercritical flow. *Experiments in Fluids*, 49(5):1095–1107.

Houssais, M. and Lajeunesse, E. (2012). Bedload transport of a bimodal sediment bed. *Journal of Geophysical Research: Earth Surface*, 117:F04015.

Houssais, M., Ortiz, C. P., Durian, D. J., and Jerolmack, D. J. (2015). Onset of sediment transport is a continuous transition driven by fluid shear and granular creep. *Nature Communications*, 6:6527.

Hsu, T.-J. and Liu, P. L.-F. (2004). Toward modeling turbulent suspension of sand in the nearshore. *Journal of Geophysical Research: Oceans*, 109:C06018.

Iverson, R. M., Logan, M., LaHusen, R. G., and Berti, M. (2010). The perfect debris flow? Aggregated results from 28 large-scale experiments. *Journal of Geophysical Research: Earth Surface*, 115:F03005.

Jackson, R. (1997). Locally averaged equations of motion for a mixture of identical spherical particles and a Newtonian fluid. *Chemical Engineering Science*, 52(15):2457–2469.

Jackson, R. (2000). *The Dynamics of Fluidized Particles*. Cambridge University Press.

Jenkins, J. T. and Hanes, D. M. (1998). Collisional sheet flows of sediment driven by a turbulent fluid. *Journal of Fluid Mechanics*, 370:29–52.

Jenkins, J. T. and Mancini, F. (1989). Kinetic theory for binary mixtures of smooth, nearly elastic spheres. *Physics of Fluids A: Fluid Dynamics*, 1(12):2050–2057.

Jones, R. P., Isner, A. B., Xiao, H., Ottino, J. M., Umbanhowar, P. B., and Lueptow, R. M. (2018). Asymmetric concentration dependence of segregation fluxes in granular flows. *Physical Review Fluids*, 3:094304.

Jop, P., Forterre, Y., and Pouliquen, O. (2005). Crucial role of sidewalls in granular surface flows: Consequences for the rheology. *Journal of Fluid Mechanics*, 541:167–192.

Jop, P., Forterre, Y., and Pouliquen, O. (2006). A constitutive law for dense granular flows. *Nature*, 441(7094):727–730.

Kalinske, A. A. (1947). Movement of sediment as bed load in rivers. *Eos, Transactions American Geophysical Union*, 28(4):615–620.

Kamrin, K. and Koval, G. (2012). Nonlocal Constitutive Relation for Steady Granular Flow. *Physical Review Letters*, 108(17):178301.

Khakhar, D. V., McCarthy, J. J., and Ottino, J. M. (1999). Mixing and segregation of granular materials in chute flows. *Chaos: An Interdisciplinary Journal of Nonlinear Science*, 9(3):594–610.

Komatsu, T. S., Inagaki, S., Nakagawa, N., and Nasuno, S. (2001). Creep Motion in a Granular Pile Exhibiting Steady Surface Flow. *Physical Review Letters*, 86(9):1757–1760.

Lafaye de Micheaux, H., Ducottet, C., and Frey, P. (2018). Multi-model particle filter-based tracking with switching dynamical state to study bedload transport. *Machine Vision and Applications*, 29(5):735–747.

Lai, Z., Vallejo, L. E., Zhou, W., Ma, G., Espitia, J. M., Caicedo, B., and Chang, X. (2017). Collapse of Granular Columns With Fractal Particle Size Distribution: Implications for Understanding the Role of Small Particles in Granular Flows. *Geophysical Research Letters*, 44:12,181–12,189.

Lajeunesse, E., Malverti, L., and Charru, F. (2010). Bed load transport in turbulent flow at the grain scale: Experiments and modeling. *Journal of Geophysical Research: Earth Surface*, 115:F04001.

Lavelle, J. W. and Mofjeld, H. O. (1987). Do Critical Stresses for Incipient Motion and Erosion Really Exist? *Journal of Hydraulic Engineering*, 113(3):370–385.

LeVeque, R. J. (2002). *Finite Volume Methods for Hyperbolic Problems*. Cambridge Texts in Applied Mathematics. Cambridge University Press, Cambridge.

Li, L. and Sawamoto, M. (1995). Multi-Phase Model on Sediment Transport in Sheet-Flow Regime Under Oscillatory Flow. *Coastal Engineering in Japan*, 38(2):157–178.

Linares-Guerrero, E., Goujon, C., and Zenit, R. (2007). Increased mobility of bidisperse granular avalanches. *Journal of Fluid Mechanics*, 593:475–504.

López de Haro, M., Cohen, E. G. D., and Kincaid, J. M. (1983). The Enskog theory for multicomponent mixtures. I. Linear transport theory. *The Journal of Chemical Physics*, 78(5):2746–2759.

Mangeney, A., Roche, O., Hungr, O., Mangold, N., Faccanoni, G., and Lucas, A. (2010). Erosion and mobility in granular collapse over sloping beds. *Journal of Geophysical Research: Earth Surface*, 115:F03040.

Marks, B., Rognon, P., and Einav, I. (2012). Grainsize dynamics of polydisperse granular segregation down inclined planes. *Journal of Fluid Mechanics*, 690:499–511.

Maurin, R. (2015). *Investigation of Granular Behavior in Bedload Transport Using a Eulerian-Lagragian Model*. PhD thesis, Univ. Grenoble Alpes.

Maurin, R., Chauchat, J., Chareyre, B., and Frey, P. (2015). A minimal coupled fluid-discrete element model for bedload transport. *Physics of Fluids*, 27(11):113302.

Maurin, R., Chauchat, J., and Frey, P. (2016). Dense granular flow rheology in turbulent bedload transport. *Journal of Fluid Mechanics*, 804:490–512.

Maurin, R., Chauchat, J., and Frey, P. (2018). Revisiting slope influence in turbulent bedload transport: Consequences for vertical flow structure and transport rate scaling. *Journal of Fluid Mechanics*, 839:135–156.

May, L. B. H., Golick, L. A., Phillips, K. C., Shearer, M., and Daniels, K. E. (2010). Shear-driven size segregation of granular materials: Modeling and experiment. *Physical Review E*, 81(5):051301.

Meyer-Peter, E. and Müller, R. (1948). Formulas for Bed-Load transport. *IAHSR 2nd meeting, Stockholm, appendix 2*.

Middleton, G. V. (1970). Experimental studies related to problems of flysch sedimentation. In *Flysch Sedimentology in North America*, number 7 in Special Paper, pages 253–72. Business and Economics Science Ltd., j. lajoie edition.

Morland, L. W. (1992). Flow of viscous fluids through a porous deformable matrix. *Surveys in Geophysics*, 13(3):209–268.

Navarrete, I. and Lopez, M. (2017). Understanding the relationship between the segregation of concrete and coarse aggregate density and size. *Construction and Building Materials*, 149:741–748.

Ottino, J. M. and Khakhar, D. V. (2000). Mixing and Segregation of Granular Materials. *Annual Review of Fluid Mechanics*, 32(1):55–91.

Ouriemi, M., Aussillous, P., and Guazzelli, E. (2009). Sediment dynamics. Part 1. Bed-load transport by laminar shearing flows. *Journal of Fluid Mechanics*, 636:295–319.

Pähtz, T., Clark, A. H., Valyrakis, M., and Durán, O. (2020). The Physics of Sediment Transport Initiation, Cessation, and Entrainment Across Aeolian and Fluvial Environments. *Reviews of Geophysics*, 58(1):e2019RG000679.

Pähtz, T. and Durán, O. (2020). Unification of Aeolian and Fluvial Sediment Transport Rate from Granular Physics. *Physical Review Letters*, 124(16):168001.

Paintal, A. S. (1971). Concept Of Critical Shear Stress In Loose Boundary Open Channels. *Journal of Hydraulic Research*, 9(1):91–113.

Parker, G., Klingeman, P. C., and McLean, D. G. (1982). Bedload and size distribution in paved gravel-bed streams. *Journal of the Hydraulics Division - ASCE*, 108(HY4):544–571.

Parker, G., Paola, C., and Leclair, S. (2000). Probabilistic Exner Sediment Continuity Equation for Mixtures with No Active Layer. *Journal of Hydraulic Engineering*, 126(11):818–826.

Patankar, S. V. (1980). *Numerical Heat Transfer and Fluid Flow*. Hemisphere Publishing Corporation.

Perera, V., Jackson, A. P., Asphaug, E., and Ballouz, R.-L. (2016). The spherical Brazil Nut Effect and its significance to asteroids. *Icarus*, 278:194–203.

Perrin, H., Clavaud, C., Wyart, M., Metzger, B., and Forterre, Y. (2019). Interparticle Friction Leads to Nonmonotonic Flow Curves and Hysteresis in Viscous Suspensions. *Physical Review X*, 9(3):031027.

Phillips, J. C., Hogg, A. J., Kerswell, R. R., and Thomas, N. H. (2006). Enhanced mobility of granular mixtures of fine and coarse particles. *Earth and Planetary Science Letters*, 246(3):466–480.

Pollard, B. L. and Henein, H. (1989). Kinetics of Radial Segregation of Different Sized Irregular Particles in Rotary Cylinders. *Canadian Metallurgical Quarterly*, 28(1):29–40.

Pouliquen, O., Cassar, C., Jop, P., Forterre, Y., and Nicolas, M. (2006). Flow of dense granular material: Towards simple constitutive laws. *Journal of Statistical Mechanics: Theory and Experiment*, 2006(07):P07020.

Powell, D. M., Reid, I., and Laronne, J. B. (2001). Evolution of bed load grain size distribution with increasing flow strength and the effect of flow duration on the caliber of bed load sediment yield in ephemeral gravel bed rivers. *Water Resources Research*, 37(5):1463–1474.

Prandtl, L. (1926). Bericht über neuere Turbulenzforschung. *Hydraulische Probleme. Vorträge Hydrauliktagung Göttingen*, 5:1–13.

Recking, A. (2013). An analysis of nonlinearity effects on bed load transport prediction. *Journal of Geophysical Research: Earth Surface*, 118(3):1264–1281.

Recking, A., Frey, P., Paquier, A., and Belleudy, P. (2009). An experimental investigation of mechanisms involved in bed load sheet production and migration. *Journal of Geophysical Research: Earth Surface*, 114:F03010.

Recking, A., Richard, D., and Degoutte, G. (2013). *Torrents et Rivières de Montagne*. Savoir Faire. Quae edition.

Revil-Baudard, T. and Chauchat, J. (2013). A two-phase model for sheet flow regime based on dense granular flow rheology. *Journal of Geophysical Research: Oceans*, 118(2):619–634.

Richardson, J. F. and Zaki, W. N. (1954). The sedimentation of a suspension of uniform spheres under conditions of viscous flow. *Chemical Engineering Science*, 3(2):65–73.

Rickenmann, D. (1991). Hyperconcentrated Flow and Sediment Transport at Steep Slopes. *Journal of Hydraulic Engineering*, 117(11):1419–1439.

Rognon, P. G., Roux, J., Naaïm, M., and Chevoir, F. (2007). Dense flows of bidisperse assemblies of disks down an inclined plane. *Physics of Fluids*, 19(5):058101.

Rousseau, H., Chassagne, R., Chauchat, J., Maurin, R., and Frey, P. (subm). Bridging the gap between particle-scale forces and continuum modelling of size segregation: Application to bedload transport. *under review in Journal of Fluid Mechanics*.

Roux, J. and Combe, G. (2002). Quasistatic rheology and the origins of strain. *Comptes Rendus Physique*, 3(2):131–140.

Savage, S. B. and Lun, C. K. K. (1988). Particle size segregation in inclined chute flow of dry cohesionless granular solids. *Journal of Fluid Mechanics*, 189:311–335.

Schmeeckle, M. W., Nelson, J. M., and Shreve, R. L. (2007). Forces on stationary particles in near-bed turbulent flows. *Journal of Geophysical Research: Earth Surface*, 112(F2).

Schwager, T. and Poschel, T. (2007). Coefficient of restitution and linear–dashpot model revisited. *Granular Matter*, 9(6):465–469.

Shi, Q., Sun, G., Hou, M., and Lu, K. (2007). Density-driven segregation in vertically vibrated binary granular mixtures. *Physical Review. E, Statistical, Nonlinear, and Soft Matter Physics*, 75:061302.

Shields, A. (1936). Anwendung der Aehnlichkeitsmechanik und der Turbulenzforschung auf die Geschiebebewegung. *PhD Thesis Technical University Berlin*.

Smilauer et al., V. (2015). *Yade Documentation 2nd Ed. The Yade Project.* Zenodo.

Srebro, Y. and Levine, D. (2003). Role of friction in compaction and segregation of granular materials. *Physical Review. E, Statistical, Nonlinear, and Soft Matter Physics*, 68:061301.

Staron, L. (2018). Rising dynamics and lift effect in dense segregating granular flows. *Physics of Fluids*, 30(12):123303.

Staron, L. and Lajeunesse, E. (2009). Understanding how volume affects the mobility of dry debris flows. *Geophysical Research Letters*, 36:L12402.

Stokes, G. G. (1851). On the effect of internal friction of fluids on the motion of pendulums. *Transactions of the Cambridge Philosophical Society.*, 9(part ii):8–106.

Thomas, N. (2000). Reverse and intermediate segregation of large beads in dry granular media. *Physical Review. E, Statistical Physics, Plasmas, Fluids, and Related Interdisciplinary Topics*, 62:961–974.

Thornton, A., Weinhart, T., Luding, S., and Bokhove, O. (2012). Modeling of particle size segregation: Calibration using discrete particle method. *International Journal of Modern Physics C*, 23(08):1240014.

Thornton, A. R., Gray, J. M. N. T., and Hogg, A. J. (2006). A three-phase mixture theory for particle size segregation in shallow granular free-surface flows. *Journal of Fluid Mechanics*, 550:1–25.

Tripathi, A. and Khakhar, D. V. (2011a). Numerical Simulation of the Sedimentation of a Sphere in a Sheared Granular Fluid: A Granular Stokes Experiment. *Physical Review Letters*, 107(10):108001.

Tripathi, A. and Khakhar, D. V. (2011b). Rheology of binary granular mixtures in the dense flow regime. *Physics of Fluids*, 23(11):113302.

Tripathi, A. and Khakhar, D. V. (2013). Density difference-driven segregation in a dense granular flow. *Journal of Fluid Mechanics*, 717:643–669.

Turowski, J. M., Rickenmann, D., and Dadson, S. J. (2010). The partitioning of the total sediment load of a river into suspended load and bedload: A review of empirical data. *Sedimentology*, 57(4):1126–1146.

Ulrich, S., Schröter, M., and Swinney, H. L. (2007). Influence of friction on granular segregation. *Physical Review. E, Statistical, Nonlinear, and Soft Matter Physics*, 76:042301.

Utter, B. and Behringer, R. P. (2004). Self-diffusion in dense granular shear flows. *Physical Review E*, 69(3):031308.

Van der Vaart, K., Gajjar, P., Epely-Chauvin, G., Andreini, N., Gray, J., and Ancey, C. (2015). Underlying Asymmetry within Particle Size Segregation. *Physical review letters*, 114:238001.

Van der Vaart, K., Van Schrojenstein Lantman, M. P., Weinhart, T., Luding, S., Ancey, C., and Thornton, A. R. (2018). Segregation of large particles in dense granular flows suggests a granular Saffman effect. *Physical Review Fluids*, 3:074303.

Weinhart, T., Hartkamp, R., Thornton, A. R., and Luding, S. (2013). Coarse-grained local and objective continuum description of three-dimensional granular flows down an inclined surface. *Physics of Fluids*, 25(7):070605.

Whitaker, A. C. and Potts, D. F. (2007). Coarse bed load transport in an alluvial gravel bed stream, Dupuyer Creek, Montana. *Earth Surface Processes and Landforms*, 32(13):1984–2004.

Wiberg, P. L. and Smith, J. D. (1985). A theoretical model for saltating grains in water. *Journal of Geophysical Research: Oceans*, 90(C4):7341–7354.

Wiederseiner, S., Andreini, N., Epely-Chauvin, G., Moser, G., Monnereau, M. L., Gray, J. M., and Ancey, C. (2011). Experimental investigation into segregating granular flows down chutes. *Physics of Fluids*, 23:013301.

Wilcock, P. R. (1993). Critical Shear Stress of Natural Sediments. *Journal of Hydraulic Engineering*, 119(4):491–505.

Wilcock, P. R. and Crowe, J. C. (2003). Surface-based Transport Model for Mixed-Size Sediment. *Journal of Hydraulic Engineering*, 129(2):120–128.

Abstract Understanding particle size segregation is one of the great challenge in fluvial geomorphology. It is still notoriously difficult to predict sediment transport more accurately than within one order of magnitude. One of the main origin of this difficulty is particle size segregation, a granular process of particle sorting in the sediment bed. Size segregation is therefore a grain scale process impacting the morphological scale.

This PhD presents a numerical study of size segregation as a granular process during bedload transport. A coupled fluid discrete element method (DEM) is used to study the infiltration of small particles in a large particle bed. This configuration, close to granular flows on erodible bed, is characterized by a particle velocity profile, a shear rate profile and an inertial number profile exponentially decreasing into the bed. It presents a particular segregation phenomenology with small particles infiltrating the bed as a travelling wave, the velocity being controlled by the inertial number at the bottom of the layer. The segregation velocity is observed dependent on the local small particle concentrations and on the size ratio. The segregation problem is also analyzed with an advection diffusion model. With advection and diffusion coefficients both proportional to the inertial number, the continuum model perfectly reproduces the dynamics observed in the DEM results.

Very recently, a new segregation advection diffusion model has been derived based on particle scale forces, in particular a granular buoyancy force (or segregation force) and an inter-particle drag force. This provides new physically based parametrisations for the advection and diffusion coefficients. This new model is analysed in the bedload configuration, and reproduces qualitatively the DEM results. To improve the model, new dependencies on the inertial number and small particle concentration are proposed for the segregation and drag forces.

Finally, the impact of size segregation on sediment transport is studied through the mobility of bidisperse already segregated particle beds. Large particles are placed above small ones, and it is observed that, in the same fluid and surface bed conditions, the transport rate is higher in the bidisperse configuration than in the monodisperse one. For the range of studied size ratio ($r < 4$), it is showed that it is not a rugosity but a granular effect. This is analyzed within the framework of the $\mu(I)$ rheology and it is demonstrated that the buried small particles are more mobile than larger particles and play the role of a conveyor belt for the large particles at the surface. Based on rheological arguments, a simple predictive model for the additional transport in the bidisperse case is proposed, which reproduces quite well the DEM results for a large range of Shields number and for size ratios smaller than 4. The results of the model were used to identify four different transport regimes of bidisperse mixtures, depending on the mechanisms responsible for the mobility of the small particles.

This work represents an important improvement in the understanding of size segregation during bedload transport and questions our understanding of bidisperse granular media, which have not been much studied. It also represents a first step in an upscaling process towards the morphological scale through continuum models.